IMPLEMENTATION OF A PHOTOELECTRONIC MOTION TRANSDUCER FOR MEASURING SUB-MICROMETER DISPLACEMENTS OF VESTIBULAR BUNDLES

Andrew Charles Merkle

Thesis submitted to the Faculty of the
Virginia Polytechnic Institute and State University
in partial fulfillment of the requirements for the degree of

MASTER OF SCIENCE

in

Engineering Mechanics

J.Wallace Grant, Chair
Thomas E. Diller
Ellengene H. Peterson
Laura A. Wojcik

May 23, 2000
Blacksburg, Virginia

Keywords: Utricle, Vestibular System, Hair Cell, Photodiode

IMPLEMENTATION OF A PHOTOELECTRONIC MOTION TRANSDUCER FOR MEASURING SUB-MICROMETER DISPLACEMENTS OF VESTIBULAR BUNDLES

by

Andrew Charles Merkle

Committee Chairman: J. W. Grant

Engineering Mechanics

(ABSTRACT)

The vestibular system is one of our main organs responsible for the sense of balance. This system is located within the inner ear and contains cells with ciliary bundles. These hair cells are transducers that convert a mechanical movement, detected by the bundle of cilia extending from their top surface, into an electrochemical signal to be sent to the brain. The bundles vary structurally within the organs of the inner ear, and this structural difference may play a role in the mechanical properties of each bundle. Analyzing the mechanical properties of the cells will provide information necessary for understanding the transduction process. In an effort to evaluate one of these properties, cell bundle stiffness, a system was designed to mechanically stimulate the bundles within their physiological range and then measure the resulting displacement. The mechanical stimulation was the result of a force applied to the tip of a bundle with the end of a glass whisker. The distance the base of the whisker moves is measured by an extrinsic Fabry-Perot interferometer (EFPI). The magnitude of this movement is compared with the amount the bundle is deflected, detected by a photoelectronic motion transducer (PMT). Knowing these displacements and the stiffness of the glass whisker, simple kinematics is used to determine the bundle stiffness. System tests were conducted on imitation bundles (whiskers of known stiffness) and the experimental stiffness differed from the known value by less than 4.5% for every test. These results lead us to conclude the system was in good working order and could be used to conduct tests on cell bundles. For tissue tests, this work focused on the hair cells located within the utricle, which senses linear accelerations of the head. Within the utricle, we examined two types of hair cells: non-striolar (medial type II) and striolar. Tests on twelve medial type II cells found bundles ranging in stiffness from 0.26 to 2.62×10^{-5} N/m. Results with striolar bundles provided a range from 2.83 to 27.10×10^{-5} N/m. The results of the preliminary tissue tests lead us to conclude that the average stiffness of the striolar and non-striolar bundles seems to vary by an order of magnitude. This is consistent with the relative relationship produced through a computer model. However, the model predicted larger stiffness values for both types of cells.

ACKNOWLEDGMENTS

First and foremost, I would like to thank my advisor and committee chair, Dr. J. W. Grant. Not only did he supply the finances and facilities to support this project, but he also provided the guidance and instruction necessary for its completion. His encouraging and supportive nature was the driving force behind this work.

I would also like to thank Dr. E. H. Peterson, Dr. L. A. Wojcik and Dr. T. Diller for taking positions on my graduate committee. Dr. Peterson was the source for information on bilological aspects as well as the provider of techniques and equipment used in tissue preparation. Unfortunately, I did not take nearly as much advantage of the knowledge and areas of expertise of Dr. Wojcik and Dr. Diller that I could have. Let this be a lesson to make use of all of your resources (especially ones that save you time).

Those who I would like to thank for their technical support include the craftsmen at the ESM Machine Shop, the engineers at Luna Innovations, the representatives of Burleigh, Nik Teichmann of Zeiss, and Keith Duncan. At one time or another, these groups or individuals were a great help in furthering my progress. As for my labmates, John Cotton introduced me to 107 Norris and answered my daily questions regarding the vestibular system. A special thanks to Jen Silverman. She went from destroying tissue samples daily to consistently producing excellent specimens for testing and did not complain when I requested her presence for early morning tests.

Finally, I would like to thank friends and family. Kevin, Gerard, and Andrew were with me since the start of our ESM careers. Zack, Keith, and Matt have been there to provide social relief to school related stresses. Most importantly, I would like to thank my family. My parents, Ted, Shannon, Paul, Adam, and long-time girlfriend Michelle have shown extensive love and support. They have always been there for me and I will never be able to thank them enough. I look forward to finally returning home.

TABLE OF CONTENTS

LIST OF FIGURES

LIST OF TABLES

1.0 INTRODUCTION

The inner ear is very well recognized for the role it plays in audition – the sense of hearing. However, less widely realized is the fact that the inner ear is one of the main organs responsible for the sense of balance. The vestibular apparatus, located within the inner ear, as well as the eyes and the proprioception in the limb muscles are the organs that enable the maintenance of balance. The vestibular system provides information about the movement and position of the head in space and will be the main focus of this thesis.

The following sections will review the anatomy and physiology of the human vestibular system, unless otherwise specified. It will introduce background necessary to comfortably understand this work and provide insight into the mechanisms by which equilibrium is maintained. Furthermore, an outline of this work will be discussed as will motivations and objectives of this project.

1.1 THE INNER EAR

The inner ear is located in the temporal bone of the human skull and begins at the oval window [Gelfand, 1998] as seen in Figure 1.1 It is comprised of three regions: the vestibular apparatus, the cochlea, and the endolymphatic system (Figure 1.2). Each region is responsible for a specific function. The vestibular apparatus senses head motion and maintains balance. The cochlea is essential for hearing since it provides the final mechanical stage for transduction of sound waves into neural signals [Geisler, 1998]. The endolymphatic system bathes the organs with fluids (perilymph and endolymph) that have four essential functions. The fluids serve to deliver nutrients and remove waste, provide a fluid medium for carrying vibratory stimulation, distribute pressure, and provide a chemical environment for energy transformation of vibratory stimuli into neural signals [Gelfand, 1998].

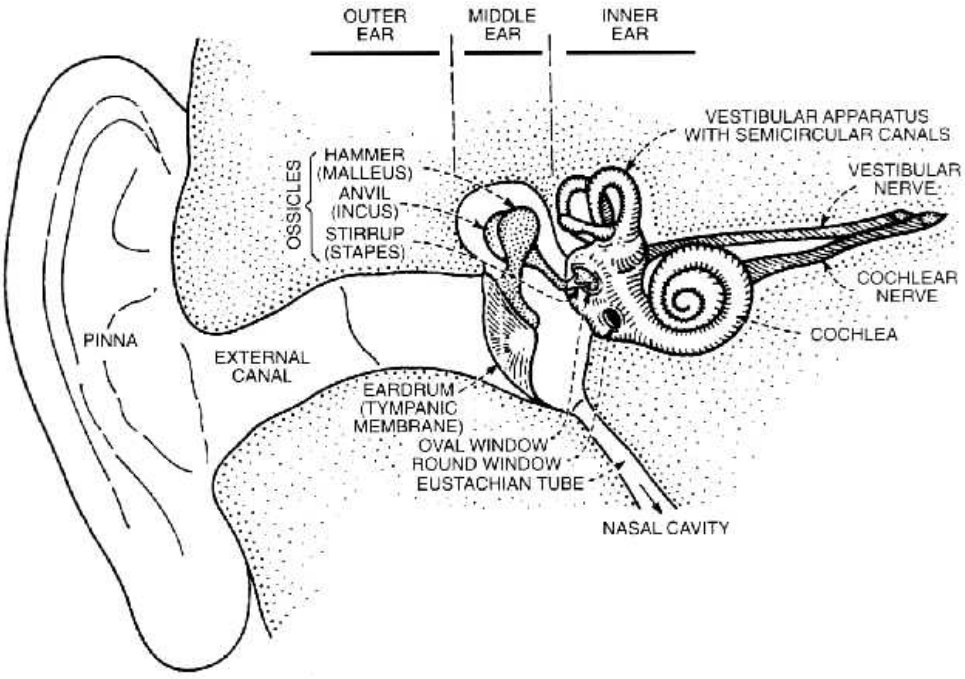

Figure 1.1 Anatomy of the human ear (Geisler, 1998).
The ear is separated into three parts: outer ear, middle ear, and inner ear. The inner ear begins at the oval window.

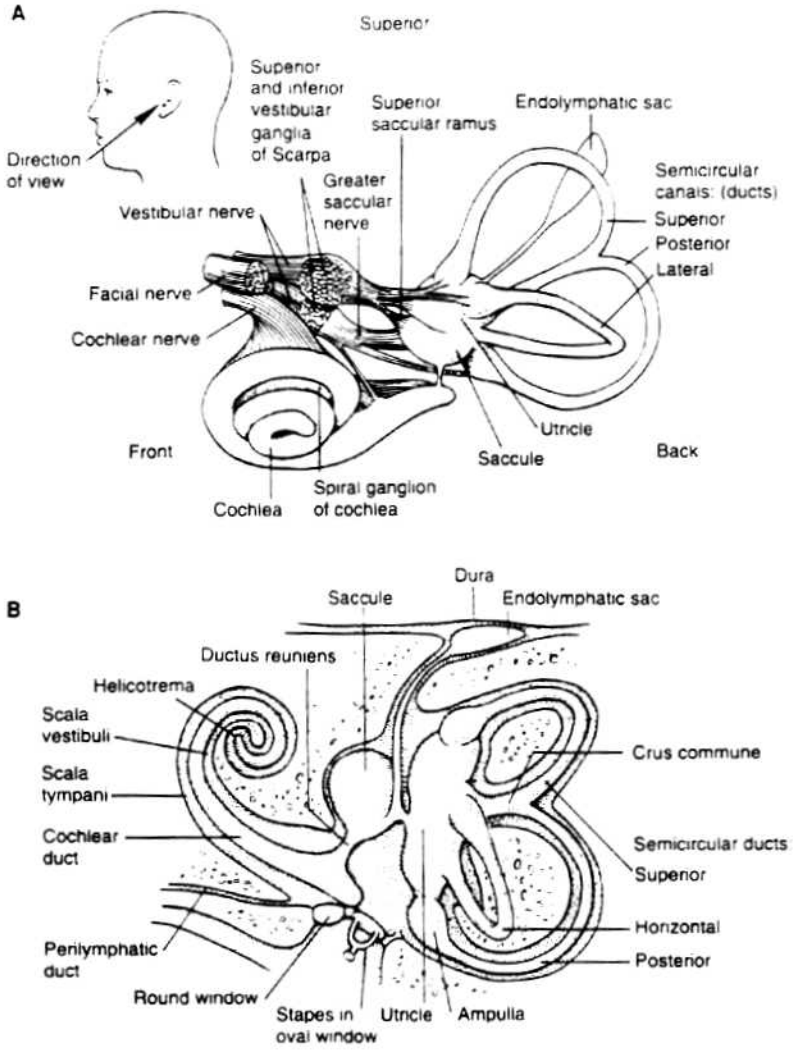

Figure 1.2 Anatomy of the inner ear (Kelly, 1991).
A. The inner ear has three sections: the vestibular apparatus, the cochlea and the endolymphatic sac. **B.** The drawing shows that the inner ear is divided into a bony and membranous labyrinth. It also depicts the different regions of the vestibular apparatus.

The inner ear structures are contained within a system of spaces and canals called the bony labyrinth (Figure1.3). Within these spaces lies the membranous labyrinth which is made up of a simple epithelium. In specialized regions, the simple epithelium of the membranous labyrinth is elaborated into a sensory epithelium that serves as a transducing structure for either audition or balance [Kelly, 1981].

1.1.1 Hearing

The human ear is an energy transformation system that has been separated into three parts as previously shown in Figure 1.1: outer ear, inner ear, and middle ear. The transformation begins when sound waves reach the outer ear as acoustic energy. The waves are gathered and propagate to the middle ear where they are transformed at the eardrum into mechanical energy. These waves are amplified by the auditory ossicles to overcome the impedance mismatch caused between the air-filled middle ear and the fluid-filled inner ear. The mechanical energy is then transformed into hydraulic energy in the form of hydraulic waves. These waves continue on in the inner ear and stimulate neural sensory equipment that creates bioelectric energy. At this point, the auditory signal is ready for transmission to and processing in the brain [Perkins and Kent, 1986].

The outer ear consists of two parts: the auricle, or pinna, and the canal. The auricle is the external appendage of the ear that gathers sound. The ear canal is a tube that conveys the gathered sound waves to the eardrum. The canal is lined with cilia for filtering dust and secretes cerumen (earwax) to prevent the canal from drying out [Perkins and Kent 1986].

The vibrations from the eardrum enter the air filled cavity known as the middle ear. This cavity contains the tympanic membrane and the three smallest bones in the body called the auditory ossicles [Geisler, 1998]. The three bones, seen in Figure 1.5, are the malleus (hammer), incus (anvil), and the stapes (stirrup). Together, the ossicles increase pressure and transmit eardrum vibrations to the fluid in the middle ear. The footplate of the stapes fits into the oval window of the inner ear. The footplate swings back and forth, due to vibrations, thereby converting the mechanical eardrum vibrations into hydraulic waves [Perkins and Kent, 1986].

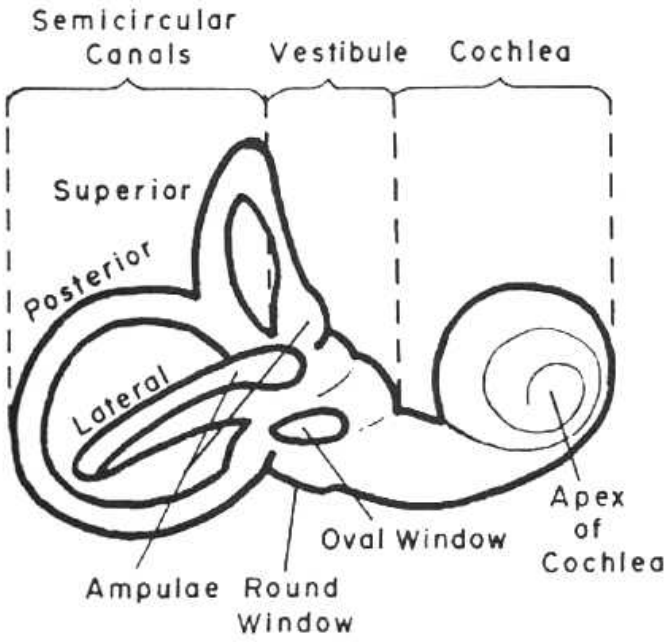

Figure 1.3 The bony labyrinth (Gelfand, 1998).
The bony labyrinth is a system of spaces and canals that house the membranous labyrinth.

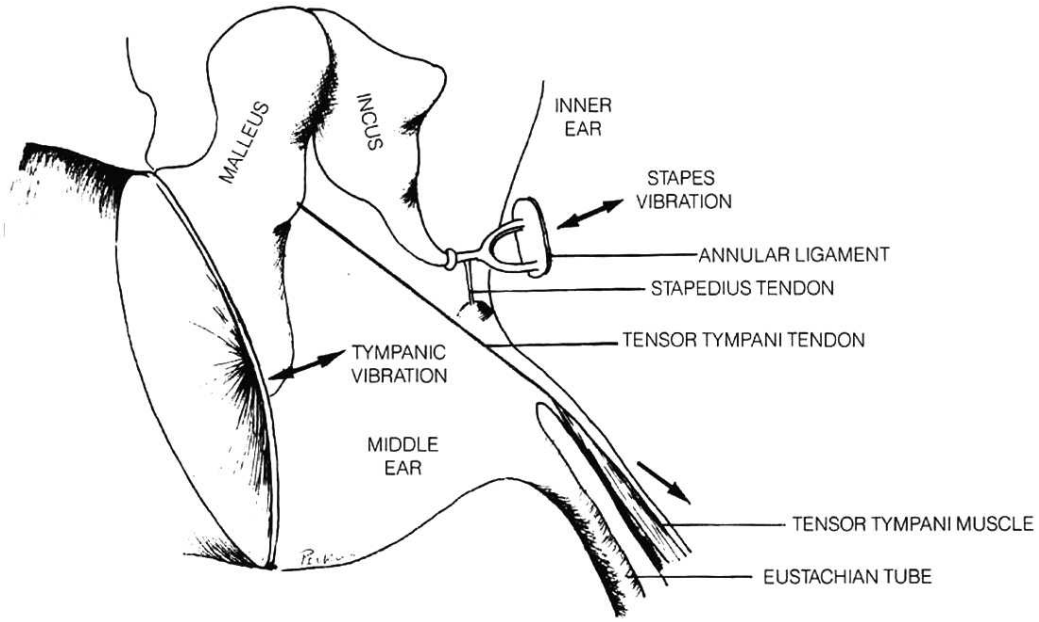

Figure 1.4 The auditory ossicles of the middle ear (Perkins and Kent, 1986).
The mechanical vibrations from the eardrum result in a vibration of the footplate of the stapes. The swinging of the footplate creates hydraulic waves in the fluid-filled inner ear.

The stapes proceeds to vibrate the oval window which causes a wave motion in the endolymphatic fluid of the cochlea in the inner ear. The wave begins in the scala vestibuli and is transferred to the scala media (Figure 1.5), causing the basilar membrane to vibrate up and down. This vibration travels into the Organ of Corti and leads to a displacement of the basilar and tectorial membranes relative to one another.

The displacement causes the cilia of the hair cells (described in section 1.2), which are in contact with the tectorial membrane, to undergo a shearing force and become bent. This process is depicted in Figure 1.6 and is the last mechanical step involved in hearing. The movement of the cilia generates a neural auditory signal that is sent to the brain via the eighth cranial nerve [Klinke, 1986].

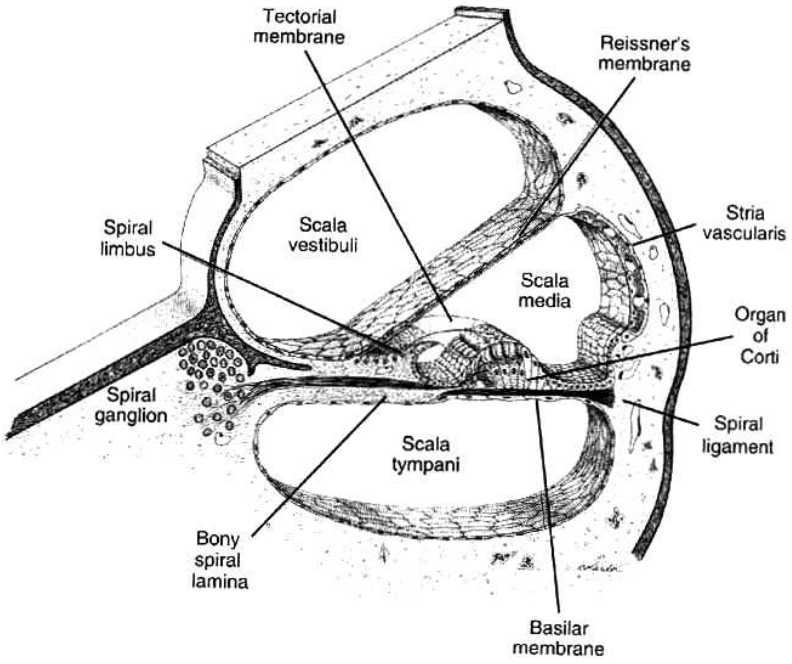

Figure 1.5 Segment of the cochlear duct (Geisler, 1998).
The hydraulic waves begin in the scala vestibuli and cause the basilar membrane to vibrate. The vibration leads to a displacement of the basilar and tectorial membranes and a shearing of the cochlear hair cells.

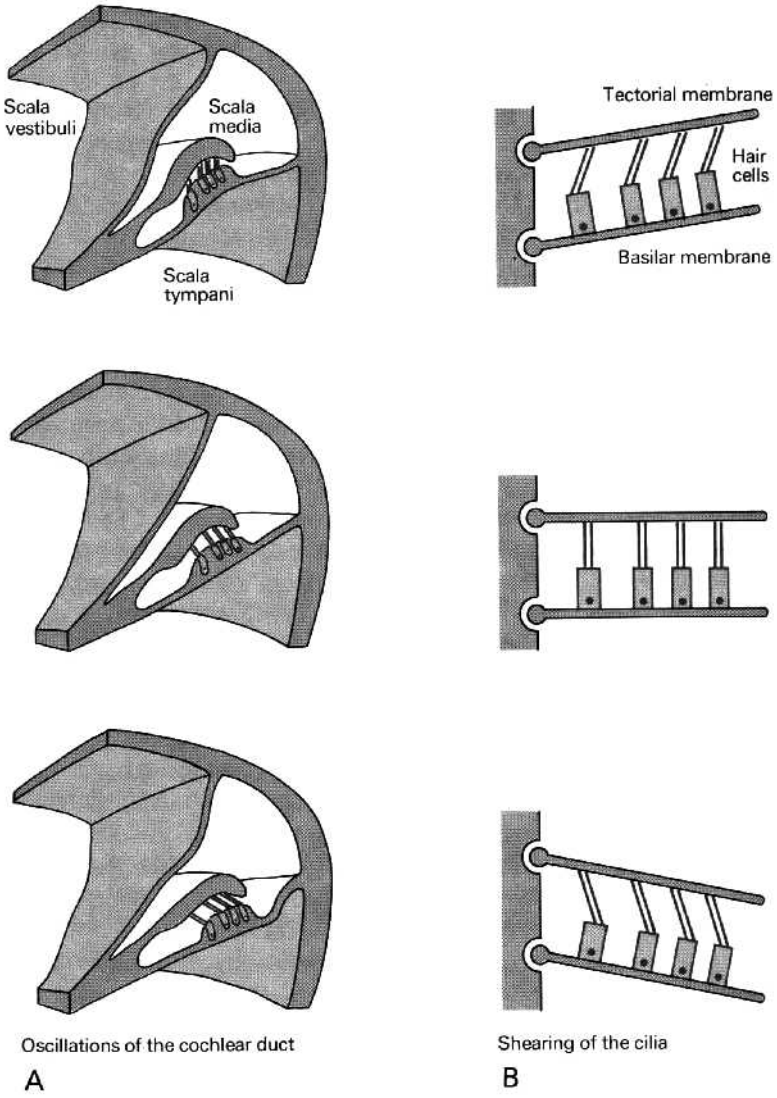

Figure 1.6 Cochlear response to vibrations (Schmidt, 1986).
A. The response of the cochlear duct to vibrations causes displacement of the basilar and tectorial membranes with respect to one another. **B.** A model displaying how the cilia of the hair cells are sheared as the membranes are displaced.

1.1.2 Equilibrium

As mentioned earlier, the vestibular system is also located in the inner ear and is involved in the sense of balance and maintenance of equilibrium. This system is essential for the coordination of motor responses, eye movement, and posture [Kelly, 1991]. There are two main organs that coordinate this sensory information: the otolith organs and the semicircular canals, which are pictured in Figure 1.7. Each of these organs contains a sensory epithelium with a very similar structure. However, they differ in the form and arrangement of the cells and in the superstructure that lies above the cilia that project from the sensory cells [Engström and Engström, 1981].

The otolith organs are divided into two sacs, the utricle and the saccule, which both reside in the vestibular portion of the membranous labyrinth [Kelly, 1981]. These two organs are important in detecting linear acceleration due to head movement and for determining the position of the head with respect to gravity. The receptor cells (hair cells) are grouped in a sensory epithelium, or macula, in each sac [Shepherd, 1988]. The macula consists of hair cells surrounded by supporting cells. These hair cells project into a gelatinous mass in which small crystals of calcium carbonate, called otoconia, are embedded. The otoconia have a high specific gravity and along with the gelatinous mass they form the otolith membrane [Klinke, 1986]. The orientation of this membrane in the macula is shown in Figure 1.8.

When the head is tilted to one side or the other, the force of gravity slightly displaces the otolith membrane. As it moves this short distance with respect to the sensory epithelia, it bends the cilia. This bending creates a shearing stress similar to that experienced by the hair cells of the cochlea. The result is a signal carried by afferent fibers of the VIIth cranial nerve from the inner ear to signal processing centers in the brain [Lewis, *et al*, 1985].

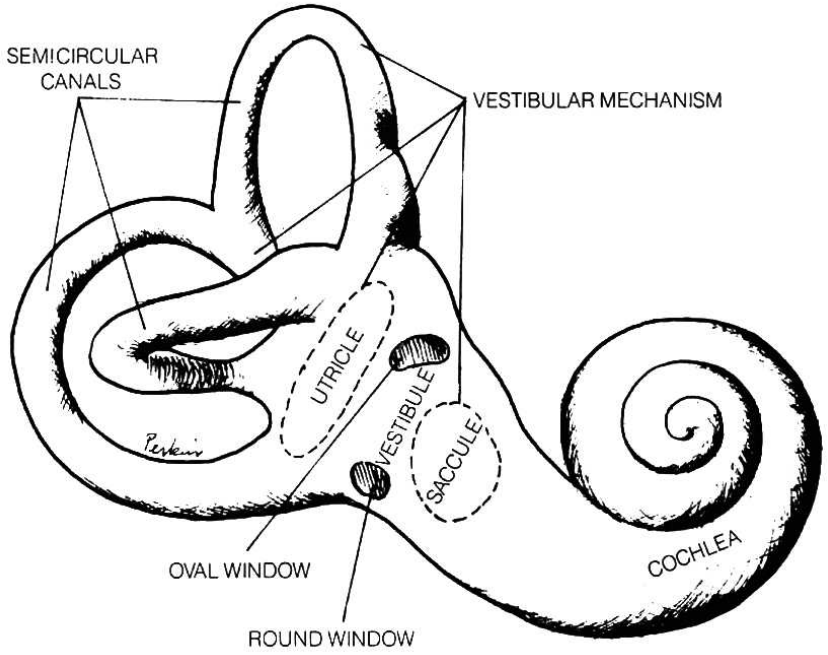

Figure 1.7 Sensory organs of the vestibular system (Perkins and Kent, 1986).
The two main organs that coordinate sensory information in the vestibular system are the semicircular canals, of which there are three, and the otolith organs (utricle and saccule).

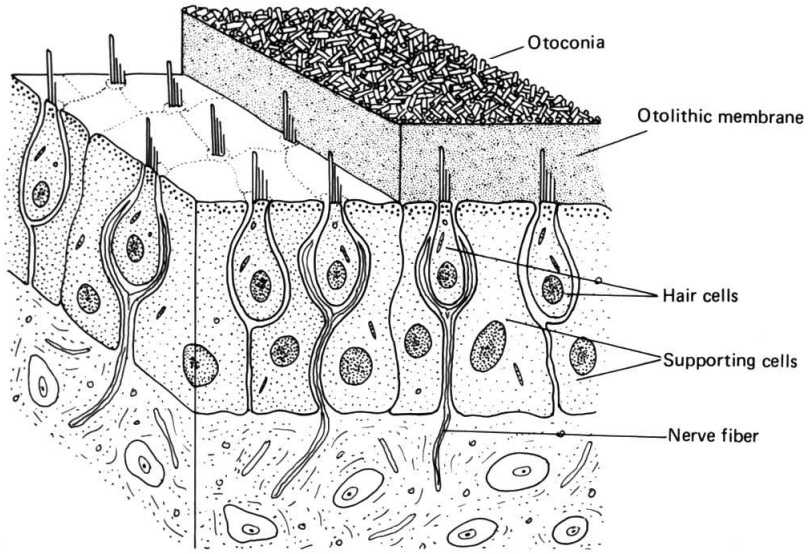

Figure 1.8 Orientation of the otolithic membrane (Kelly, 1981).
The hair bundles are positioned within the gelatinous membrane which has an otoconial layer on top. Together, they form the otolithic membrane.

The second organ that coordinates sensory information is composed of three semicircular canals. The canals are located above and behind the vestibule, which is the middle dilated portion of the bony labyrinth as seen in Figure 1.9 [Singh, 1980]. The anterior and posterior semicircular canals are located in the vertical plane at right angles to each other while the lateral canal sits in a plane that forms a 30° angle with horizontal when the head is in its normal position [Klinke, 1986]. The orientation of the three canals within the skull is shown in Figure 1.10. As a consequence of their orthogonal arrangement in 3-dimensional space, the semicircular canals are very good detectors of angular acceleration in numerous directions [Kelly, 1981].

Within each semicircular canal there is a semicircular fluid filled duct about one-fourth the diameter of the canal. Each duct contains an enlarged end with a structure termed the ampulla shown in Figure 1.11 [Singh, 1980]. In the ampulla (Figure 1.12), a gelatinous membrane, the cupula, projects into the fluid and has a specific gravity exactly equal to the surrounding endolymph. Contrary to the otolith membrane in the otolith organs, having a specific gravity equal to that of its surroundings allows the cupula to move along with the canal during linear accelerations. However, rotational acceleration does affect the cupula due to the inertia of the endolymph. When the skull, initially at rest, is turned, the endolymph at first tends not to move; since the cupula is attached to the wall of the canal, it is pulled in a direction opposite to the rotation [Klinke, 1986] as illustrated by Figure 1. The projections of the receptor cells (cilia) extend into the cupula similar to the way hair cells in the otolith organs extended into the otolith membrane. When the cupula is distorted, a shearing force is created on the projections which stimulates the receptor cells. However, in the semicircular canals the sensory epithelium that contains the receptor cells is referred to as the crista. The crista within the ampulla is analogous to the macula within the utricle or saccule. As with the maculae, an afferent nerve fiber will carry a neural signal to the brain from the receptor cells.

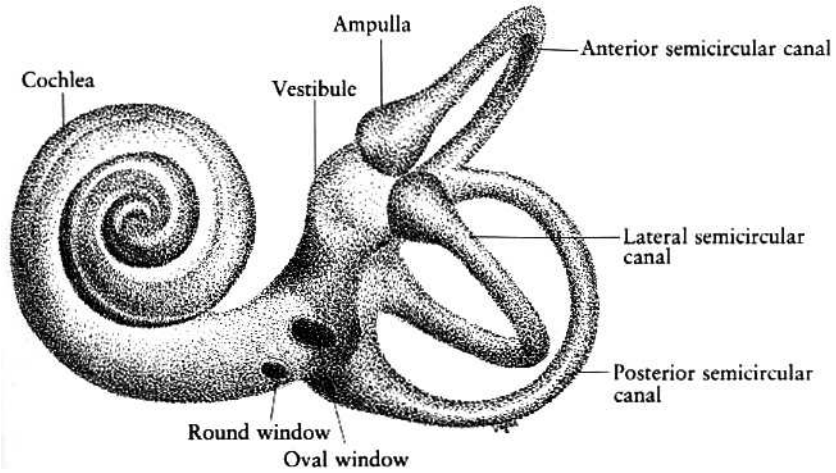

Figure 1.9 The orientation of the semicircular canals within the vestibular system (Singh, 1980).

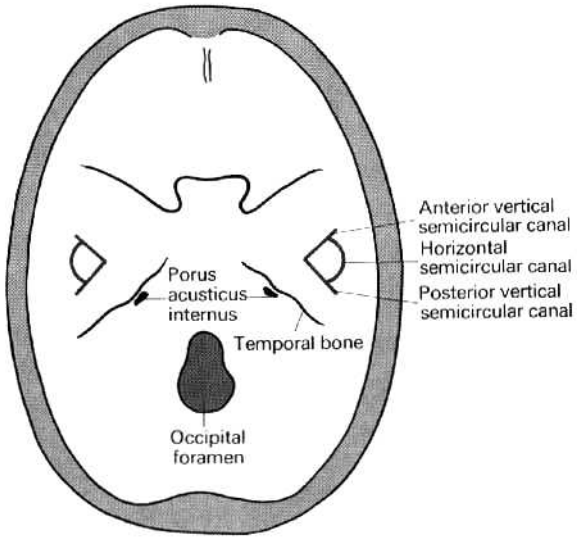

Figure 1.10 Orientation of the semicircular canals in the human skull (Klinke, 1986). This is the view of the three canals as seen by an observer looking down from above at the base of the skull. This view shows the orthogonal arrangement of the canals with respect to one another.

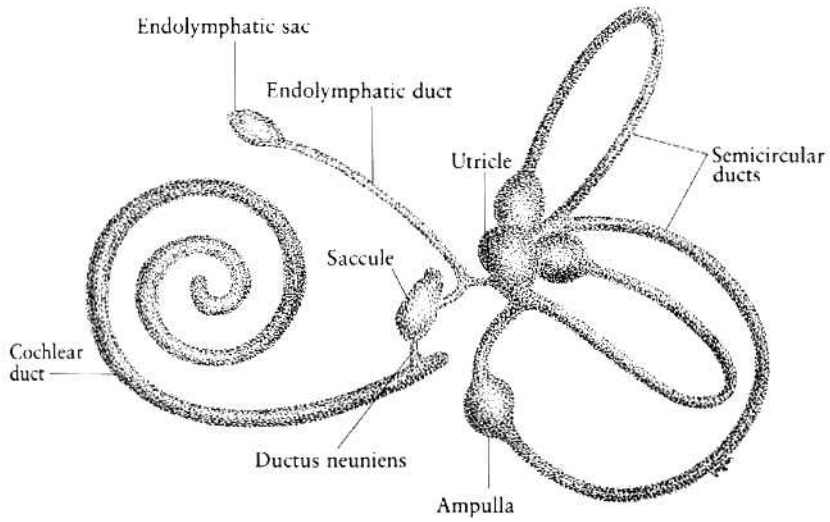

Figure 1.11 The membranous labyrinth (Singh, 1980).
The semicircular ducts are located within the canals. The ducts have an enlarged end known as the ampulla. Within each ampulla are sensory hair cells.

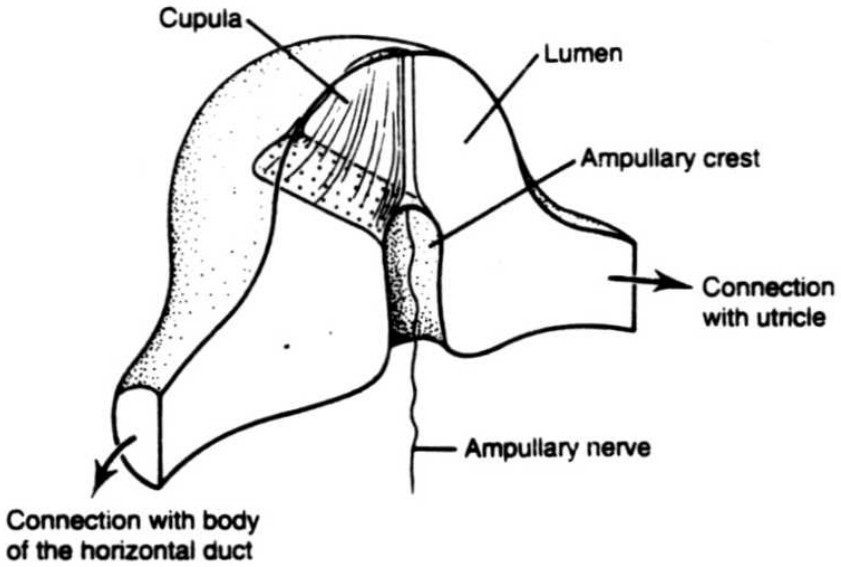

Figure 1.12 The ampulla of the semicircular duct (Kelly, 1981).
The ampullary crest, or the crista, is the sensory epithelium containing the hair cells. The cells are embedded in a gelatinous material called the cupula, which extends to the roof of the ampulla.

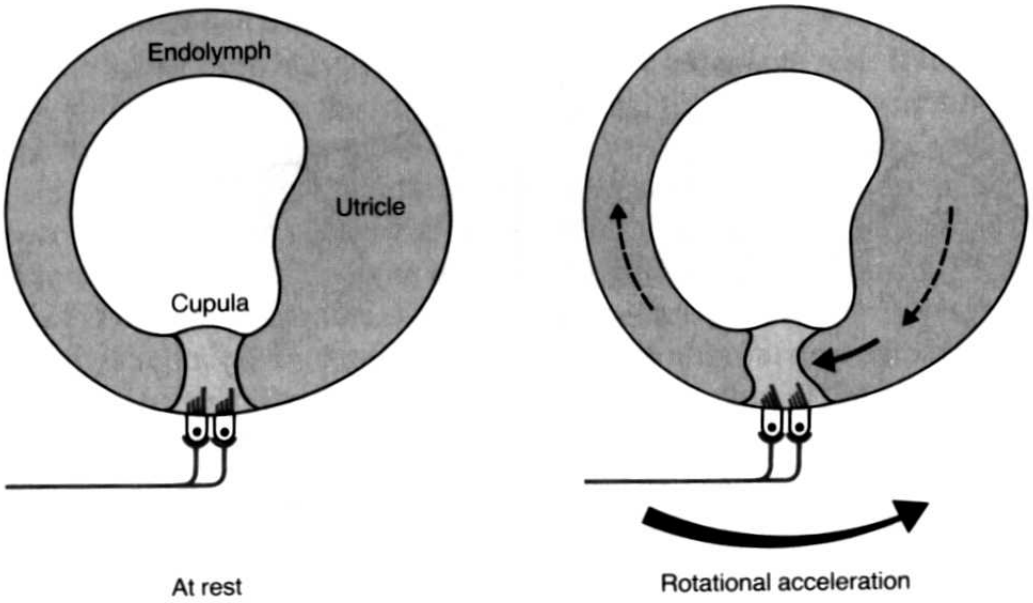

Figure 1.13 Response of semicircular canal to rotational acceleration (Klinke, 1986).
The hair cells are embedded in the cupula and stand upright when not subject to rotational acceleration. During the acceleration, the hair cells experience a shear force due to the pull on the cupula from the endolymph.

1.2 HAIR CELL

The previously mentioned receptor cells located in the sensory epithelium of the otolith organs and the semicircular canals are also referred to as hair cells. These cells vary in size, arrangement, and function depending upon their location within the vestibular system. In the maculae of the utricle and saccule they detect linear acceleration, whereas in the ampullary crests of the semicircular canals the hair cells are responsible for detecting angular accelerations [Kelly, 1981]. These cells are the main topic of this work and their form and function will be examined more closely in this section.

1.2.1 Structure

Each hair cell is characterized by a group of cilia or "hairs" protruding from one end of the cell as shown in Figure 1.14 [Geisler, 1998]. All but one of these cilia extend from a rigid, flat cuticular plate and are called stereocilia. The single remaining cilium, referred to as the kinocilium, resides in a cuticle-free region and protrudes from a basal body [Engström and Engström, 1981]. Each stereocilia is composed of parallel actin filaments tightly packed into hexagonal arrays and oriented along the longitudinal axis of the cilium. The actin strands are cross-linked by transverse striations, most likely fibrin, making the stereocilia into a relatively stiff rod. The diameters of each stereocilia vary, usually from 0.1 to 0.3 μm, and are considerably reduced at the stereocilia's insertion point into the cuticular plate. When subjected to lateral forces, the stereocilia will pivot about their base where they are connected to the cuticular plate. The kinocilia are usually the longest of all of the cilia on the cell and can be as tall as 40 μm on the ampullar cristae. The kinocilium has a cytoplasmic core containing the "9 + 2" arrangement of microtubular doublets characteristic of true cilia as shown in the top view of the hair cells in Figure 1.14 [Geisler, 1998].

The stereocilia are arranged in different configurations on the cuticular plate depending upon the identity of the hair cell. For example, a cell in the saccule of a bullfrog has stereocilia in a tightly packed circle (Figure 1.15) whereas in a mammalian cochlea the stereocilia are arranged in rows (Fig 1.16). Despite the variations, common

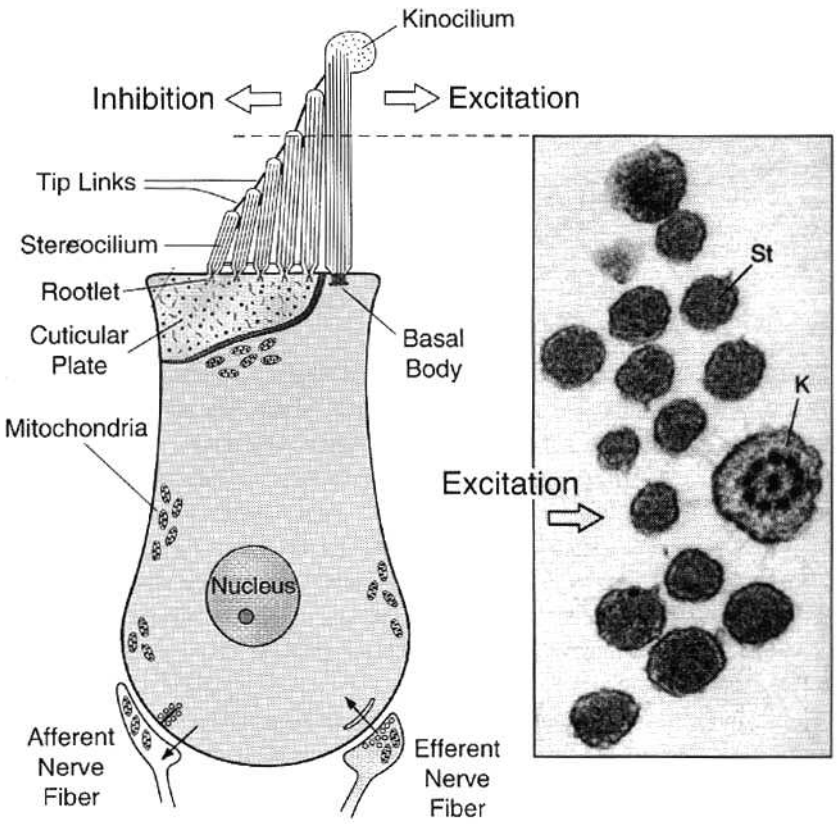

Figure 1.14 Structure of a vertebrate hair cell (Geisler, 1998).
The hair cell has an arrangement of stereocilia projecting from the cuticular plate as well as a longer kinocilium. The kinocilium has a "9+2" organization of microtubule doublets and the stereocilia are packed with actin rods. Depolarization of the cell occurs with deflection towards the kinocilium while hyperpolarization occurs with deflection away from the kinocilium.

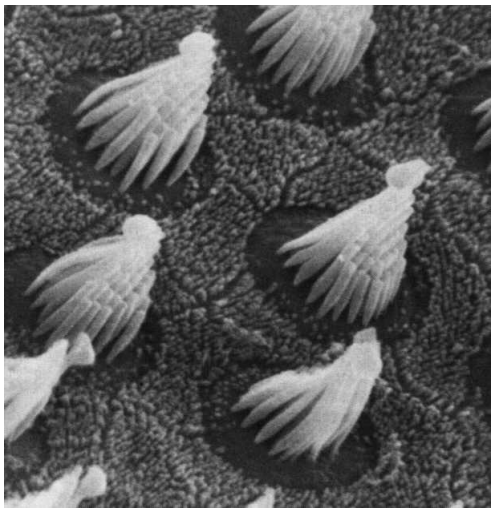

Figure 1.15 Saccular bundle of a bullfrog (Lewis, *et al*, 1985).
The stereocilia of the hair cell bundle are arranged in a tightly packed circle.

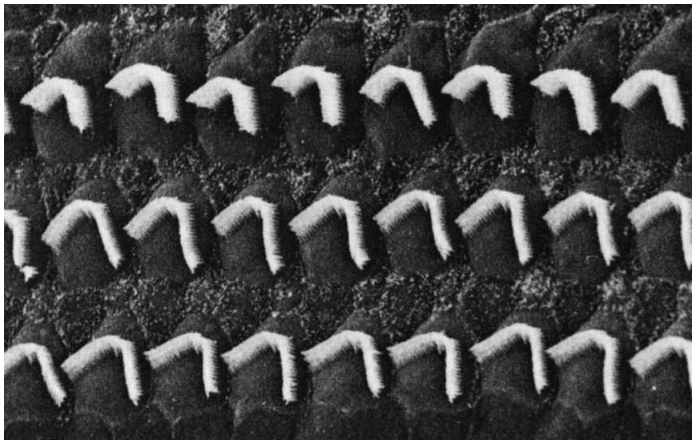

Figure 1.16 Mammalian cochlear bundle (Lewis, *et al*, 1985).
The stereocilia of the hair cell bundle are arranged in rows.

to all of the cells is the fact that the stereocilia stand in a stair-step arrangement. In other words, the stereocilia that stands closest to the kinocilium is tallest with the ones further away from the kinocilium becoming progressively shorter [Geisler, 1998] as seen in Figure 1.17. Each of these stereocilia are connected by tip links and subapical bands discussed in sub-section 1.2.2.

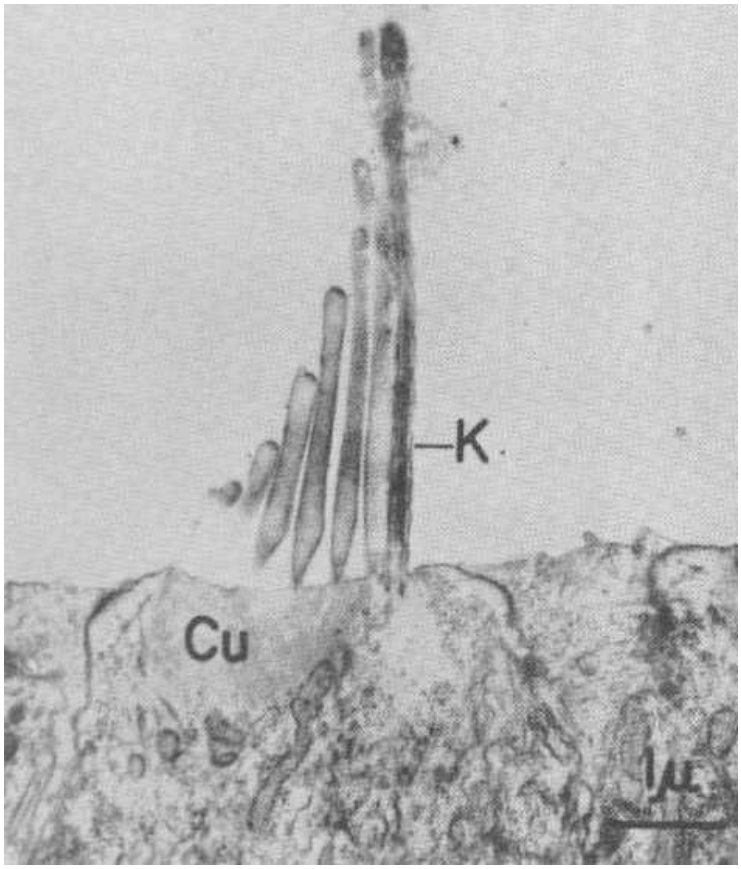

Figure 1.17 Transmission electron micrograph of hair cell apical surface (Kelly, 1981).
The stereocilia increase in length with their proximity to the kinocilium (**K**). The stereocilia project from the cuticle (**Cu**) which occupies the top of the sensory cell except for the area around the basal body of the kinocilium.

1.2.2 Mechanoelectrical Transduction

The kinocilium acts as the functional axis of the hair cell. If the tip movements of the stereocilia occur towards the kinocilium, the result is electrical depolarization. However, when the tips of the stereocilia move opposite the direction of the kinocilium, the cell becomes hyperpolarized. Any movements at right angles to these directions produce little or no response [Geisler, 1998]. However, the response is graded and the closer the angle of movement is to the direction of depolarization, the larger the response [Hudspeth, 1983]. This is depicted in Figure 1.18.

Some hair cells in certain amphibians, reptiles and developing mammals have kinocilia with bulb-like tips which contain dense filamentous material as seen in Figure 1.19. In these cases, the bulbs appear to be attached to adjacent stereocilia and the overlying gelatinous structure. Unbulbed kinocilia are attached to adjacent stereocilia by fine filaments located near the top of the stereocilia [Lewis, *et al*, 1985]. These filaments, possibly elastin, are referred to as tip links and also connect the top of the shorter stereocilium with the lateral wall of its tallest neighbor (Figure 1.14). The cilia are also joined by lateral links, or subapical bands, which occur below the tip links and run in all directions between neighboring stereocilia [Geisler, 1998].

Tip links are believed to play a large role in the transduction of ciliary deflections into cell potentials. One popular theory, named the "Trapdoor" theory, suggests that the tip links are attached to a gate mechanism that controls the flow of ions into the hair cells (Figure 1.20). A hair cell that is not being stimulated has a resting membrane potential. In this case, the tip links are slightly stretched which leaves the gates slightly open and allows a small steady flux of potassium (K^+) and calcium ions (Ca^{2+}) into the cell. These gates are only open a small percentage, some believed to be 10%, and allow the ions, which occur in high concentration in the surrounding endolymph, to enter into the cell.

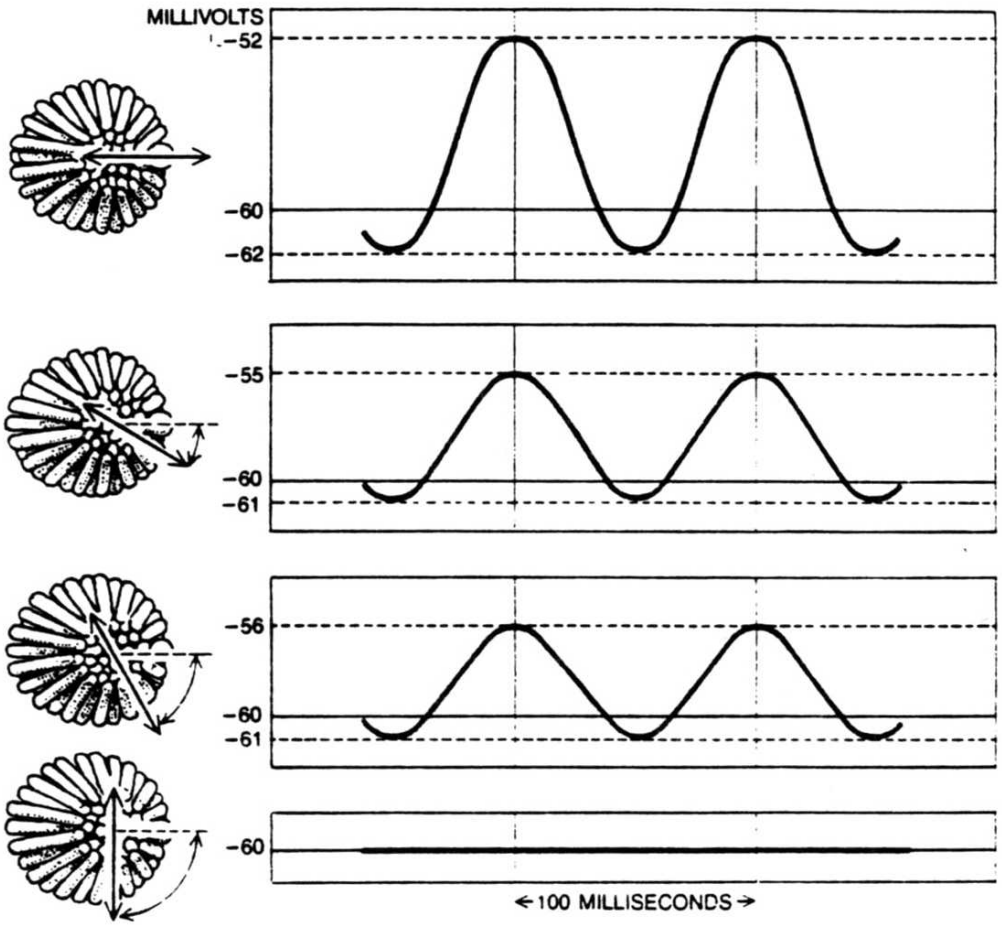

Figure 1.18 Graded receptor cell response (Hudspeth, 1983).
These graphs plot the hair cell's membrane potential versus time and show the total change in the rate at which the vestibular afferent nerve fires. A maximum response occurs when the stereocilia are stimulated in the direction of depolarization (top graph). A graded response will occur for other directions of stimulation. The closer the directional angle to that for depolarization, the greater the response. A minimal response occurs in the direction of hyperpolarization (bottom graph), which is 90° from the direction of depolarization.

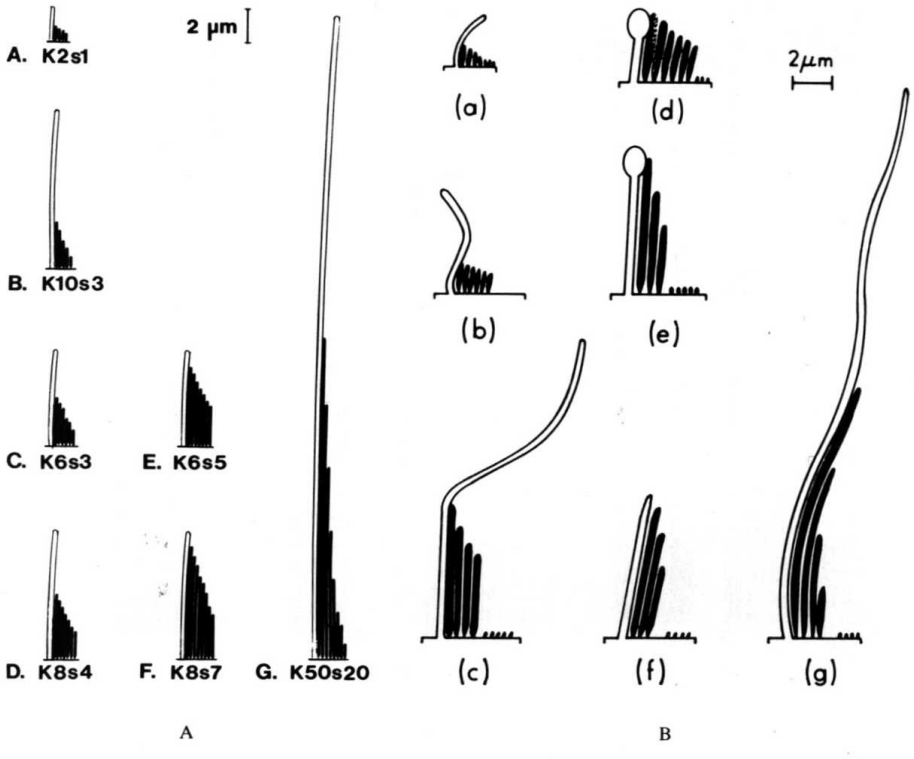

Figure 1.19 Hair cell bundle variation (Lewis, *et al*, 1985).
A. Hair cell bundles from bony fishes. The sizes of the kinocilium and stereocilia vary, as well as their orientation. **B.** Hair cell bundles from bony fishes. As seen in (d) and (e), the kinocilium may be bulbed.

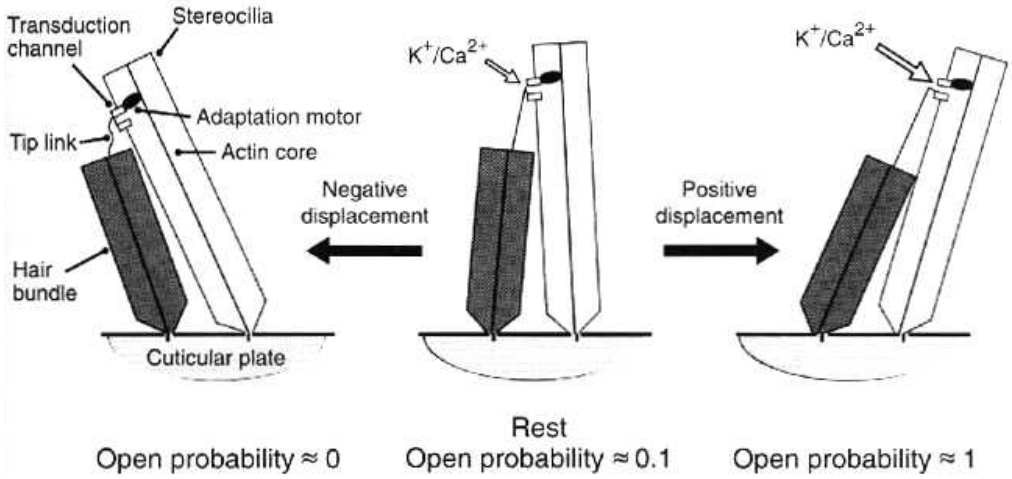

Figure 1.20 "Trapdoor" theory of hair cell excitation (Geisler, 1998).
A change in tension in the tip link is hypothesized to change the cation-conducting probabilities of the transduction channel. Displacements away from the kinocilium relax tip link tension and the trap door is closed. Displacements toward the kinocilium stretch the tip links and increase the probability that the trapdoor is open to an influx of cations.

The influx is driven by the strong electrical potential that exists between the positively charged endolymph and the negatively charged interior of the cell. This results in the resting depolarization of the hair cell [Geisler, 1998].

A positive stimulation occurs when the cilia are forced in the direction of their taller neighbors (usually the kinocilium). This stretches the tip links and causes the ion gates to open. The K^+ and Ca^{2+} ions flow inward at a higher rate and the cell is further depolarized. Negative stimulation occurs when the cilia are stimulated in the direction towards their shorter neighbors. The tension in the tip link will be reduced below its resting value and the influx of ions will be close to none. This will cause the cell potential to decrease below its resting value [Geisler, 1998].

1.2.3 Classification

Hair cells in the epithelium have been classified into two types: type I and type II. The type I cell is flask shaped with a rounded lower end. At the surface there is a cuticle provided with one kinocilium and numerous stereocilia. Below the cuticle the cell has a narrow neck which leads into a wider body around the nucleus as seen in Figure 1.21. The bottom of the cell is surrounded by a nerve chalice which continues as an afferent nerve fiber through the basement membrane and becomes a myelinated nerve fiber [Engström and Engström, 1981].

The second type of cell, type II, is more cylindrical, but also has a rounded lower end as seen in Figure 1.21. At the surface lies a cuticular plate with one kinocilium and numerous stereocilia. Contrary to type I cells, the type II cell has contact with many nerve endings which form synapses along the cell at locations both below and above the level of the nucleus [Engström and Engström, 1981]. Supporting cells, often with their nuclei close to the basement membrane, separate individual sensory cells within the sensory epithelium.

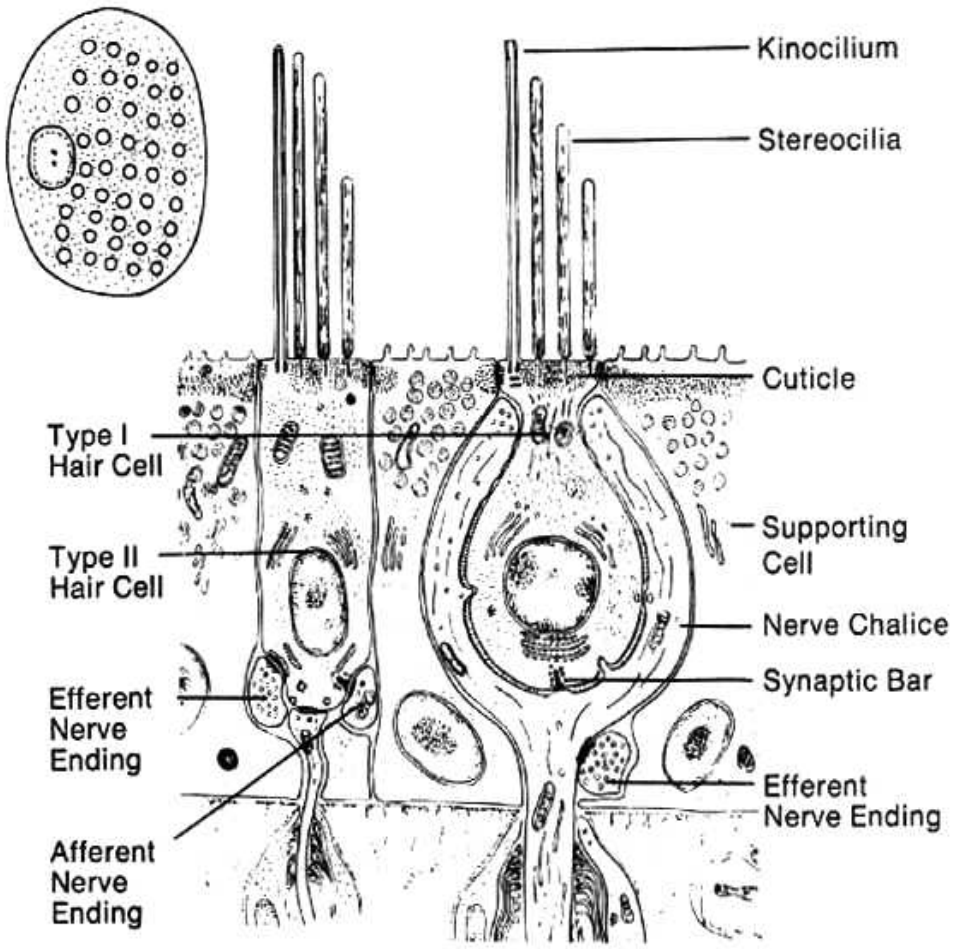

Figure 1.21 Hair cell types of the vestibular labyrinth (Shepherd, 1988).
The type I hair cell is innervated by a nerve chalice and is rounded at the bottom. The type II cell is innervated by multiple nerve endings and has a cylindrical shape.

1.2.4 Ampulla Response to Angular Acceleration

As previously mentioned, the size, arrangement, and function of hair cells depends on where they are located in the vestibular system. The hair cells located within the semicircular ducts are used to sense rotational accelerations. The nervous system requires the semicircular canals to be capable of sensing rotations on three possible independent axes. These axes correspond to head movement and occur when the head is 1) turned about its vertical axis, 2) inclined forward or backward, and 3) tilted to either side [Klinke, 1986]. The semicircular ducts are located on either side of the head (Figure 1.22) and the hair cell arrangements in the ducts allow them to work in pairs [Kelly, 1981]. All of the hair cells in one crista are oriented in the same direction relative to the plane of the semicircular canal. Vertical (both anterior and posterior) canal cells are oriented toward the canal and away from the utricle. Horizontal canal hair cells are oriented toward the utricle [Lewis, *et al*, 1985].

To illustrate their cooperative function, imagine when the head turns to the left. Looking at Figure 1.23 we see that the fluid in the horizontal ducts will lag behind the turning motion due to inertia. As a result, the fluid in the left duct will force the hair bundles in the direction of their axes of polarization while the fluid in the right duct forces the hair bundles in the direction of hyperpolarization. Therefore, the hair cells located in the left ampulla will depolarize and excite afferent fibers innervating them. Conversely, the hair cells of the right ampulla are hyperpolarized and will decrease the firing rate of afferent fibers innervating them. The brain will receive two signals. The signal from the left shows an increase in firing of eighth cranial nerve fibers while that of the right shows a decrease [Kelly, 1981].

The anterior and posterior ducts work in a similar fashion. However, since the anterior ducts on the left and right are not in the same plane, they do not work as a pair. Rather, the anterior duct of the left ear works with the posterior duct of the right ear because they lie in approximately the same plane (refer to Figure 1.22). The same applies to the right anterior and left posterior ducts as they work as a pair to provide bilateral indication of head movement [Kelly, 1981].

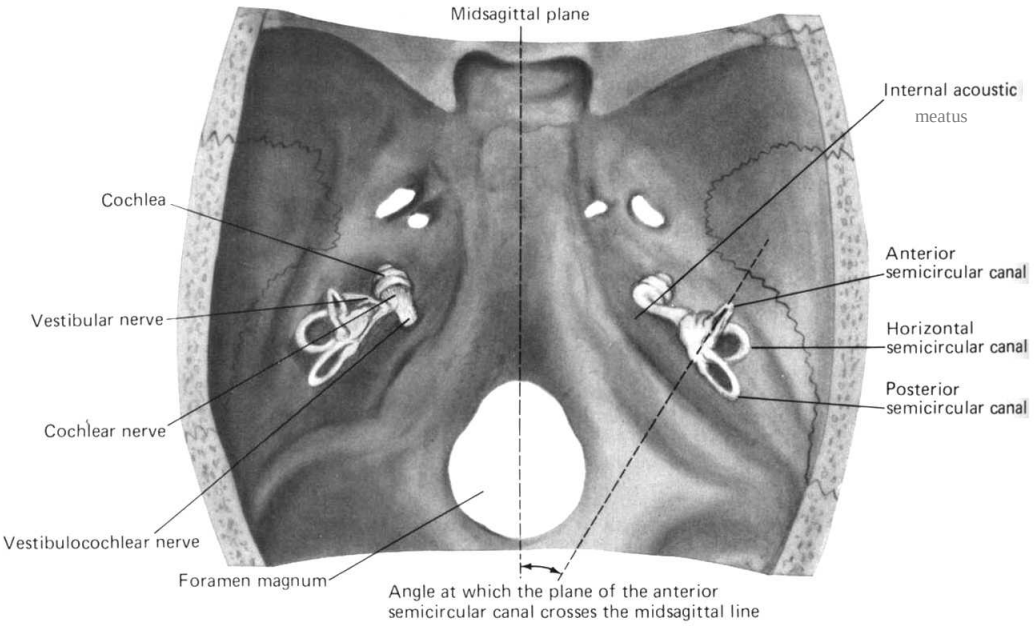

Figure 1.22 Semicircular canal orientation within the skull (Kelly, 1981).
The semicircular canals are located on each side of the head. They are mutually orthogonal and those that lie in the same plane work in pairs.

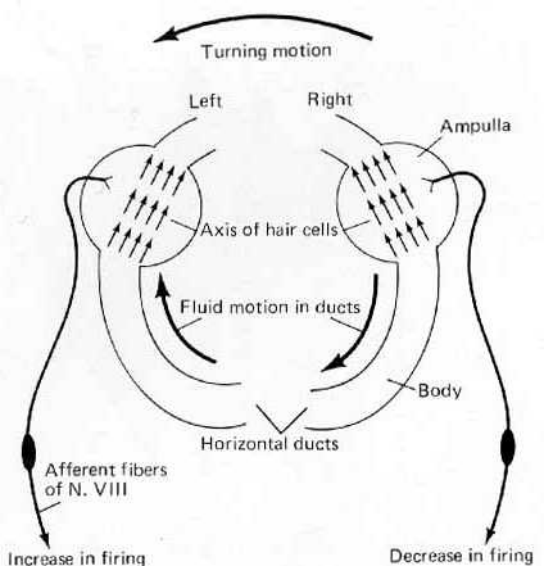

Figure 1.23 Horizontal ducts working as a pair (Kelly, 1981).
The view of the horizontal ducts from above demonstrates how paired canals work in unison to provide bilateral indication of head movement.

Typically, type I cells are predominant in the sensory epithelium of mammalian canals. They are broadly distributed over the crista and outnumber type II cells. The type II cells can be found in the crest or in a narrow marginal zone of exclusively type II cells. In turtles, type I hair cells are concentrated in two large patches on each vertical canal crista or one patch on horizontal canal crista. The location and orientation of type I cells for reptiles and mammals are compared in Figure 1.24. Type II cells surround these patches and spread broadly across ampullary walls [Lewis, *et al*, 1985].

1.2.5 Saccule and Untricle Response to Linear Acceleration and Static Displacement

In the saccule, the macula is divided into two populations of oppositely oriented hair cells. The dividing line approximately follows the longitudinal axis of the macula, which curves considerably in some animals. Hair cells on either side of the line are oriented away from it with local deviations of 20° or less. In mammals, a striolar region is present. In turtles, two bands of type I cells are present on opposite sides of the orientation dividing line.

Hair cells in the macula of the utricle are also arranged in a specific pattern, but they do not have their kinocilia facing in a single direction. Since the cells are not polarized in a uniform direction, it allows the utricle to respond to tilt or to linear acceleration in any one of several directions. The pattern in utricle hair cell arrangements is that the axes of the hair cells all point toward a single curving region called the striola (Figure 1.24). As a result, some hair cells vary in direction by 180°. The striolar region is marked by specialized hair cell morphologies, an increase or decrease of hair cell population density, and some modification of the gelatinous and calciferous structures as seen in Figure 1.25. Therefore, tilt of the head in any direction depolarizes some macular hair cells and hyperpolarizes others. The dual signal mostly aids in providing the brain with an accurate measure of head position.

In the utricle, different hair cell types tend to be distributed in relation to contours of the striola. In mammals, nearly two-thirds of the striola hair cells, but only one-half of the extrastriolar cells, are type I. In turtles, type I cells are located in one elevated, striolar belt (Figure 1.24) [Lewis, *et al*, 1985].

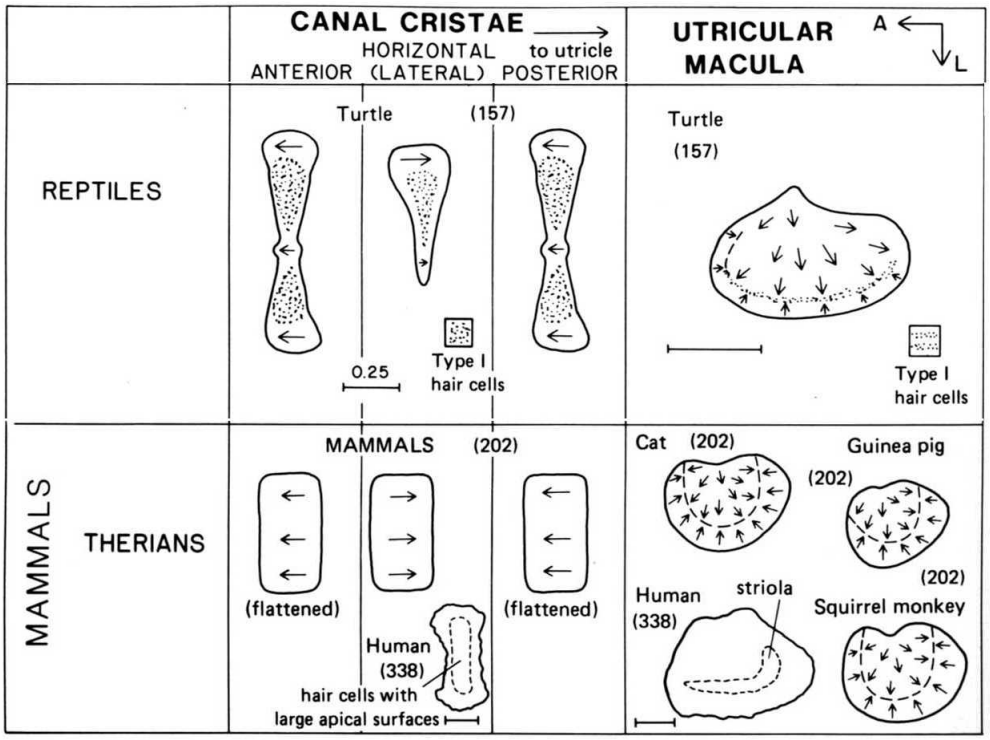

Figure 1.24 Location and direction of hair cell types in vestibular organs. (Lewis, *et al*, 1985).

The hair cell type location and direction are compared for reptiles and mammals. Type I cells are predominant in the crista of the ampulla for both mammals and reptiles. The striolar region of the utricle is evident for reptiles and mammals.

This work specifically examines the utricular hair cells from the turtle, Trachemys (Pseudemys) Scripta. The macula of this particular utricle contains four categories of hair cells. The first and most predominant hair cells found in the utricle are in the category referred to as the medial type II hair cells (Figure 1.26). These cells are located in a region medial of the striola, called the cotillus. They have kinocilium that average around 14 microns with up to 60 stereocilia in a hair bundle. Their bodies form an elliptical shape when the apical surface is viewed from above (Figure 1.27). The second category is a much less common cell referred to as the lateral type II hair cell (Figure 1.28). These cells are located in a region lateral to the striola and referred to as the rampa. They have very tall kinocilium and also have elliptically shaped apical surfaces. The final two types of hair cells are found in the striolar region. These cells may be type I or type II and their apical surface is more circular than those of the extra-striolar hair cells (Figure 1.27). These hair cells contain up to 100 stereocilia in a particular bundle and are taller than the stereocilia in the extra-striolar hair cells. Striolar hair cells are shown in Figure 1.29.

Using these three organs in conjunction with the hair cell arrangements, nearly any movement or orientation of the head can be sensed accurately. However, if the vestibular system is disrupted in any manner, it can lead to sensory problems. For example, if an excess of endolymph occurs within the labyrinth due to overproduction or improper drainage, it will disrupt the function of the entire system. This could lead to common problems including dizziness (vertigo), nystagmus, and nausea associated with Meniere's disease [Kelly, 1981].

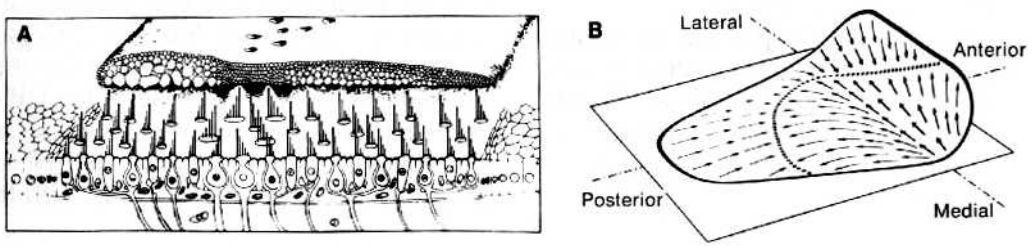

Figure 1.25 Hair cell organization in the utricle (Shepherd, 1988).
A. The hair bundles all have the direction of polarization towards the striola. The axis along which polarization direction changes (the striola) is evident as well as the modifications of the otolith membrane. **B.** Surface view of the macula of the utricle displaying the direction of hair cell polarization.

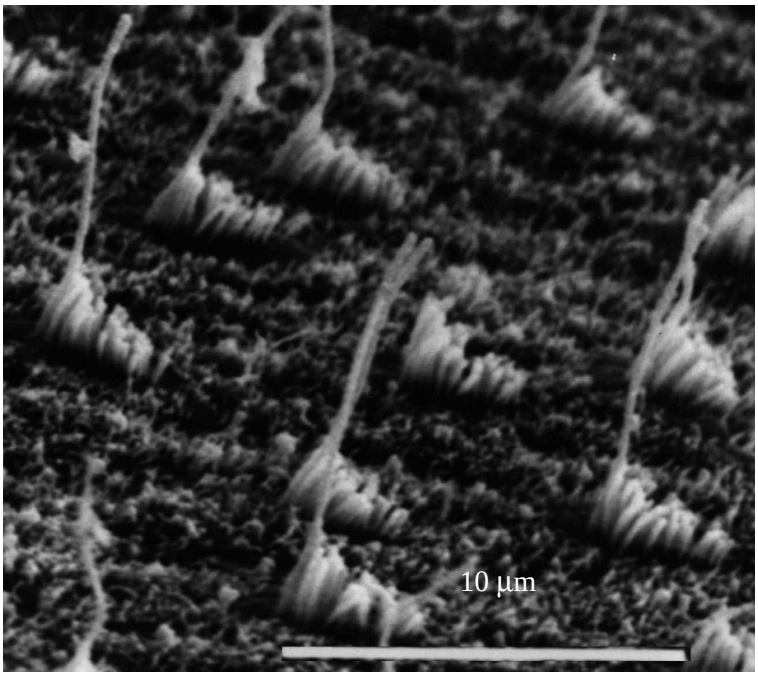

Figure 1.26 Medial type II utricular hair cells of the turtle (Peterson).
The hair bundles are located in the cotillus region of the utricle medial to the striola. They are characterized by longer kinocilium with shorter stereocilia.

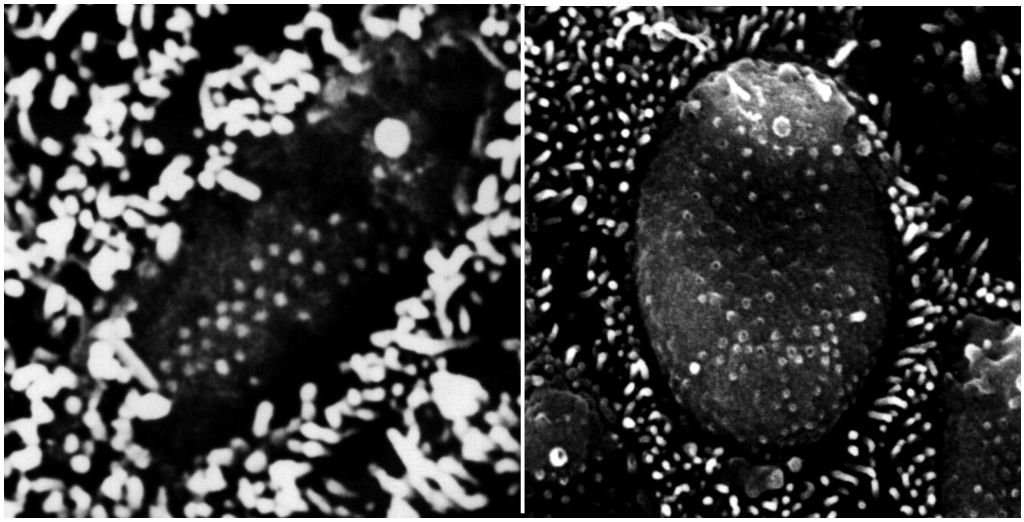

Figure 1.27 Apical surface of utricular hair cells (Peterson).
The hair cells in this figure have been sonicated to remove the cilia. The cell on the left is medial type II and has an elliptically shaped apical surface. On the right is a striolar cell which has more of an oval shaped apical surface. The large white dot in both pictures is the sonicated kinocilium and the remaining white projections are microvilli.

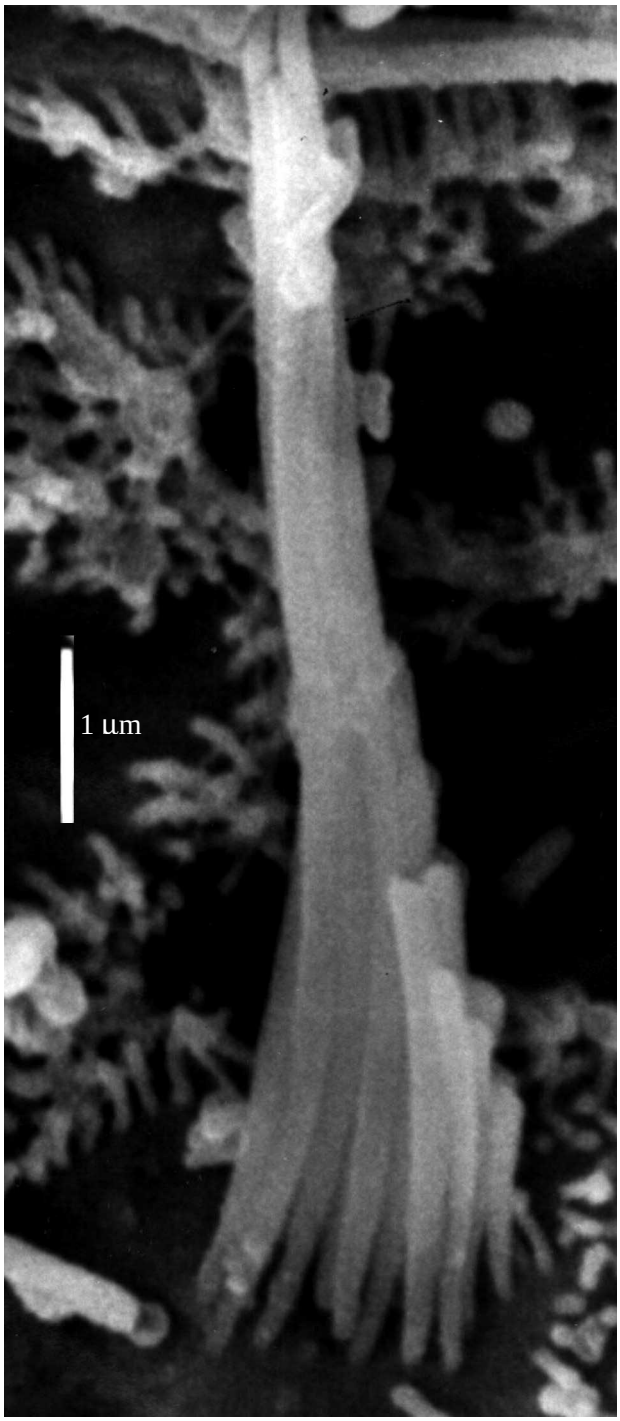

Figure 1.28 Lateral type II utricular hair cells of the turtle (Peterson).
The hair bundles are located in the rampa region of the utricle lateral to the striola. They are characterized by extremely long kinocilium with relatively long stereocilia.

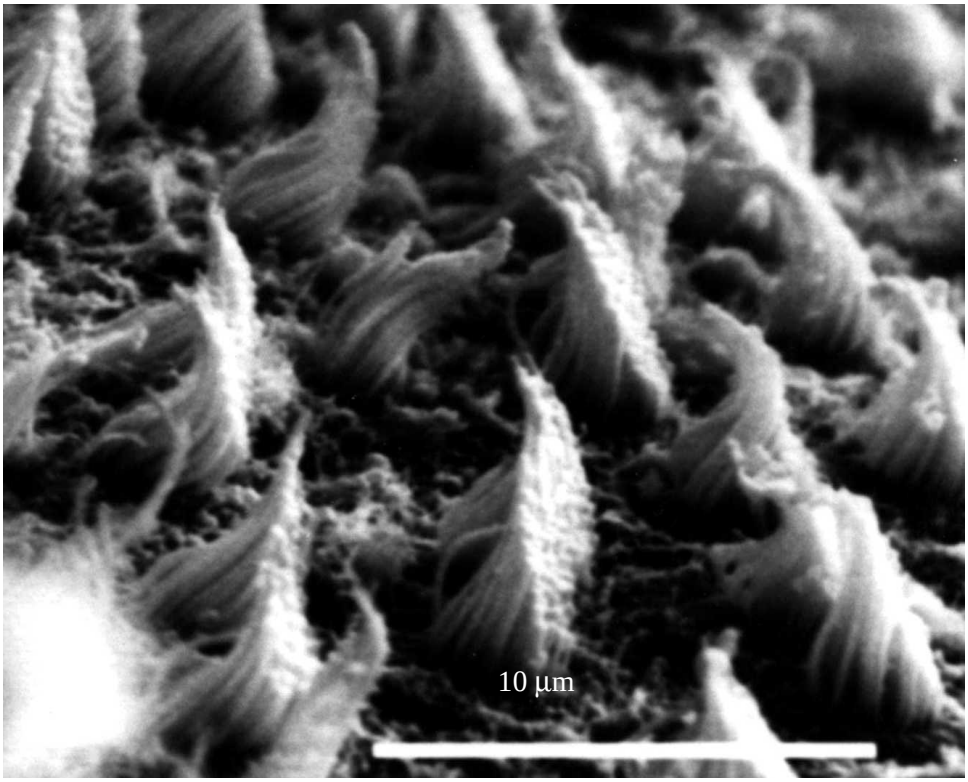

Figure 1.29 Striolar hair cells of the turtle utricle (Peterson).
The hair bundles are located in striolar region. They are characterized by numerous stereocilia taller than those found in extra-striolar hair cells.

1.3 BRIEF HISTORY

As previously mentioned, hair cells are extremely sensitive transducers that moderate the senses of hearing and balance. A small force applied to the top of the cell produces an electrical signal at the bottom. Although the general structure of the hair cell and its sensory role have been known for years, how the individual hair cell works is the current subject of scientific research. The purpose of this research is to concentrate on one aspect of the mechanoelectrical transduction process: the stiffness of the hair cell bundle.

Various methods have been employed by researchers in an attempt to attain reliable measures of hair bundle stiffness. One method involved the use of a glass probe. By pushing or pulling a bundle with a probe of known stiffness, the force on the bundle can be calculated. The displacement of the bundle as well as the displacement of the probe were measured using optical techniques such as photodiode pairs or video microscopy. Knowing the force on the hair bundle and the deflections of the bundle and probe, the stiffness could be calculated using simple kinematics. Other researchers have used a water jet in place of a glass probe. A stream of fluid from the water jet stimulated the bundle at varying frequencies and the bundle deflections were measured using photodiodes. Again, knowing the deflections and forces, the stiffness of the bundle could be calculated.

Averaged values for hair bundle stiffness have been obtained by various researchers and are reported in Table 1.1 [Szymko, *et al*, 1992]. The stiffness values vary over a wide range which could be the result of numerous factors. One possible influence is that not only are the examined cells from different organs in the vestibular system, but they are also from different animals. Since each different organ has varying functions and capabilities, it is likely the stiffness will and should differ from organ to organ and cell to cell. These values were obtained with methods discussed in depth in the next chapter.

Table 1.1 Experimental stiffness values (Szymko, 1992).

INVESTIGATOR	STIFFNESS ($\times 10^{-4}$ N/m)	HAIR CELL ORGAN
Ashmore (1984)	1.32	frog sacculus
Flock and Streiloff (1984)	7.8 to 34.7	guinea pig cochlea
Streiloff and Flock (1984)	1 to 97.2	guinea pig cochlea
Crawford and Fettiplace (1985)	6	turtle cochlea
Howard and Ashmore (1986)	2.56	frog sacculus
Howard and Hudspeth (1988)	6.3	bullfrog sacculus
Denk, Webb, and Hudspeth (1989)	3.41	frog sacculus
Russell, Richardson and Kossl (1989)	16 to 35	mouse cochlea
Szymko, Dmitri and Saunders (1992)	5.04	chick cochlea

Additional methods and variations of the ones already discussed have been used to determine stiffness of hair bundles. However, they all have their problems and limitations. It is our hope to correct some of these problems and eliminate as many limitations as possible by developing an experimental procedure that utilizes previously used technologies in different techniques.

1.4 MOTIVATION

There are many situations in which the vestibular system may fail and cause a range of effects from dizziness to death. For example, in the weightlessness of space, gravity is non-existent and astronauts may become extremely disoriented. This may limit their productivity and compromise their safety. Fighter aircraft undergo large accelerations which can lead to misleading sensations for the pilot and can result in accidents and loss of life. More commonly, according to the National Ambulatory Medical Care Survey of 1991, there are approximately five million physician visits a year related to vertigo, or dizziness, in the U.S. [Cotton, 1998]. Often this is the result of a disturbance in the pressure of the endolymphatic system [Azzi, 1980] which, in extreme cases, the patient cannot walk, stand, or sit. Nausea as well as nystagmus (rapid eye movement) and tinnitus (ringing of the ear) may accompany the other symptoms.

This work is motivated by a need to understand the normal function of hair cell bundles which are an integral part of the vestibular system. Most techniques used today

to measure mechanical properties of hair bundles introduce significant error and have limitations. The purpose of this research is to take previously developed techniques for measuring hair bundle stiffness, and employ them in new experimental methods. In an effort to attain reliable stiffness values, Fabry-Perot interferometry will be used in conjunction with video microscopy and a photoelectric motion transducer (PMT). Using each of these measurement techniques will provide a means for system calibration and precise displacement measurements. Eventually, the resulting calculated stiffness values will be compared to theoretical stiffness values obtained using computer modeling techniques.

1.5 OBJECTIVE

The main objective is to devise a resourceful and reliable method for measuring the deflection of hair cells in-vivo. This will allow for a better understanding of the mechanics of the vestibular hair cells and provide insight into the role hair cells play in the mechanoelectrical transduction process that occurs in the cell.

The specific objectives of this research are:

- develop a method for proper dissection of the vestibular system from a turtle, Trachemys (Pseudemys) Scripta
- fabricate glass whiskers and calculate their stiffness and dimensions
- use piezoelectric micromanipulators to hold glass whisker and apply force to hair bundle
- employ Extrinsic Fabry-Perot Interferometer (EFPI) to measure distance the glass whisker is moved
- construct photoelectronic motion transducer (PMT) to detect movement of bundle
- calibrate PMT using video microscopy and EFPI
- extrapolate linear relationship from calibration in order to accurately measure smaller movements
- conduct experimental trials by applying force to utricular hair bundle while measuring resulting deflections
- calculate the stiffness of the hair bundles
- compare results to previous research and theoretical computer model

This work will demonstrate the accuracy with which the small hair bundle displacements can be measured. The success of this work will determine the amount of continued research necessary to perfect the developed technique. Upon perfection, the stiffness of hair bundles in the utricle and other vestibular organs can be measured in order to help evaluate their mechanical properties.

1.6 OVERVIEW

The following chapter will briefly discuss various methods and techniques developed for measuring the displacements of hair cell bundles. Chapter three will introduce the measurement technique developed in this work. Chapter four will describe the experimental setup and equipment used. Chapter five details the procedure used for preparing the specimen, calibrating the system, and obtaining experimental results. Chapter six will outline evaluation and testing of the experimental system to predict its usefulness. Chapter seven presents the results and discusses the possible implications and success of the experimental technique. Chapter eight will provide a summary and highlight the conclusions. Finally, Chapter nine will point to future considerations for research and ideas for further testing.

2.0 PREVIOUS TECHNIQUES USED TO MEASURE MECAHNICAL PROPERTIES OF HAIR BUNDLES

Over the last 15 years, researchers have worked in developing new techniques for measuring the displacement of a hair bundle so that its stiffness could be calculated. Many of these techniques, whose success depends on its capability to measure extremely small displacements, involve a mechanical stimulus used to deflect the bundle whereas others measure natural motion. A number of these techniques will be explained briefly in the following chapter. This chapter will also highlight the challenges that these techniques face and problems that persist. Our research attempts to circumvent current problems and limitations by using a combination of the techniques discussed below.

2.1 GLASS WHISKERS AND VIDEO MICROSCOPY

One of the earlier methods developed involves the use of a glass whisker to mechanically deflect the hair bundle. The whiskers are manufactured to have a stiffness less than that of the hair bundle so that they will bend when deflecting the bundle. The stiffness of the whisker can be obtained through calibration (section 6.1). The stiffness of the hair bundle can be calculated using simple kinematics when the whisker and bundle displacements as well as the stiffness of the whisker are all known quantities (section 5.4). Many researchers use this method of a glass whisker to stimulate the bundle, but have different techniques for measuring the actual bundle displacements [Howard and Ashmore, 1986]; [Flock and Orman, 1983].

One end of the whisker is usually attached to a larger micropipette which is displaced by a micromanipulator; often the manipulator is a piezoelectric bimorph which makes small displacements accurately. The opposite end of the whisker is in contact with the bundle and moves perpendicular to its long axis (Figure 2.1). As the whisker is displaced, it creates a force on the bundle and leads to an ensuing deflection. For this procedure, the whiskers are commonly 1 μm in diameter and 0.25 to 0.7 mm in length [Flock and Streiloff, 1984].

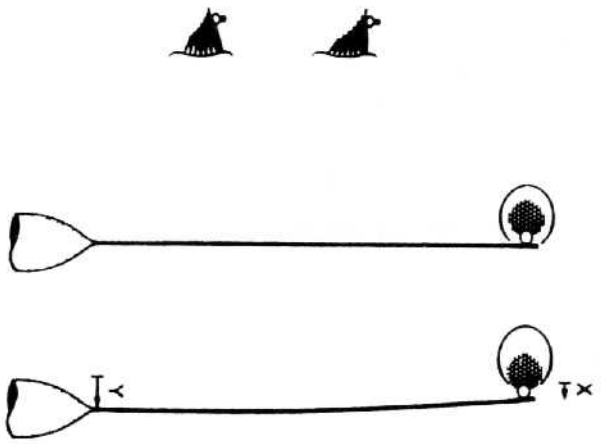

Figure 2.1 Glass whisker stimulation (Howard and Hudspeth, 1988).
A glass whisker is used to mechanically deflect the hair bundle. The whisker is attached to a larger pipette and is moved by a micromanipulator. The difference in the Y and X displacements can be used to determine the bundle stiffness (not to scale).

The simplest way to obtain data would be to apply enough force with the whisker on the bundle to deflect the bundle 1 μm. This deflection can be seen through a microscope or by photographic means. Since the deflections are known as well as the whisker stiffness, the bundle stiffness could be calculated. However, there are a number of flaws in this method that could severely effect the resulting calculation. One major flaw is the inaccuracy that accompanies trying to measure a 1 μm displacement using photography. A second problem is that the physiological deflections that the hair cells endure are believed to be smaller than 1 μm; more likely a maximum of ~300 nm. Therefore, these larger displacements could destroy the tissue and alter its mechanical properties. Finally, in the past, researchers' results were limited by the accuracy of the displacements of the piezoelectric bimorphs. If the bimorphs are incapable of accurate displacements less than 1 μm, then the researcher is limited to deflections of 1 μm or more.

Improvements in this technique have been made in recent years. There have been developments of tools such as video rulers. These are used to measure deflections seen on a monitor that displays the movement taking place underneath the microscope. However, this method is subject to the limits of light microscopy and resolution. There are other methods that have been developed to further increase the capabilities of light microscopes such as video and digital image processing [Sheetz, *et al*, 1988].

2.2 WATER-JET AND LIGHT MICROSCOPE OPTICS

The use of a glass whisker is not the only method available to mechanically deflect a hair bundle. Initially, a micro-syringe apparatus was used to deflect hair bundles [Flock and Orman, 1983]. This design was later modified and evolved into a water microjet that was used to stimulate hair cell sensory bundles [Saunders and Szymko, 1989]. In this technique, a piezoelectric crystal drives a small stainless steel bellows. One end of the bellows is fitted with a plug that mates to the threaded end of the crystal. The other end of the bellows is also fitted with a plug designed to accept a 1.2 mm glass pipette. The total inside volume is approximately 0.3 cc. This device is depicted in Figure 2.2 which shows how the end of the bellows with the pipette is secured while the end attached to the crystal is free to move back and forth as it is driven. The entire device was attached to a micromanipulator which was used to position the waterjet close to the desired target.

Further modifications were made to this design by Saunders and Szymko (Figure 2.3) by eliminating the bellows and increasing the output voltage. The bellows was replaced by a conical chamber with a piston rod in its center that was mated to the driving shaft of the crystal. A thin plastic diaphragm was then inserted into the open back of the chamber. When the crystal was driven sinusoidally, a pressure wave, generated by the diaphragm, was propagated through the fluid of the chamber and the capillary rod to the pipette tip. This produced a water jet stimulus at the pipette tip. The water jet was then calibrated using a TV monitor, frame-grabbed image, or photodiode array (discussed in section 2.3) with glass beads [Saunders and Szymko, 1989] or glass whiskers [Huang, 1991].

Experimentation on hair bundles has been done in which an isolated hair cell was separated from the sensory epithelium and placed under a Zeiss UEM microscope [Huang, 1991]. The bundle was placed on the midline of photodiode plates and the waterjet was positioned within microns of the cell. The cell was stimulated at different frequencies and the resulting displacements were measured. There are some potential

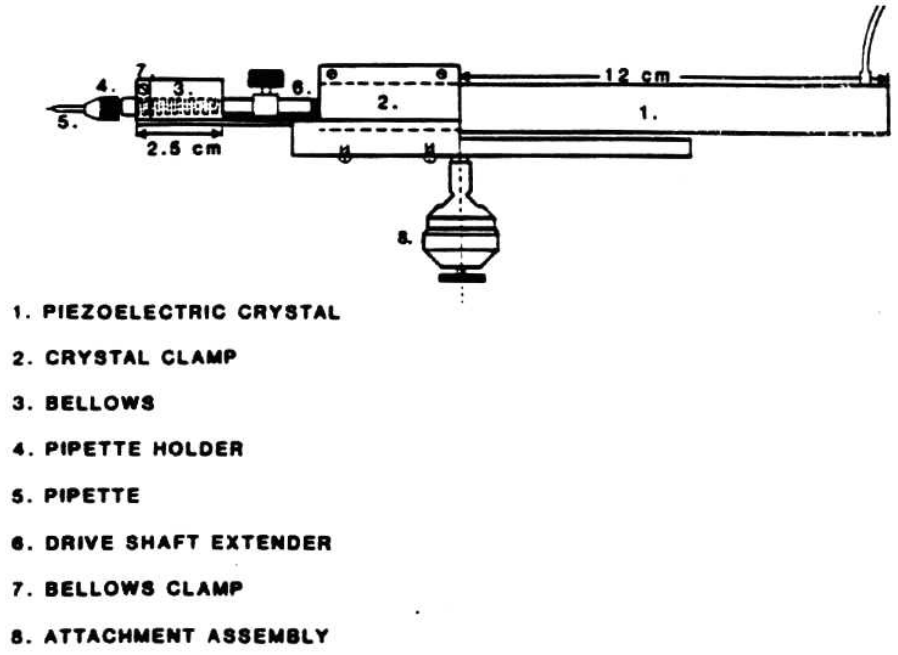

Figure 2.2 Micro-syringe apparatus (Saunders and Szymko, 1989).
This device was originally used to deflect hair cells by producing a water-jet perturbation.

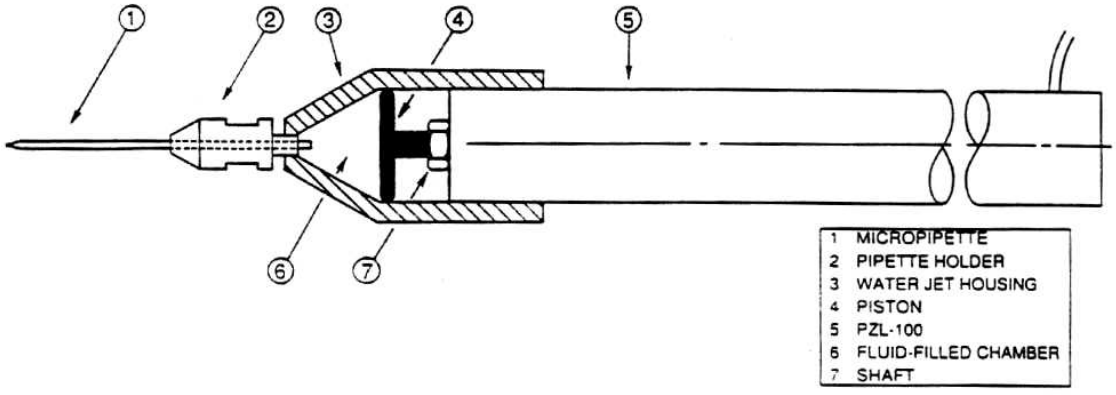

Figure 2.3 Water –jet apparatus (Szymko, Dimitri, and Saunders, 1992).
This device is a modification of the previous micro-syringe apparatus. Used as an alternative to a glass whisker for displacement of hair bundles.

problems with this technique. Most obvious is that the removal of a single hair cell from its surroundings will be very traumatic to the bundle. This could alter its properties or damage the tissue. Also, the waterjet stimulus often causes the hair bundle to make movements in excess of its physiological deflections which could also damage the tissue. Finally, the calibration of the waterjet is difficult and could introduce significant error.

2.3 GLASS WHISKERS AND PHOTODIODES

The use of photodiodes has enabled researchers to accurately measure displacements under 1μm. In this technique, researchers use a glass whisker or a water jet to apply a force to the bundle as discussed in the two previous sections. They then use a photoelectric motion transducer (PMT) along with light microscope optics to determine the hair bundle displacements [Howard and Hudspeth, 1988], [Crawford and Fettiplace, 1985], and [Kazahaya, 1989]. The PMT is a measuring device comprised of a power supply, a dual-diode array, and a differential instrumentation amplifier. The details of this arrangement are discussed in sub-section 3.2.1 and a diagram of the photodiode field projected onto the whisker and bundle is shown in Figure 2.4.

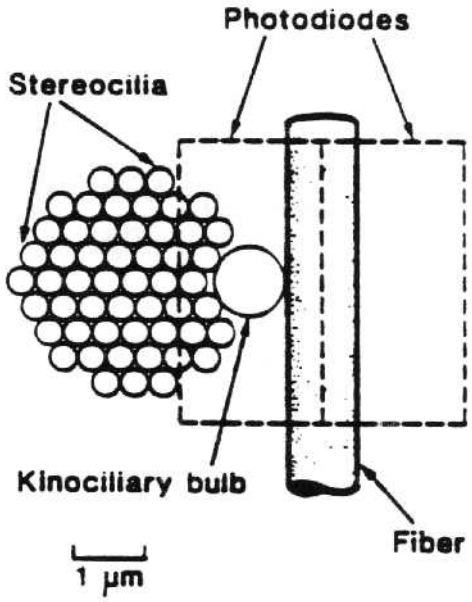

Figure 2.4 Photodiode field of vision (Howard and Hudspeth, 1988).
This illustration shows the alignment of the whisker and bundle in the field of the two photodiodes.

In this technique, the hair bundle is positioned under a microscope with a 40x water immersion objective. The image of the bundle is projected through an optivar, which further increases the magnification, and then focused on the double photodiode array. The setup that Crawford and Fettiplace used is depicted in Figure 2.5. The magnified image of the bundle must not exceed the dimensions of the photodiode array. The photodiodes detect light and transduce it into a current. The currents from each diode are transmitted to the differential amplifier where they are changed into voltages. The amplifier takes the difference between the two voltages and then increases it. Therefore, if the diodes see the same amount of light, the output from the differential amplifier will be zero. So, in this technique the image of the bundle is centered on the array at the midline between the two diodes. As the image of the bundle is deflected and moved from the center of the diode array towards one diode or the other, the amount of light the two diodes detect is no longer equal and will alter the voltage they output. The difference between diode outputs and, therefore, the output from the differential amplifier will no longer be zero. The difference in the voltages between the two diodes is proportional to the displacement of the image. Calibrations are done to find the relationship between the displacement of the bundle and the output of the voltage from the PMT.

Crawford and Fettiplace were able to achieve detection of displacements in the range of 1 – 500 nm [Crawford and Fettiplace, 1985] with this system, which is much closer to physiological range than the methods discussed in the previous two sections. However, there are also potential difficulties with this method. A major problem is that since the diodes are very sensitive to a change in light, they must be illuminated equally which requires a very good light source. Also, since the voltages created by the photodiodes will be small, they may be susceptible to interference and noise. Therefore, eliminating disturbance sources, isolating the platform being worked on from vibrations and a large signal-to-noise ratio are imperative. Finally, calibrations done to find the voltage-displacement relationship are difficult and must be done prior to performing each test. These calibrations are only valid for all of the exact conditions for a specific test and will change based on hair bundle, whisker size, light intensity, and numerous other variables.

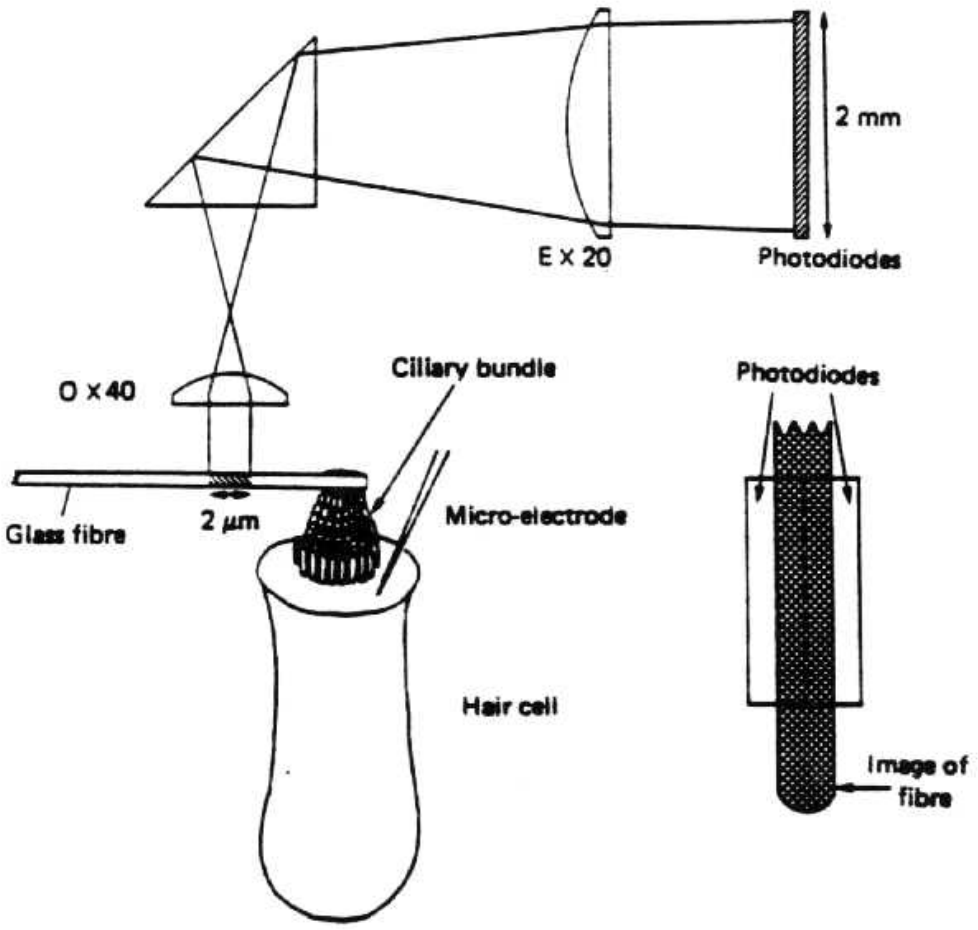

Figure 2.5 Photodiode setup (Crawford and Fettiplace, 1985).
This system was used to measure the bundle displacement. The researchers examined a 2 µm section of the whisker. The image was projected through a 40× water immersion lens and a 20× eyepiece onto the photodiodes. The bundle was deflected with the glass whisker and the displacement was measured by the change in photocurrents between the two diodes.

2.4 FABRY-PEROT INTERFEROMETER

Another technique used to measure the deflection of a hair bundle is a Fabry-Perot interferometer system. The Fabry-Perot sensor is often used in conjunction with a glass whisker similar to those described above. The whisker applies a force to the bundle and the sensor measures the resulting deflection [Barrett, *et al*, 1999]. Once again, in knowing the deflection of the bundle as well as the movement and stiffness of the whisker, the stiffness of the bundle can be calculated.

In this technique, a laser beam travels through a fiber optic cable and is aimed at a reflective object; in this case the object is the hair bundle in a fluid medium. The laser reflects off of the bundle and a portion of the reflected light travels back up the fiber. The sensing fiber of the Extrinsic Fabry-Perot Interferometer used by Grant and Barrett and created by Luna Innovations (formerly F&S, Inc.) is shown in Figure 2.6. The reflected light from the bundle interferes with the light that reflects off of the fiber/water interface. The interference of the two light waves creates a new wave with a different intensity and phase shift than the light reflecting from the fiber/water surface. As the bundle is moved so that its position with respect to the fiber changes, so does the interference pattern between the two reflected light beams. This phase shift will cause an intensity change that enables the distance between the sensor tip and the reflective material to be determined.

This system can be very useful because it can detect small displacements in the nanometer range. The sensor can also be positioned to measure the deflection at any part of the bundle, not just where the whisker makes contact. Also, this technique requires minimal destruction of the tissue due to folding or placement which is important in regards to viability and physiologic concerns. However, this system will be very unstable unless there is an adequate amount of light reflected back into the sensor tip. Unfortunately, this means alignments need to be precise and the reflective object must be positioned so that the sensor tip can receive the reflected beam. Also, in regards to this specific case, biological tissue is not very reflective and may not offer enough reflected light for proper sensor operation.

Figure 2.6 Fabry-Perot Interferometer.
This drawing shows the EFPI sensor emitting an incident laser beam. The sensor receives back two reflected signals: reflection from the fiber/water interface (R1) and reflection when the laser reaches a target (R2). The target is a ciliary bundle being displaced by a glass whisker. The interference of these two reflections will allow for the calculation of the distance the target is from the sensor.

2.5 OPTICAL LASER DIFFERENTIAL INTERFEROMETER

Not all methods used to measure hair bundle movements require the use of a mechanical stimulus. Optical laser differential interferometry allows the detection of natural hair bundle movement without a mechanical stimulus to deflect the hair bundle. The natural movement of an object suspended in a fluid due to collisions with molecules of the fluid, known as Brownian motion [Encarta Webpage], has been correlated to the stiffness of that object [Denk, *et al*, 1989].

In this technique, light from a He-Ne laser travels through a beam splitter that splits the beam into two orthogonally polarized beams. Both beams have a diffraction-limited focus of 0.5 μm in diameter and their parallel axes are separated by 0.2 μm. As an object with a different refractive index than water moves between the two foci, it increases the interaction with one beam and decreases the interaction with the other (Figure 2.7). The interference between these two beams is consequently changed which results in a change of the relative phase of the beams. This phase shift produces a change in intensity level where the beams interfere and it is sensed by a photodetection system

(similar to that discussed in section 2.3). The change in intensity seen by the photodetector is used to determine the Brownian motion.

The optical setup used to measure the Brownian motion consists of an inverted microscope with Differential Interference Contrast (DIC) optics and an upright microscope. The inverted scope focuses the beam pair on the object while the upright scope acts as a condenser and collects light after it passes through the specimen. A He-Ne laser emits light through a gradient index (GRIN) lens into a single mode optical fiber and then into another GRIN lens in order to couple the laser light into and out of the fiber. The light then enters the inverted microscope through a 25x eyepiece passing through a polarizer and a quarter wave plate. It is then combined with light from a tungsten filament. Next, both lights pass through the first DIC-slider to a lower objective (40x, N.A. = 0.75, water-immersion), then trough the preparation, followed by another upper objective lens (40x, N.A. = 0.75) and second DIC-slider located in the upright microscope. Part of the incandescent as well as the laser light are used for direct observation through a camera/video system, while the remaining portion passes through a filter that allows the laser light to reach the photodiodes.

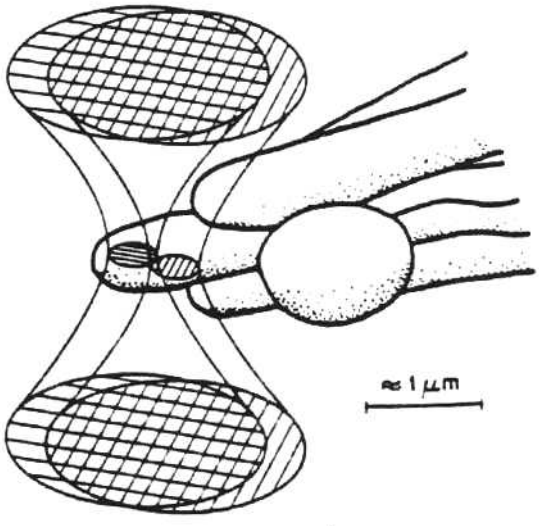

Figure 2.7 Double focus of the split laser beam (Denk and Webb, 1989).
The original laser beam is split into two orthogonally polarized beams. The two beams are focused on the tallest stereocilia which is positioned horizontally. The interference of the stereocilia will alter the interference pattern.

There are a few problems with this technique. First, the researchers used chemicals to remove the otoconial layer and the nerves which can alter the mechanical properties of the tissue. Second, calibrations in this technique with the photodiodes will be very difficult to perform accurately. Finally, this measurement technique will be very sensitive to external noise and vibrations. However, this method, if done correctly, could prove useful because no mechanical stimulus is needed to deflect the bundle.

3.0 DEVELOPED TECHNIQUE TO MEASURE MECAHNICAL PROPERTIES OF HAIR BUNDLES

This chapter will explain the steps we took in devising our technique for measuring the stiffness of utricular hair cell bundles. It will explain the reasons for our decisions and the advantages of our system.

3.1 INITIAL EFFORTS

In our initial efforts to measure the stiffness of utricular hair bundles, we hoped to use glass whiskers to deflect the bundles and the EFPI technique, discussed in section 2.4, to measure the magnitude of this deflection. However, for months we attempted to measure the bundle deflections with numerous variations of this technique without much success. We began by trying to point the EFPI sensor at a 1-3 micron glass whisker and measure the simple displacement of the whisker in air in order to evaluate the capabilities of the system. Not only was it difficult to properly align the sensor with the whisker, but we could not seem to get an intense enough reflected signal from the whisker for the EFPI system to properly work. We contemplated coating the whisker to improve reflectivity, but then realized that the biological tissue, whose deflection we would be attempting to measure in actual tests, could not be coated since that would alter its mechanical properties. To complicate matters, the actual tests with utricular hair cells would be done in a fluid medium which would further reduce the reflected light signal. Therefore, after consultations with the manufacturers of the system and continuous failures at achieving results, we concluded that we should pursue other alternatives for measuring the distance the hair bundle is deflected by the glass whisker.

We next decided to research the capabilities of video microscopy in measuring small displacements. We hypothesized that if we could see the whisker deflecting the bundle on a monitor, then we could possibly measure the distance moved. We found two potential ways of doing this. One method involved the use of a video ruler. This type of equipment, such as the Imagen XR 2001, can be calibrated using a known scale, but its resolution is accurate at a few microns and limited to hundreds of nanometers. Although it could be used as the primary measuring device, we felt the limits on resolution would

not be small enough to accurately measure a 300 nm deflection, which is the maximum deflection the bundles naturally experience and the magnitude we intended to displace them. The second method was to conduct a cross-correlation analysis on a digitized video frame of a digitally enhanced image. Although this technique was proven to produce the needed resolution [Gelles, *et al*, 1998], the cost of the equipment exceeded our budget constraint and we were not familiar enough with the technique to commit to its use in the project.

Finally, we decided to attempt to use a method developed by other researchers described in section 2.3, the photodiodes. These photodiodes could be used along with a differential amplifier, filter, and dual power supply to form a photoelectronic motion transducer (PMT). Other researchers reported that this technique could achieve nanometer scale displacement detection with reasonable accuracy through data extrapolation. We found that the PMT could be custom made and therefore decided to pursue this technique further.

3.2 DEVELOPMENT OF THE DISPLACEMENT DETECTION SYSTEM

We recognized that to effectively measure the stiffness of a utricular hair bundle, the designed system would need to satisfy specific requirements and remain within certain constraints. The two most important requirements were the accurate measurements of both the pipette displacement and the corresponding bundle deflection when displaced by the whisker. In order to be effective, the techniques used to measure these displacements must be able to detect movement in the nanometer range. We also would need an accurate method of measuring the dimensions of the hair bundles and the whisker. This technique would require measurements of dimensions as small as a few hundred nanometers.

3.2.1 Measurement Technique for Bundle Displacement

The bundle was displaced using a glass whisker between 1-3 microns in diameter. We chose the glass whisker as the stimulus used to displace the bundle rather than the water jet mentioned in section 2.2 because we can more easily control the magnitude and

direction of the displacements. A water jet can cause the hair cells to move beyond their natural physiologic range and also can create complex movement patterns due to fluid flow and impact with the bundle and surrounding tissue.

In order to accurately measure the displacements of the bundle, we constructed a photoelectronic motion transducer (PMT). This system, which was introduced in section 2.3, consists of a dual power supply, differential instrumentation amplifier, low-pass filter, and a dual photodiode array. These components are explained in more detail in Chapter 4. A microscope with DIC optics will be used to view the hair bundle and the image will be projected onto the photodiode pair attached to the top of the microscope. Essentially, the photodiodes will detect a change in light intensity and location as the image of the bundle and whisker in contact is displaced between the boundaries of the two diodes (Figure 2.4). The differential amplifier will output a voltage that shows the change in output between the diodes, while the power supply provides a voltage source for the diodes and the amplifier. System calibrations will find a linear displacement-voltage relationship for the central region of the diodes, explained in section 5.3, which will be used in the calculation of the actual displacement of the hair bundle.

3.2.2 Measurement Technique for Pipette Displacement

The whisker used to force the bundle is bonded to a pipette which is, in turn, attached to the micromanipulator. Prior to testing, the whisker is moved without a bundle present to calibrate the PMT. The whisker's displacement will be equal to that of the pipette and is necessary to calibrate the system. During tests with hair bundles, the pipette will be displaced which will cause the whisker tip to apply a force on the bundle. The pipette displacement will now be different than the whisker displacement since the end of the whisker will encounter the bundle. We need the distance the pipette is moved for comparison with the bundle displacement (equal to the whisker tip displacement) measured by the PMT. The pipette displacement needs to be measured accurately, or it will seriously affect the stiffness calculations.

The micromanipulator is controlled by a set of dials referred to as the Axis Control Unit (ACU). Initially, we planned to purchase or create a scale on the dial so that we could tell how far we had turned the dial during testing. However, we were unable to

locate a pre-fabricated dial that included a ruler and we doubted our ability to accurately create a circular scale that would measure nanometer displacements. Therefore, we decided to apply technology with which we were already familiar. We consulted with Luna Innovations and decided that the Extrinsic Fabry-Perot Interferometer could be used to measure the displacements the micromanipulator made to move the pipette. In order to get the maximum response from the fiber optic sensor used in the EFPI, it should be aligned with a reflective fiber using an alignment sleeve. As a result, we manufactured aluminum pieces to fit the micromanipulator and hold the sensor and reflector in place while they were kept in proper position with respect to each other by the alignment sleeve. In this fashion, accurate measurements with nanometer resolution could be made of the pipette displacement.

3.2.3 Microscopy and Video Measurements

As mentioned earlier, the specimen will be viewed with a microscope equipped with immersion lenses and DIC optics. This will increase the contrast of the image and make it easier for the photodiodes to detect movement of the bundle and whisker. A video camera is used to transmit the image to a monitor for further magnification so that dimensions and displacements can be measured using video equipment. A video ruler, the Imagen XR-2001, can be used to measure the diameter and length of the whisker used in testing, the height and width of a specific bundle, or other dimensions. The video ruler can also be used as a third method for measuring whisker displacement during calibrations. Although it does not have the resolution of the EFPI or the PMT, the Imagen XR-2001 can be used to verify that the other two measurement techniques are working properly for larger displacements in the micron range.

3.3 ADVANTAGES

The method used in this work involves a number of advantages over the techniques previously mentioned in Chapter 2. The glass whisker will be used to stimulate the hair bundle as opposed to a water micro-jet because the applied force will provide for a much simpler situation and less potential for introduced complexities. This whisker will be positioned near the hair bundle using a piezoceramic micropositioner controlled by the experimenter. Attached to the micropositioner is the Fabry-Perot

Interferometer. The interferometer is the selected technique for measuring the whisker and pipette movement during calibrations and only the pipette displacement during actual tests. This system is far better than reading displacements from a scale and is extremely accurate to the nearest nanometer especially since it will use a reflective fiber as well as an alignment sleeve. The PMT is the method of choice for determining the displacement of the whisker during calibrations and the displacement of the bundle during actual tests. This method was preferred because it is affordable, we were able to construct and customize it, and it did not propose the difficulties of other methods, such as the EFPI, with measuring displacements in a fluid medium. Also, the PMT has the capability of measuring nanometer displacements and, with precise calibrations, will provide accurate results. The calibration of the PMT (discussed in detail in Chapter 5) will be done using the Fabry-Perot interferometer and, for added accuracy, will be compared with measurements from a video ruler. Finally, the actual preparation and stimulation of the bundle will result in minimal tissue damage and the tests will only displace the bundle within its natural physiologic range.

Chapter four will explain in greater detail the experimental setup and equipment used for testing and data collection that were introduced above. It will also explain in more detail the theory behind the techniques involved and how the stiffness of a bundle may be found from experimental data.

4.0 EXPERIMENTAL SETUP & EQUIPMENT

This chapter will discuss the experimental setup used to measure the stiffness of a utricular hair cell bundle. The necessary equipment for the experimentation will also be described in detail.

4.1 EXPERIMENTAL SETUP

The vestibular system is dissected out from the ear of *a Pseudemys (Trachemys) scripta elegans*, red-eared slider turtle. The saccule, semicircular canals, and other surrounding structures are removed in order to expose the utricle. The utricle is pinned down on a cover slip containing lactated ringer's solution and viewed with a Zeiss Axioplan microscope. The Zeiss microscope is equipped with differential interference contrast (DIC) which produces optical sectioning of the viewed object and enhanced contrast between edges [Inoue and Spring, 1997]. The light source for the microscope is a Zeiss 100 illuminator (12V 100 W halogen bulb) and is powered by a Zeiss DC power supply (12V 100W). The image formed by a water immersion objective (Zeiss 40× achroplan; N.A. 0.75) and magnified by an optivar slide (1.6×) is viewed through 10× oculars.

Once the utricle is placed under the microscope, the DIC optics are adjusted and the object is put into focus. The microscope is used to locate and magnify a single hair bundle on the sensory epithelium. A glass whisker with predetermined stiffness is then maneuvered into position up against the bundle with the micromanipulator (Burleigh PCS-5000). The Fabry Perot system (Luna Innovations AFSS-PC v3), whose sensor is hooked to the micromanipulator to determine pipette displacement, is now turned on and checked for a good signal. The image of the bundle seen through the microscope oculars also travels up through a beam splitter (Zeiss) to the photodiode pair (EG&G UV 140-2) and a video camera (Dage-Mti DC 200). The video camera feeds into a monitor (Sony Trinitron Color Video Monitor) on which the image can be seen and is magnified. The input voltage to the photodiode pair is supplied by a dual power supply (HP E6360A) and the output from the diode is monitored with both a digital storage oscilloscope (Tektronix 2220) and a digital multimeter (Keithley 197). Once the experimental setup is complete,

the whisker is used to apply a force to the bundle. The displacement of the pipette is measured with the Fabry-Perot system and the bundle displacement is measured using the photodiode pair. This information is then used to calculate the bundle's stiffness (see section 5.4).

4.2 EQUIPMENT

4.2.1 Extrinsic Fabry-Perot Interferometer

Fiber optic phase sensors use configurations, such as Fabry-Perot, to detect information, such as magnitude or direction, of a perturbation (i.e., strain, temperature, or displacement). An extrinsic Fabry-Perot interferometer is an optical, phase-shifted instrument that, in this research, is used to detect nanometer displacements. It is referred to as a phase sensor because it uses two signals, a sensing and a reference signal, which interfere with each other to provide an intensity modulation at a detector. In this project, an AFSS-PC system designed by Luna Innovations was used to calculate the necessary displacements.

Unlike laser based interferometric systems, the AFSS-PC sensor system (seen in Figure 4.1) employs a broadband light-emitting diode (LED) as the optical source [F&S, Inc., 1999]. A coherent light signal is transmitted from the optical source and travels down the input/output optical fiber to the sensor head. As the coherent light reaches the end of the fiber, a portion of the incident signal is reflected off the internal face of the fiber and this is used as the reference reflection (R1 in the figure). The remaining portion of the coherent light is transmitted through the end of the fiber and travels a short distance until it encounters the surface whose position is to be measured. In this experiment, the surface is a reflector fiber, which acts as the target. The incident light reflects off of the target, the sensing reflection (R2 in the figure), and reenters the optical fiber where it interferes with the reference reflection. The optical fiber and the reflector fiber are joined by a hollow core fiber, also referred to as an alignment sleeve, because it ensures that the target is in proper position to reflect the light. The sleeve maximizes the reflected signal while minimizing outside interference.

The modified light travels back from the sensor head to the AFSS-PC system where the spectral properties of light are monitored. A signal-processing algorithm is

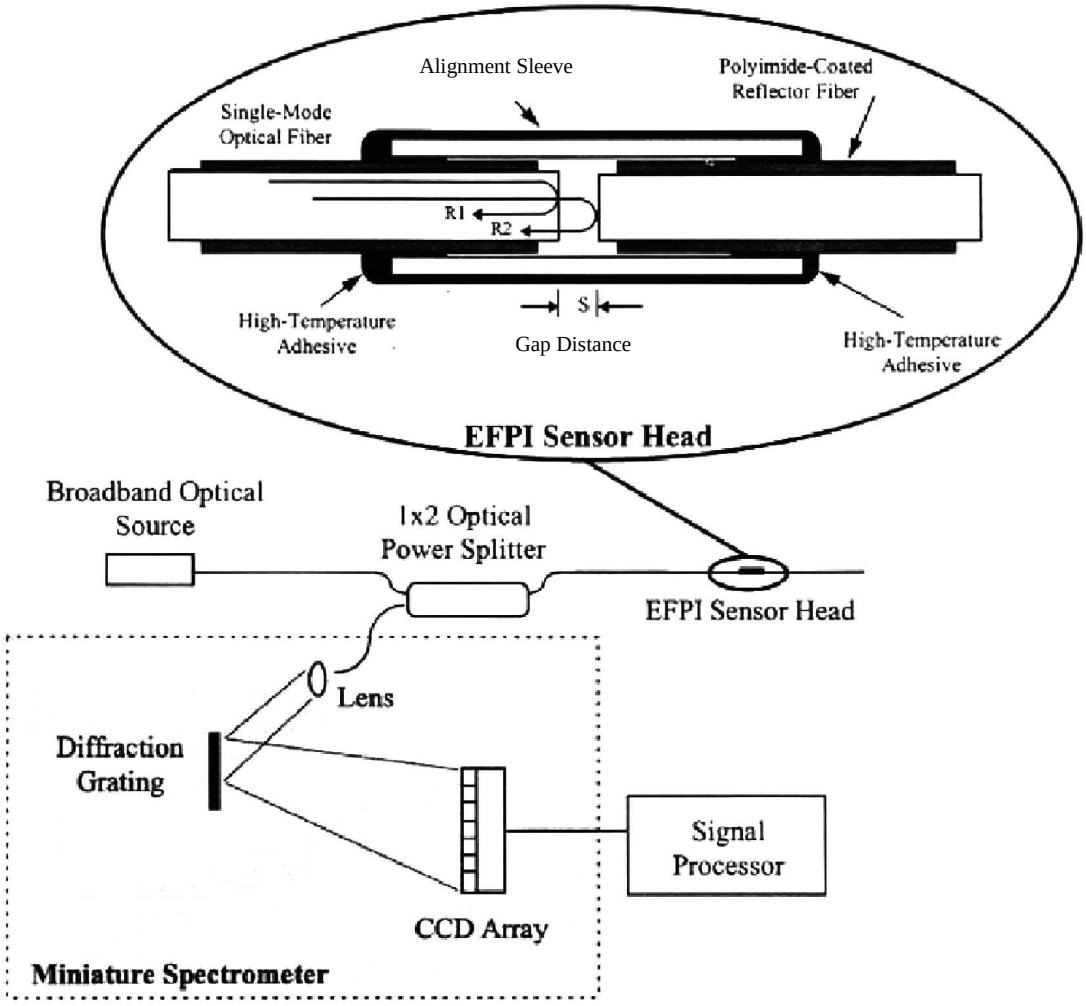

Figure 4.1 EFPI constructed by Luna Innovations (Luna manual, 1999).
This schematic of the AFSS system shows how the EFPI uses the reference reflection (R_1) and the sensing reflection (R_2) to calculate the gap distance (s) between the optical and the reflector fibers.

then used to determine the gap distance, s in Figure 4.1, by analyzing the optical signal returned to a miniature spectrometer from the sensor head. A personal computer as well as LabView code written by Luna Innovations serve to perform the computations for the signal processing and display the resulting gap distance. The program will also display a spectrum plot (an example seen in Figure 4.2) which indicates the quality and strength of the sensor signal [F&S, Inc., 1999].

In this project, the EFPI system will be used to measure the displacement of the pipette as the whisker generates a force on the bundle. The optical fiber will be attached to a stationary portion of the micromanipulator while the reflecting fiber will be fixed to the moving part of the micromanipulator stage. A diagram of the designed plates that held the fibers and attached them to the micromanipulator are shown in Figure 4.3. The L-shaped plate is fixed to the moving part of the stage and will move the reflecting fiber the same distance the pipette is moved. A groove was cut into the aluminum plates for the fibers and clamps were tightened overtop the fibers to keep them in place. An alignment sleeve mated the two ends as to ensure the correct alignment and maximum reflected signal. Since the sensor was not being used in a fluid medium and the sleeve shielded it from open air, the effectiveness of the system was further increased. Using the EFPI is much more accurate than most techniques for measuring the pipette displacement because it can achieve nanometer resolution without much difficulty.

This EFPI system is much improved over older models that required the manual calculations of the gap distance [Barrett, 1998]. However, there are a few difficulties that arise in getting the system to perform correctly. The sensing fiber and the reflecting fiber must both have flat surfaces. Any sharp pieces of glass or slanted surfaces will cause a poor signal or may cause the system to report erroneous data as light reflects from the non-uniform surface. Cleaving both fibers with a diamond tipped scalpel, which is a very delicate process, can prevent this. However, if it is done correctly, it is not difficult to achieve a strong signal with a spectrum plot as seen in Figure 4.2. A constraint on the system is that it works best when the gap distance is between 30-80 microns. A gap distance smaller than this cannot be measured. However, we have seen that very good spectrum plots can often be achieved at gap distances up to 200 microns.

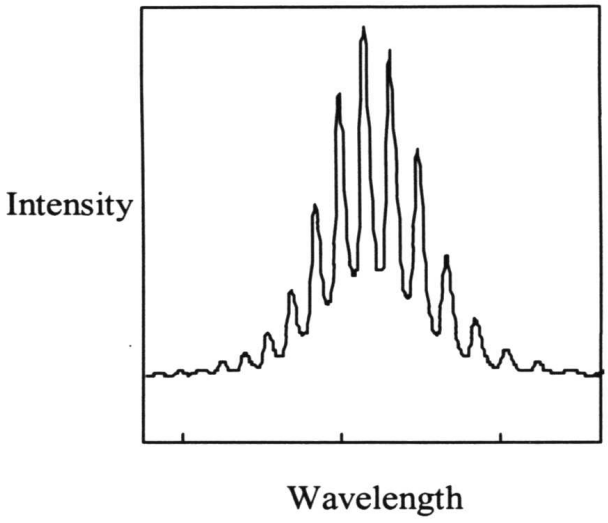

Figure 4.2 A Spectrum plot of AFSS-PC signal (F&S Manual, 1999).
The spectrum plot indicates that a quality signal is being received by the EFPI sensor which is necessary for accurate readings. It also shows that the offset controls and the drive current are adjusted properly.

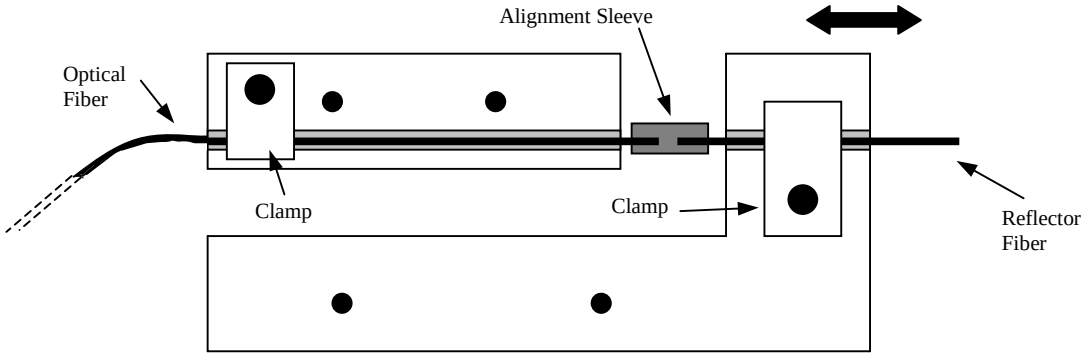

Figure 4.3 Plates for attaching EFPI to the micromanipulator.
The two aluminum plates are screwed into the micromanipulator. The L-shaped plate is attached to the movable stage. The fibers sit in a groove while clamps hold them in place. As the stage moves the pipette back and forth, the reflector moves within the alignment sleeve, thus changing the gap distance.

4.2.2 Photoelectronic Motion Transducer (PMT)

Silicon photodiodes are semiconducting devices that detect light and convert it into an electrical signal (current) [EG&G Catalog]. The amount of current generated is proportional to the intensity of the light to which the diode is exposed. As a result, photodiodes create a linear relationship between the amount of light shone upon them and the voltage they output. The ability of the diode to create this linear relationship can be applied to the measurement of small displacements.

Diodes can be mounted side by side and are often used in arrangements of two or four diodes (Figure 4.4). When two diodes are mounted side by side it is referred to as a dual diode array. If the surfaces of both diodes are illuminated equally, they will generate the same current. However, if the illumination on the two diodes differ, then the resulting currents will not be equal. The diode array can be connected to a differential amplifier (Figure 4.5) which will amplify the signal from the diodes, convert the current into a voltage, and calculate the difference between these two voltage outputs. Therefore, if both diodes were to be fully exposed to a certain light source, the differential amplifier would calculate the output voltage to be zero. However, if one diode receives less light due to an object in the path of the light, the differential amplifier will output the difference in the two voltages. If this object were moved to a different position along the diode array, the differential amplifier would produce a second voltage. Knowing these two voltages and the actual displacement that has occurred provides the linear relationship the diodes produce between light exposure and output voltage. The ratio of the change in output of the two diodes to the distance the object that causes the light shift moves will be the linear voltage-displacement relationship of the diodes necessary to calibrate the measurement system. The combination of the dual diode array, the differential amplifier, a low-pass filter and a dual power supply are the components of what will be referred to as a photoelectronic motion transducer (PMT).

The differential amplifier used to determine the difference in voltage output from each diode was constructed on a PC board and is depicted in Figure 4.5. The drawback to

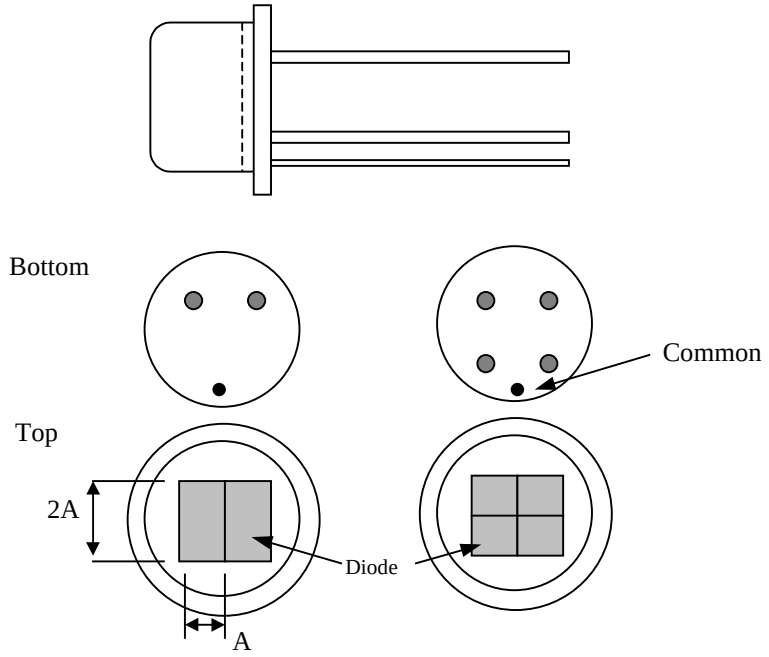

Figure 4.4 Photodiode configuration.
Each photodiode is equipped with one lead per diode along with a common lead. The diodes can be arranged as a dual (left) or quad (right) array. The width of the diode (A) is 1.3 mm while the length (2A) is 2.6 mm. The gap in-between the two diodes is 0.10 mm thick.

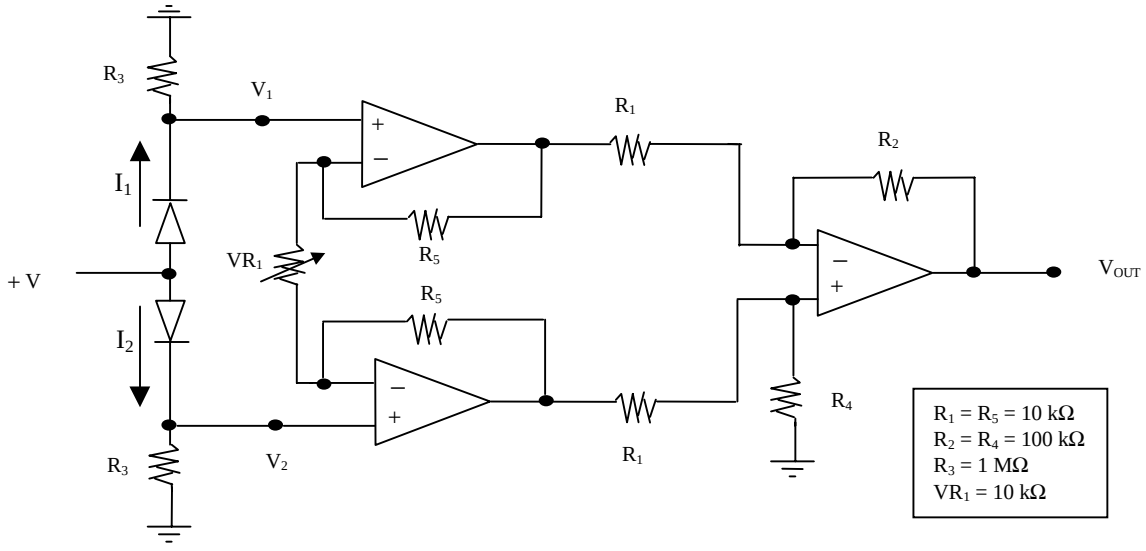

Figure 4.5 Schematic of differential instrumentation amplifier.
The instrumentation amplifier converts the current from the diodes into a voltage, amplifies the values, and then outputs the difference between the two voltages. The variable resistor (VR_1) controls the gain of the circuit. The two currents, I_1 and I_2, are from the photodiodes.

using a differential amplifier is that the absolute incident photon intensity the diodes detect can no longer be measured. However, the advantage is that a relative measurement of voltage output of one diode with respect to the other can be obtained with an increase in signal-to-noise ratio (SNR). Since both diodes will see the same noise, the differential of their outputs will eliminate this noise, thus increasing the SNR.

The configuration of an instrumentation amplifier was used in the design of the differential amplifier (Figure 4.5). The instrumentation amplifier has many advantages including: 1) high sensitivity and accuracy; 2) large common-mode-rejection-ratio; 3) high input impedances; and 4) easy balancing of input amplification and differentiation. This last advantage is very important because a single variable resistor provides a balanced gain control for the entire instrumentation design [Kazahaya, 1989].

The components and materials used to construct the PMT were chosen carefully in order to achieve accurate motion quantization, precise and balanced differential amplification of the input signal, and minimum noise. The diode pair used to detect the change in light was a high sensitivity, dual-element photodiode (EG&G UV-140BQ-2). The instrumentation amplifier was constructed with low-noise, precision operational amplifiers (Analog Devices OP-27-E) and precision film resistors. The precision resistors provided for the balanced differential amplification in the second stage of the instrumentation amplifier. A multi-turn variable resistor provided the balanced gain of the input signal from the photodiode elements. The gain for an instrumentation amplifier is found using the equation

$$G = \left[2\frac{R_5}{VR_1} + 1 \right] \left[\frac{R_2}{R_1} \right] \qquad [4.1]$$

where the values for the resistors are shown in Figure 4.5. The variable resistor can be adjusted between 0 and 10 kΩ. We set the value to 2.222 kΩ. This provides an approximate gain of 100 over the entire circuit.

$$G = \left[2\frac{10}{2.222} + 1 \right] \left[\frac{100}{10} \right] \approx 100$$

The circuit was constructed on a general purpose IC PC board (Radio Shack 276-159 B).

A low-pass filter was used to aid in isolating the photodetector's output signal from extraneous line or circuit noise amplified by the instrumentation amplifier. The filter (Krohn-Hite 3750 R) was set at 200 Hz and did not allow any frequency signals higher than this to pass while causing minimal disturbance to the signal coming from the differential amplifier. A dual power supply was necessary to provide constant, stable DC voltage to the photodiode array and to the operational amplifiers in the instrumentation amplifier. A constant DC supply voltage is needed so that the op-amps can operate at their optimum levels. Any variances in the supply voltage would cause distortion and masking of the true movement of an object being detected by the photodiodes.

The PMT system worked rather well with the exception of a few problems. First, we experienced a low frequency disturbance to which we could not locate the source. We could not eliminate the noise with a filter because it occurred at a frequency near that of our signal. We also tried to use capacitors in the amplifier without success. So, we had to deal with approximately a 1-2 mV voltage jump during data collection. Second, the diodes are very sensitive to influences from external light, which is the reason for the constructed assembly in section 4.2.3. An additional problem was that the circuit itself was subject to influence by external noise and had to be shielded correctly. This problem was also addressed by the enclosure described in the next section. We also had to re-wire the PMT to make sure that we eliminated any ground loops that had been initially created and led to noise problems.

4.2.3 PMT Mounting Assembly

In this project, the photodiode array is mounted above the microscope. The array and the differential amplifier are both housed in an aluminum enclosure (Radio Shack 270-238) to minimize the introduction of external noise into the system (Figure 4.6). Holes were drilled into the bottom of the enclosure and it was screwed down onto an aluminum plate which was then threaded onto a c-mount. The other end of the c-mount was tightly screwed into the top of the microscope apparatus so that there would not be any influence from external light sources. A hole was cut into the bottom of the aluminum enclosure for the entrance of light from the microscope. Two layers of fiberglass were put in the bottom of the housing and a small hole was cut in them in order

to fit the diode. The diode was seated between the two fiberglass pieces and clamped down as to minimize diode drift. A small layer of silicone sealant was spread across the bottom of the diode to ensure a snug fit. The fiberglass pieces were spray painted black so that reflections from the aluminum surface did not distort the diodes' detection of the microscope's light source. The differential amplifier was mounted on the wall of the aluminum housing (Figure 4.7). A hole was drilled in the back of the housing through which leads to and from the circuit could enter and exit the enclosure. The incoming leads carried the power supply to the diode and the outgoing one relayed the output voltage to the lowpass filter and then on to the multimeter.

4.2.4 Micromanipulator

A micromanipulator (Burleigh PCS-5100) was used to hold and precisely maneuver the glass whisker, position the whisker up against a hair bundle, and then displace the bundle by creating a force on it using the whisker. The micromanipulator (Figure 4.8) employed in this project uses piezoelectric (PZT) actuators to make small, precise displacements. PZT actuators are solid ceramic structures that expand under applied voltage and retract when the applied voltage is reduced. Three actuators are oriented in the micromanipulator stages to allow for movement in three orthogonal directions. An Axis Control Unit (ACU) controls the actual movement. The ACU has three knobs that can be turned and correspond to the three directions of motion. The knobs are connected to precision potentiometers. As the knob is turned clockwise, the voltage of the corresponding potentiometer is increased and applied to the PZT actuator, causing the plate to expand. When the knob is turned in reverse direction, the voltage is reduced and the plate contracts [Burleigh manual, 1997].

The potentiometers reach their maximum voltage after three turns of the knob. Therefore, three full rotations of the knob correspond to the full range of the PZT actuator. For the system used in this project, that full range of motion is 300 microns. The position resolution of this system is 0.04%, which provides for 120 nm of resolution for a 300 micron stage.

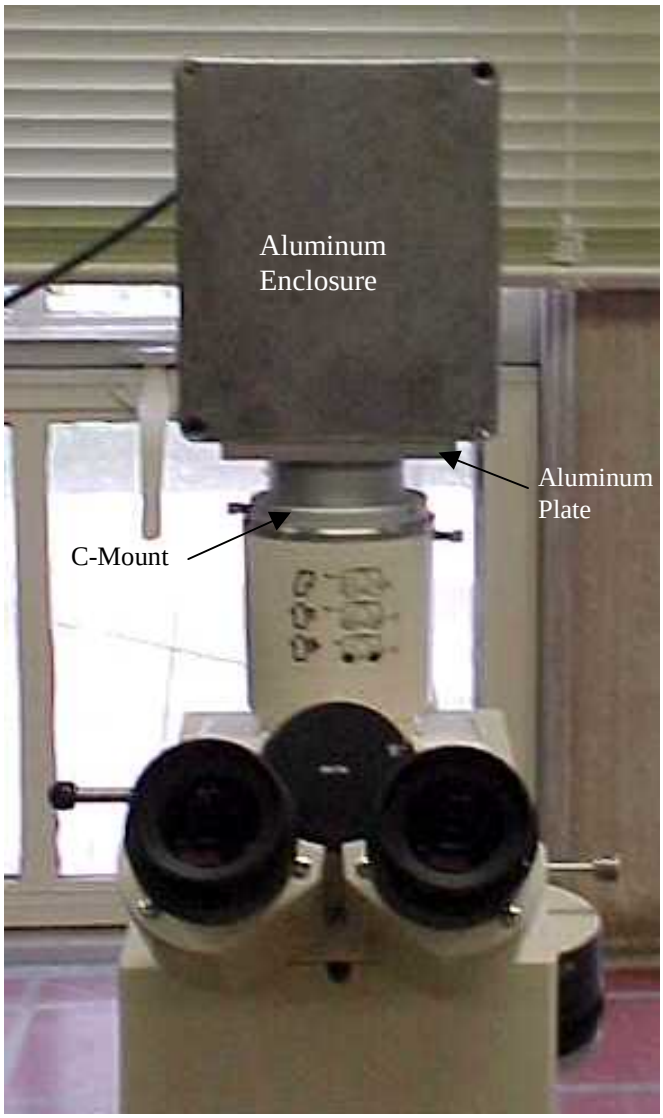

Figure 4.6 Aluminum enclosure.
The aluminum enclosure serves to shield the photodiode and differential amplifier from outside light and noise. It also creates a good connection to the microscope for the diode.

Figure 4.7 Inside of the aluminum enclosure.
The differential instrumentation amplifier circuit was mounted to the wall of the aluminum enclosure. At the bottom of the enclosure the photodiode array is seated between two fiberglass pieces. The leads to the diodes are seen extending from the hole in the fiberglass. The wires entering the enclosure from the power supply and those leaving and going to the filter can be seen in the left of the photograph.

Micromanipulations are controlled by using the ACU and PZT actuators to get the whisker up against the bundle. However, macromanipulations to get the whisker in the vicinity of the bundle underneath the microscope are done with screws. There is one screw located on each of the stages. When it is screwed in, the screw moves the stage in one direction, and when it is unscrewed, the stage moves in the opposite direction. The total displacement created in one direction is the sum of the displacements due to the PZT actuator and the screw on any particular stage (Figure 4.9) [Burleigh Manual].

The pipette is secured to the micromanipulator by placing it in a small groove in an aluminum plate already attached to the face of the horizontal stage shown in Figure 4.8. It is secured by screwing another aluminum plate overtop of it to clamp it down (Figure 4.10).

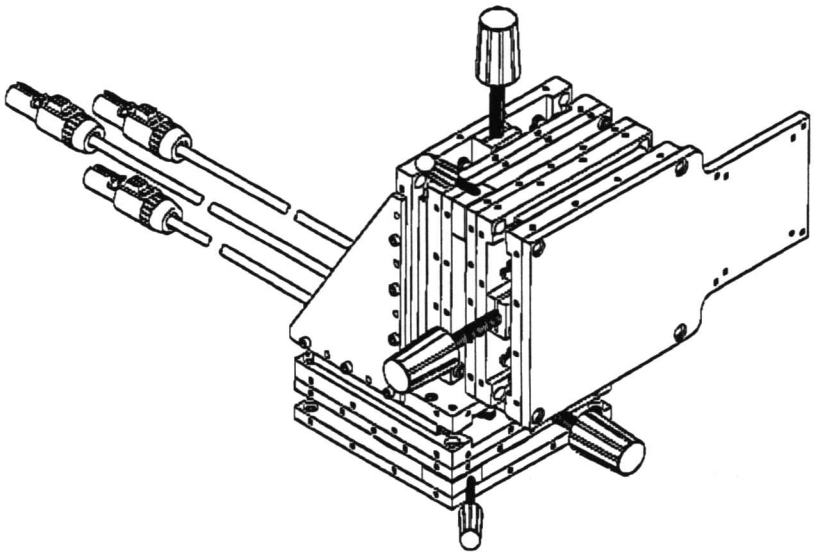

Figure 4.8 Micromanipulator (Burleigh manual).
The micromanipulator can move in three orthogonal directions. Each screw is responsible for macro-movements in these directions. The three extending cables lead to the Axis Control Unit which controls the piezoceramics that are responsible for the micro-movements. The small screws are necessary for tilt and rotation.

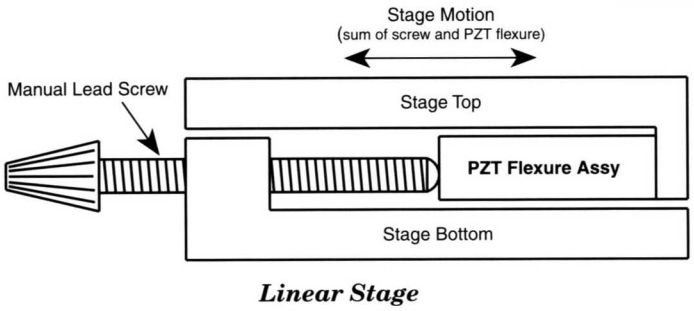

Figure 4.9 Displacement of PZT stage (Burleigh manual).
A stage of the micromanipulator can be displaced by a screw for macro-movements or by the PZT for micro-movements. The summation of both displacements equals the entire displacement of the stage.

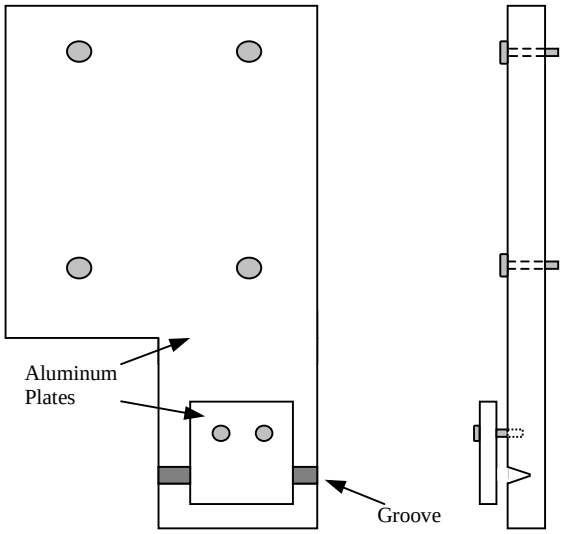

Figure 4.10 Pipette holder.
The large aluminum plate screws into the micromanipulator. A groove is cut into the plate for the pipette. Another aluminum plate is screwed into the larger plate to clamp down the pipette and prevent it from moving.

4.2.5 Whisker Fabrication

Whiskers are made from borosilicate glass rods pulled to a tip diameter of 1-2 μm. These whiskers are used to create a force on a hair bundle that will result in a displacement. The whiskers are intended to be slightly less stiff than the hair bundle so that the pipette displacement is greater than the bundle displacement due to contact (see Figure 4.11).

Initially, the borosilicate rods are placed in a micropipette puller (Stoelting Co. 51511) and a small piece of clay is placed on the end of the rod. The coils are heated until the rod begins to elongate due to the heat and force from the added weight and gravity. The rod is pulled until it is approximately 2-4 μm in diameter. Then it is placed in a microforge (Stoelting Co.) where it is again heated by a nickel-chromium filament and a weight is attached at the bottom. The rod is pulled to a final diameter of 1-2 μm. This step is extremely difficult because the whisker would often break prior to being pulled to just a few microns. A second rod is then taken and pulled using the micropipette puller to a 25 μm diameter. This pipette is shaped using the microforge (Figure 4.12) so it is suitable to be used with the slides that hold the specimen. The whisker is then bonded at a 90° angle to the micropipette using a light sensitive adhesive. This step is extremely meticulous. The slightest movements will create wind that will dramatically blow the whisker and prevent a 90° bond angle.

The stiffness of the displacement whisker can be calculated by attaching 30- to 100-μm diameter para-methyl-styrene spherical beads of known density (ρ = 1.030 g/cm^3; Bangs Laboratories, Inc) to the whisker end electrostatically, and measuring the resulting whisker deflection. The whisker and the attached beads are viewed through the microforge optics. The vertical displacement of the whisker due to the weight of the beads is measured with an eyepiece reticule. The corresponding weight of the bead is calculated from its diameter and density. This weight, along with the distance of the bead from the whisker edge and the whisker dimensions, are used to calculate the whisker's stiffness (explanation in Chapter 6). Each whisker is assessed with a minimum of 1-3 beads of varying sizes and the stiffness is calculated numerous times. The stiffness

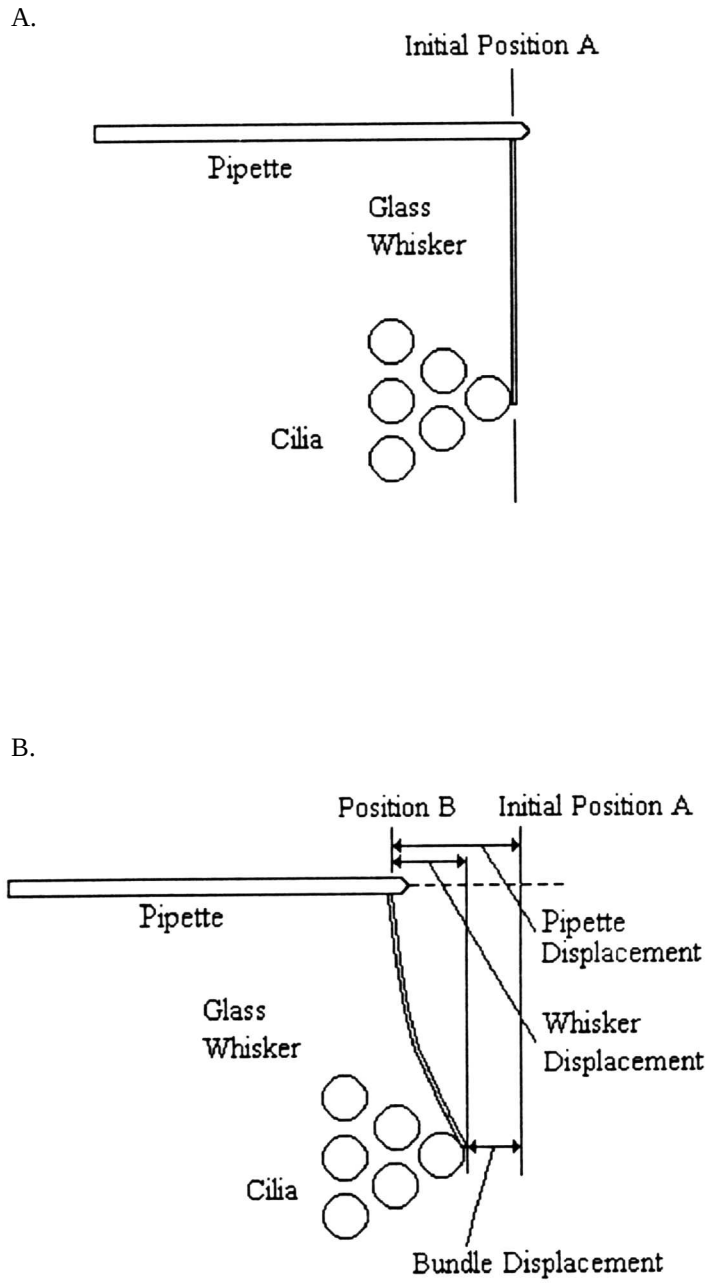

Figure 4.11 Mechanism for displacing the bundle with a whisker (Barrett, 1995).
A. The whisker is positioned up against the kinocilium of the bundle. **B.** As the bundle is displaced, the whisker, which is less stiff than the bundle, will bend and the pipette will move a further distance than the bundle/whisker point of contact.

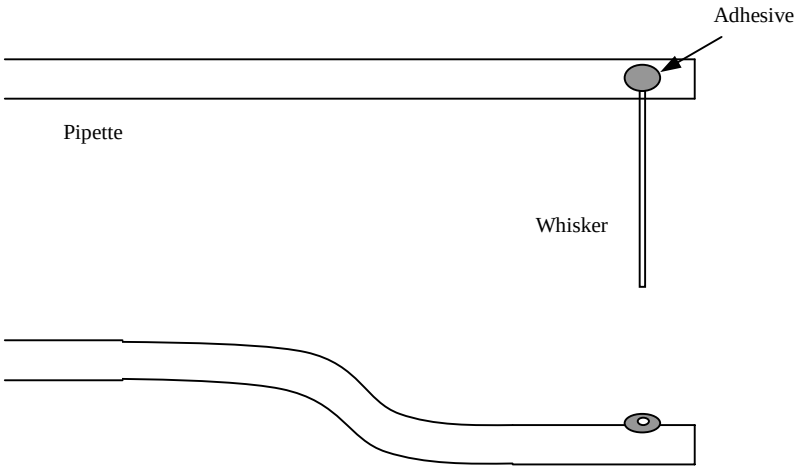

Figure 4.12 Pipette with attached whisker.

The glass pipette is bent so that the whisker will be able to take a horizontal approach to the hair cell bundle. This also enables the pipette to maneuver around the magnets holding the cover glass on which the utricle is placed (Figure 4.15).

values from these tests are averaged in order to calculate the mean stiffness for a particular whisker.

4.2.6 Optics and Imaging

The hair bundles were viewed with a light microscope equipped with DIC optics and an immersion lens (Figure 4.13). As mentioned in section 4.1, the microscope light source is a 12-volt, 100-Watt halogen bulb. The light begins its path by passing through a field diaphragm, which controls the amount of light that reaches the specimen. Then, the light encounters a polarizer with an east-west effect of polarization. Next, it travels through an aperture diaphragm which controls the depth of field and the contrast that will be seen. The condenser is located just above the aperture diaphragm and is the last object the light will pass through before encountering the specimen (Figure 4.14). After the light goes through the specimen, it will travel through the Wollaston prism which controls the shearing effects on the light for the DIC optics. The light next passes through a second polarizer oriented in a north-south direction. Finally, the light passes through an optivar for increased magnification and then onto the eyepieces, diode array, or video camera.

The specimen was placed on cover glass sandwiched between two magnets with holes cut in them (Figure 4.15). In order to make the slide for the specimen, two 50×75 mm magnets are cut from a magnetic canvas (Darice Magnets). A 10 mm diameter hole is cut in one magnet while a 25×35 mm rectangle is cut in the other. A ring of Vaseline is spread around one side of the magnet with the hole. Then, this magnet as well as the other magnet are used to sandwich a $35 \times 50 \times 1$ mm sheet of cover glass (Fisherbrand). The hole is cut in the top magnet for the specimen and Ringers solution to be placed in and the ring of Vaseline is to create a seal in order to prevent the fluid from leaking. The rectangular hole in the bottom is cut to allow light to pass through and so that the distance from the condenser to the specimen can be decreased. A thin cover glass is used instead of a normal glass slide since DIC optics do not work well if the light must travel through a thick surface before reaching the specimen. The tissue is pinned down with insect pins that have been glued to small pieces of aluminum (Figure 4.15). The aluminum will be attracted to the magnet, and the pin head will effectively hold down the tissue and prevent any movement.

The image of the specimen travels to the eyepieces in the scope as well as to the beam splitter sitting atop the microscope. The beam splitter sends the image to both the photodiodes and a video camera (Dage-MTI DC200). The camera feeds the signal to a videocassette recorder (Sony SVO-2100), through a video ruler (Mercer Imagen XR2001) and finally to a color video monitor (Sony Trinitron PVM-14M2MDU). The VCR is available for taping any test being performed or to record the hair bundles seen on the specimen. The video ruler is needed to measure the exact size of the glass whisker, dimensions of the hair bundle, and is an additional method for calibrating the PMT and measuring the displacement of the bundle when a force is applied by the whisker.

The entire microscope setup was connected to a vibration isolation table (Technical Manufacturing Corporation). This was done so that the specimen could be viewed isolated from and testing could be done without the effects of floor born noise or other vibrations from the surrounding environment. The specimen itself was placed underneath the microscope on an X-Y stage (Burleigh) seen in Figure 4.16. This was done so that we had the option of moving the specimen without having to move the scope.

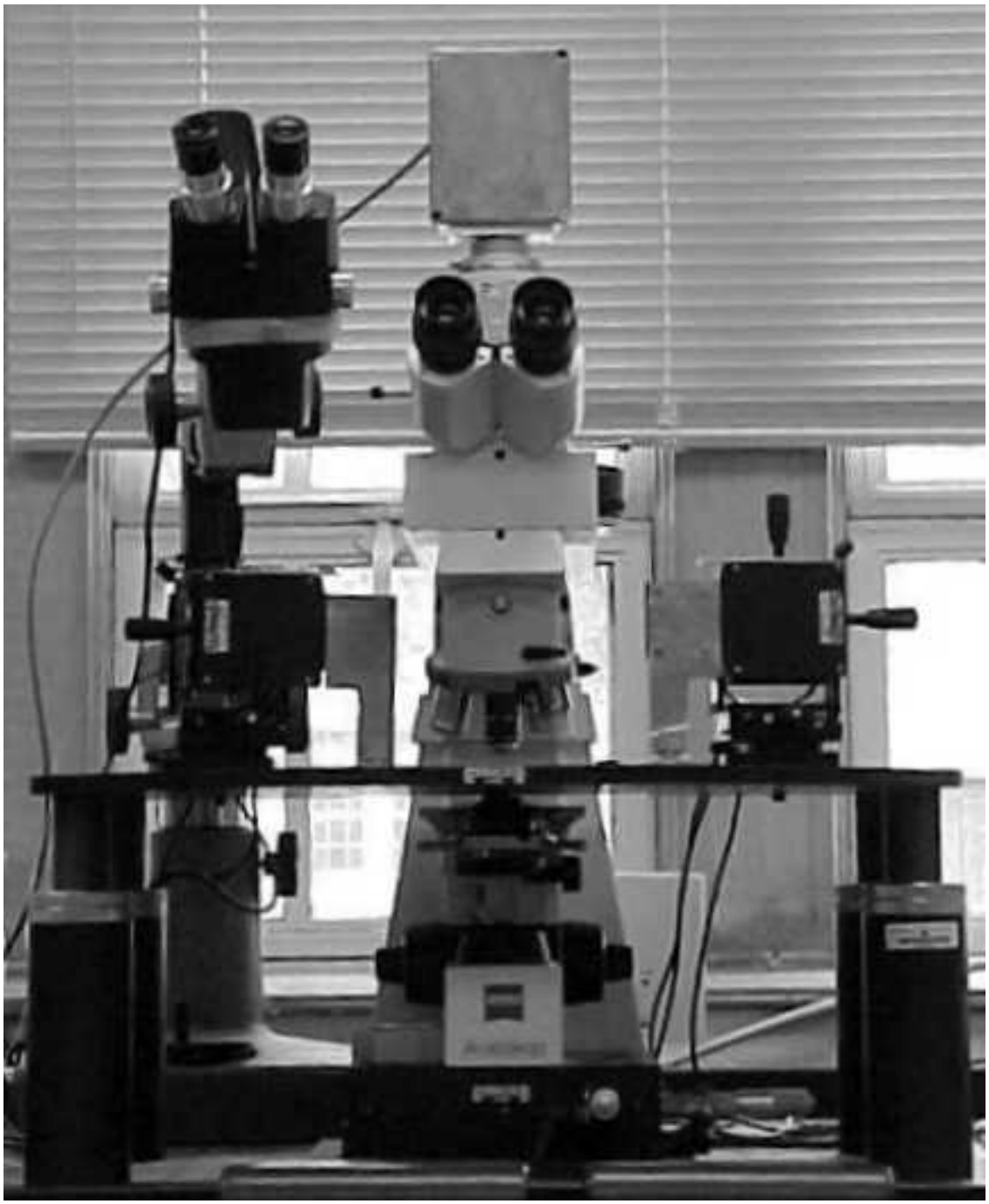

Figure 4.13 Zeiss Axioplan microscope with DIC optics.
The full microscope can be seen in this picture. There is a micromanipulator on either side. The second scope on the left is a light microscope used for positioning the EFPI sensor.

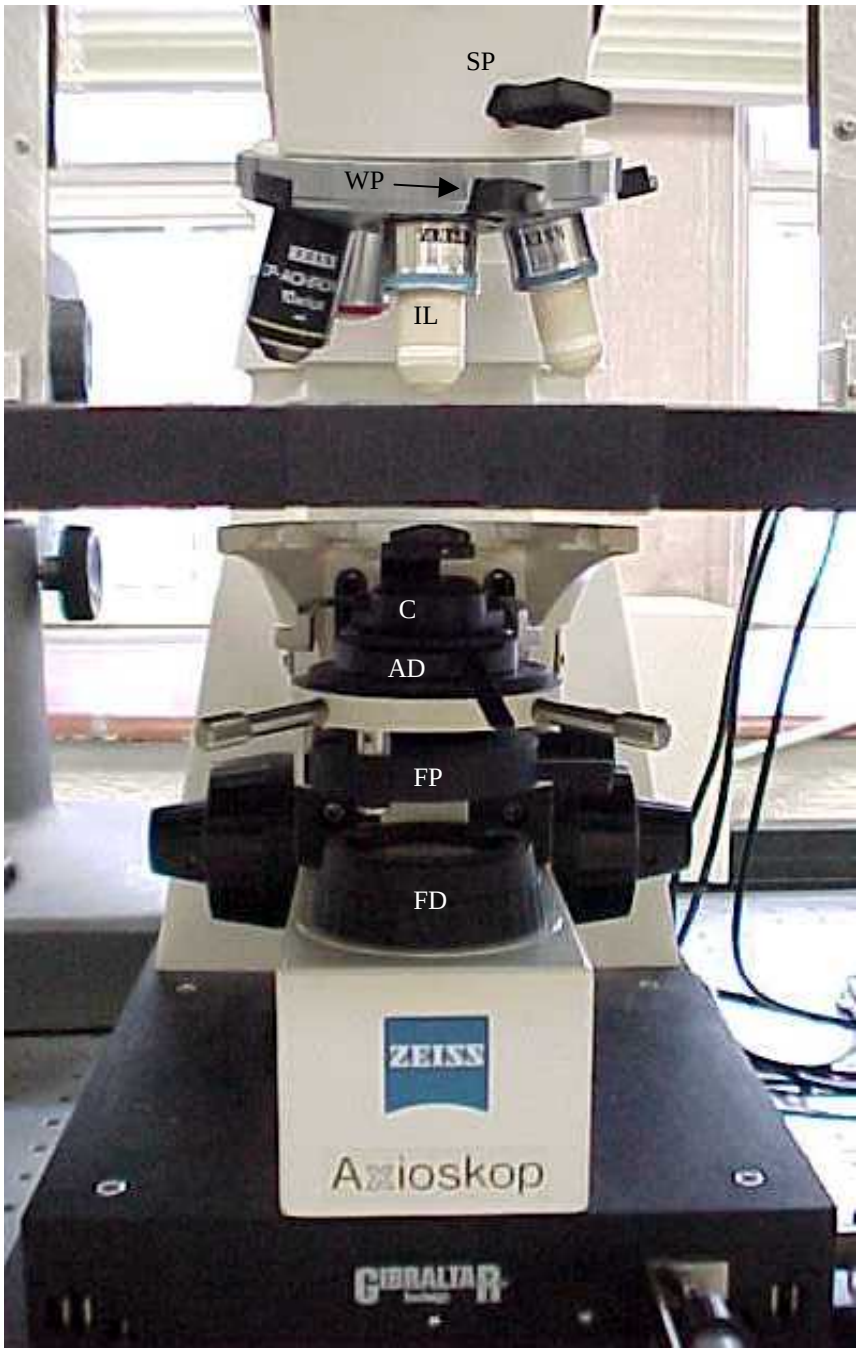

Figure 4.14 Zeiss Axioplan microscope with DIC optics.
This picture displays components of the DIC optics. The light comes from the halogen bulb and travels through the field diaphragm (FD), next through the first polarizer (FP), on to the aperture Diaphragm (AD) and finally through the condenser (C). Above where the specimen will be placed is the immersion lense (IL), the Wollaston prism (WP) and the second polarizer (SP).

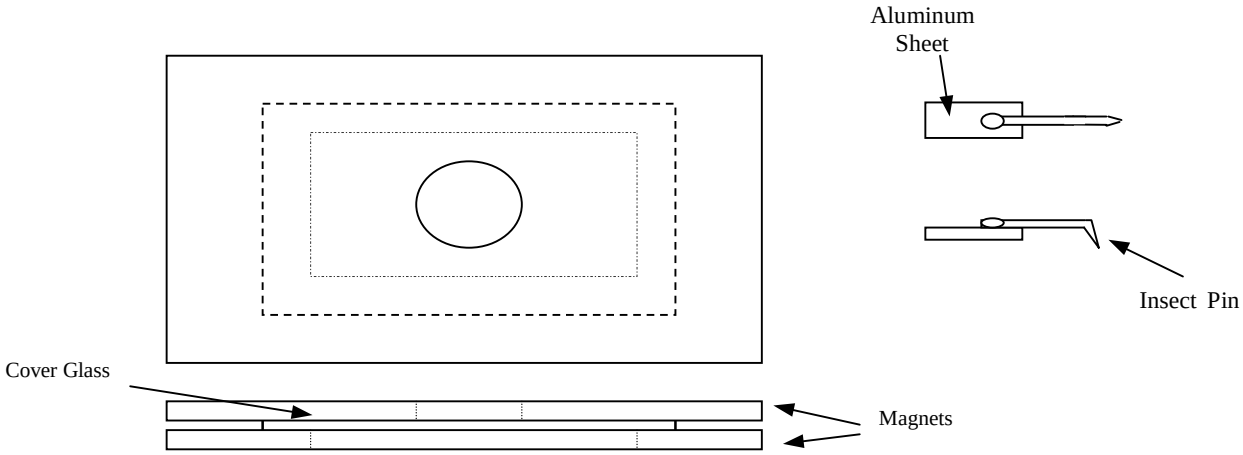

Figure 4.15 Microscope slide designed to hold specimen preps.
Two magnets sandwich a 35×50 piece of cover glass. A hole is cut in the top for the specimen and a square is cut in the bottom so that the condenser can be raised and positioned close to the specimen. This enables optimal performance of the DIC optics. The pin to the right is used to hold the specimen in place. The aluminum sheet will be attracted to the magnet while the insect pin will hold down the specimen.

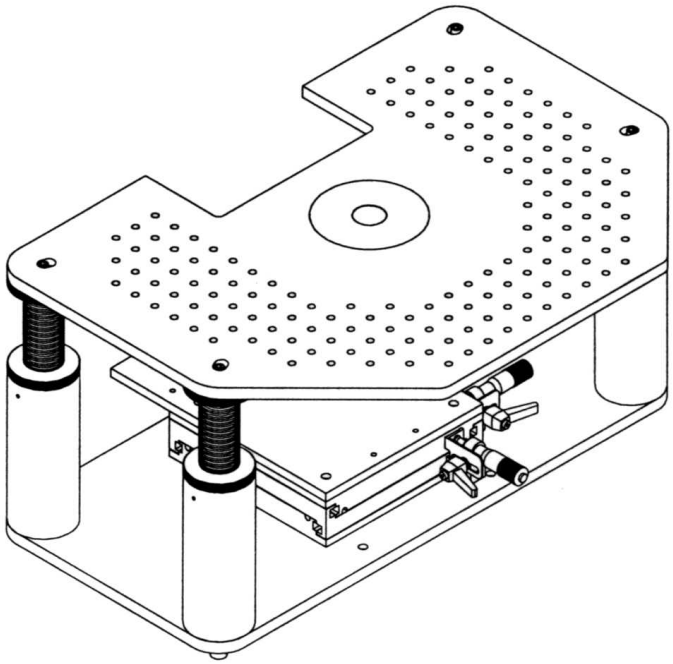

Figure 4.16 X-Y stage.
The specimen is placed on the slide and then positioned on the X-Y table underneath the microscope. The table is used to further adjust the position of the specimen by turning knobs which move the table in the x and y directions.

5.0 EXPERIMENTAL PROCEDURES

Measuring the stiffness of a hair bundle is extremely difficult and takes a great deal of time. There are numerous steps involved in performing a successful test ranging from the dissection of the utricle from the inner ear to measuring the displacement of a hair bundle due to an applied force. The steps taken to obtain values for hair bundle stiffness will be explained in this chapter.

5.1 TISSUE PREPARATION

The examined hair cells for this experimentation were located in the utricle of the *Pseudemys (Trachemys) scripta*, known as the red-eared slider turtle. The tissue tests will be conducted *in situ*, meaning that the hair cell being tested retains its normal position in the sensory epithelium. Therefore, it is important that the tissue be prepared correctly, and careful steps must be taken to anesthetize the subject, remove the labyrinth of the inner ear, and separate the utricle. These steps will be discussed in detail in the following sub-sections.

5.1.1 Anesthetization

Prior to removing the labyrinth, the turtle must be anesthetized using methods approved by the Virginia Tech Animal Care Committee. The chemical used is sodium pentobarbital (provided by the Virginia Tech Veterinary School), a general surgical anesthesia used for animals. The prescribed dosage to uthanize the animal is 50 milligram of the drug per kilogram of animal body weight. The drug's concentration was 65 mg of sodium pentobarbital per ml of solution. The turtle was weighed on a balance. This weight was multiplied by the prescribed uthanization dosage and then divided by the chemical weight to get the required dosage for a particular turtle, as shown in equation [5.1].

$$\text{Uthaniziation Dosage [ml]} = \frac{\text{Turtle Weight [kg]} \times \text{Required Dosage [mg/kg]}}{\text{Drug Concentration [mg/ml]}} \qquad [5.1]$$

On average, the turtle weighed approximately 0.2 kg and therefore would require a dosage of 0.154 ml of sodium pentobarbital for uthanization.

$$\text{Uthaniziation Dosage [ml]} = \frac{0.200\ \text{kg} \times 50\ \text{mg/kg}}{65\ \text{mg/ml}} = 0.154\ \text{ml}$$

The calculated dosage was injected either intramuscularly into the hind leg or into the peritoneal cavity. Within 20 minutes, the chemical took effect and the turtle became limp and unresponsive to stimulus.

5.1.2 Extraction of the Labyrinth

The first step in dissection is to separate the head from the remainder of the carcass by decapitating the turtle. The ventral side of the head is cleaned by removing the jawbone, esophagus, tongue and other connective tissue, thus exposing the skull bones (Figure 5.1). The dorsal skull bones of the turtle (Figure 5.2) are exposed by removing the skin, muscle and other connective tissue covering them. The head is then cut into two halves, with each half being placed in a petri dish filled with lactated ringer's solution.

Prior to extracting the labyrinth, it is important to notice its location and orientation within the head. This is depicted in Figure 5.3. In order to dissect out the labyrinth, the squamosal, quadrate, paroccipital and pre-optic bones are all removed. This will leave a small ridge made up of the parietal (rostral) and supraoccipital (caudal) bones, which provide a thin cover for the horizontal canal. Through the thin bone, the canal can be seen as a dark image running horizontally. Blunted forceps can now be used to pick away the bone in order to expose the horizontal canal. The anterior canal is exposed by carefully breaking off pieces of the parietal bone. The posterior canal lies under the supraoccipital bone and can be exposed by removing pieces of this bone. The majority of the bone should be removed from around the canals so the tissue will be disturbed as little as possible when removed [Barrett, 1995].

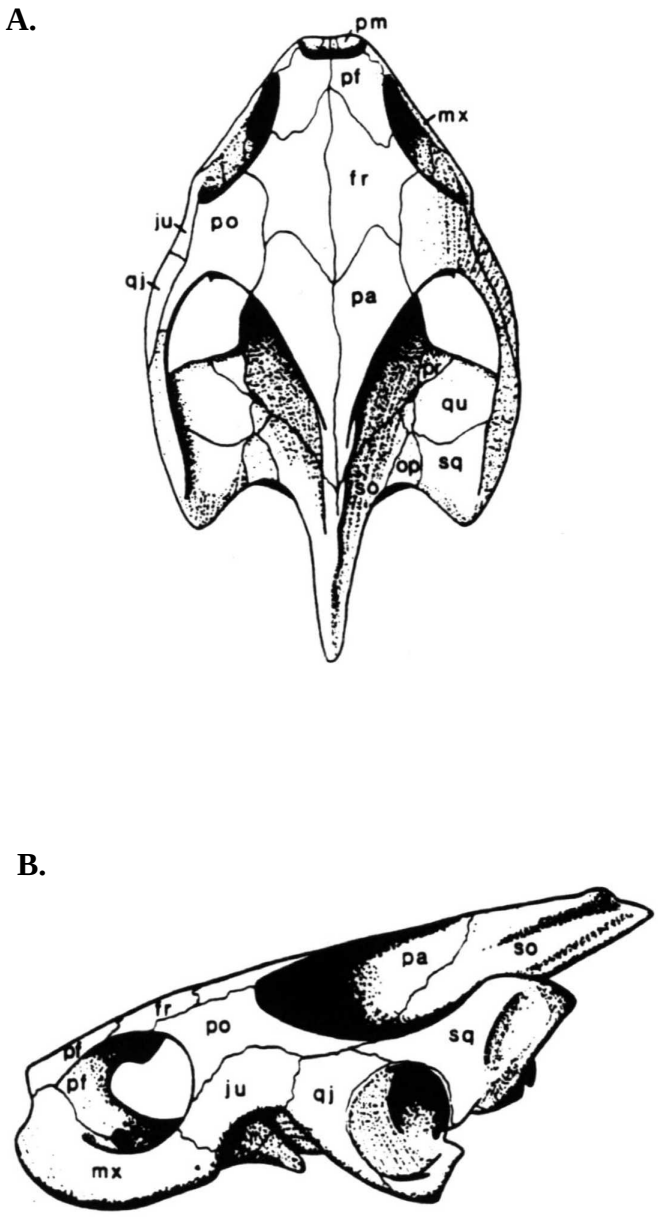

Figure 5.1 Skull bones of a *Pseudemys (Trachemys) scripta* (Gibbons, 1990).
A. A diagram of the dorsal skull bones. Many are removed to aid in the dissection of the vestibular labyrinth. **B.** A diagram of the lateral skull bones.
fr, frontal; **ju**, jugal; **mx**, maxillary; **op**, paroccipital; **pa**, parietal; **pf**, prefrontal; **pm**, premaxillary; **po**, postorbital; **pr**, pre-optic; **qj**, quadratojugal; **qu**, quadrate; **so**, supraoccipital; **sq**, squamosal

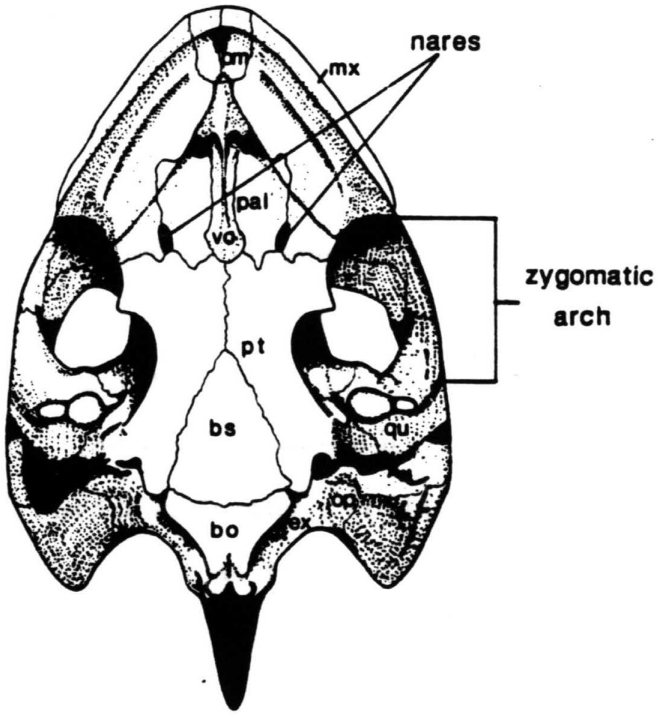

Figure 5.2 Ventral skull bones of the Pseudemys (Trachemys) scripta (Gibbons, 1990).
bo, basioccipital; **bs**, basisphenoid; **mx**, maxillary; **op**, paroccipital; **pal**, palatine; **pm**, premaxillary; **pt**, pterygoid; **qu**, quadrate; **vo**, vomer

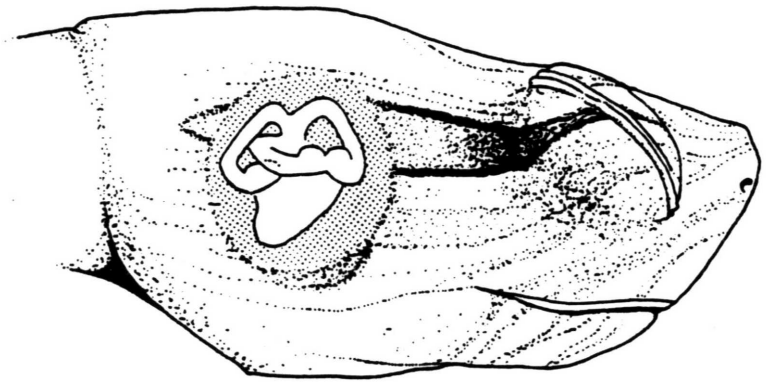

Figure 5.3 Location of the vestibular system (Brichta and Peterson, 1994).
This drawing shows the location and orientation of the vestibular system within the head of the red-eared slider turtle.

The next step is to view the head ventrally and remove the basioccipital, basisphenoid and the claudal portion of the pterygoid bone. This allows for access to the eighth cranial nerve (vestibulocochlear nerve) and the hindbrain. The labyrinth is separated from the CNS by a thin piece of cartilage through which the eighth cranial nerve passes. This cartilage is removed to expose the ventral-medial part of the labyrinth. The nerve is cut in order to free the labyrinth from the CNS. Once the bone that lies ventral and medial to the horizontal canal is removed, connective tissue holding the medial portions of the anterior and posterior canals should be the only remaining points of connection. The tissue should easily pull away from the bone, but if it does not, then it must be cut [Barrett, 1995]. The extraction of the labyrinth is now complete.

The dissections are done using a stereomicroscope (Zeiss Stemi 2000C) as well as a transmitted light base (Diagnostic Instruments TSB 3.1) and overhead illumination (Fostec 150 W). The extraction of one labyrinth takes approximately 30 – 40 minutes to complete once the turtle is decapitated. Tissue preservation is extremely important and it is estimated that the tissue is only viable for up to 7-8 hours after the animal's death. The extraction is done while the head is submerged in lactated Ringer's solution (Virginia Tech Veterinary School).

5.2 DISSECTION AND ORIENTATION OF THE UTRICLE

This section will discuss the separation of the utricle from the vestibular system and the orientation in which the tissue must be mounted on a slide in order to expose the hair bundles. These two steps in the procedure are extremely difficult and are critical for obtaining good results.

5.2.1 Dissection of the Utricle

After the labyrinth is extracted from the skull, it is placed in a petri dish that has a layer of sylgard on the bottom and is already filled with ringer's solution. The labyrinth is secured into place, with the nerve facing up, by using dissecting pins that hold the tissue to the sylgard. Small scissors are used to cut the majority of the horizontal and anterior canals from the saccule and utricle. An incision is then made to remove the saccule, which leaves the utricle along with the portion of the vestibulocochlear nerve that innervates the utricle and small portions of the two canals. The nerve must be

removed from the utricle by peeling it back using scissors, or by gently using a diamond tipped scalpel to cut it away. This must be done extremely carefully, as the sensory epithelium is very delicate and easily damaged.

The tissue is re-pinned so that the dorsal side is now facing up. An incision is made from the anterior canal to the horizontal canal along the dorsal surface. In order to expose the utricle, a cut is then made from the point where the anterior and horizontal canals connect to the back of the utricle (Figure 5.4). The cut tissue is peeled back and pinned, exposing the otolith layer that covers the sensory epithelium. The utricle resembles a scallop shell, with the abneural side facing the two ampullae. There is a shelf of tissue that covers a small portion of this side. This shelf is removed by making small incisions along its length and peeling it back. This will expose the striolar region, where the hair bundles are most dense. The otolith layer must be pulled out of the utricle very delicately as not to damage the hair cells and their ciliary bundles.

5.2.2 Mounting the Utricle

Once the utricle has been exposed, it is transferred onto a slide made from two magnets sandwiching a sheet of cover glass (Figure 4.15). The tissue is held in place with insect pins that have been glued to small pieces of aluminum (Figure 4.15). While on the slide and during tests, the utricle is covered in lactated ringer's solution.The pin will effectively hold down the tissue and prevent any drift of the tissue while under the microscope. Any tissue movement during testing would seriously alter the light detected by the photodiodes and thus taint the results. Prior to using pins as a method for securing the tissue, we attempted to glue the tissue to the glass cover using an epoxy as well as a light sensitive glue. Neither adhesive worked as they both coated the tissue and the hair cells, destroying the specimen. Other researchers have tried cyanoacrylate and tissue adhesives without much success [Barrett, 1995].

Looking through the stereoscope, the utricle was gently folded in half along a transect (Figure 5.5), with the ciliary bundles being on the outer surface. This will allow us to scan along one transect of the utricle for hair cells. We will also be able to compare the different types of hair cells found in the three regions, observe the location in which

the bundles experience a change in the direction of polarity, and estimate the ranges of the rampa, cotillus, and striolar regions. This is important so that we know what type of

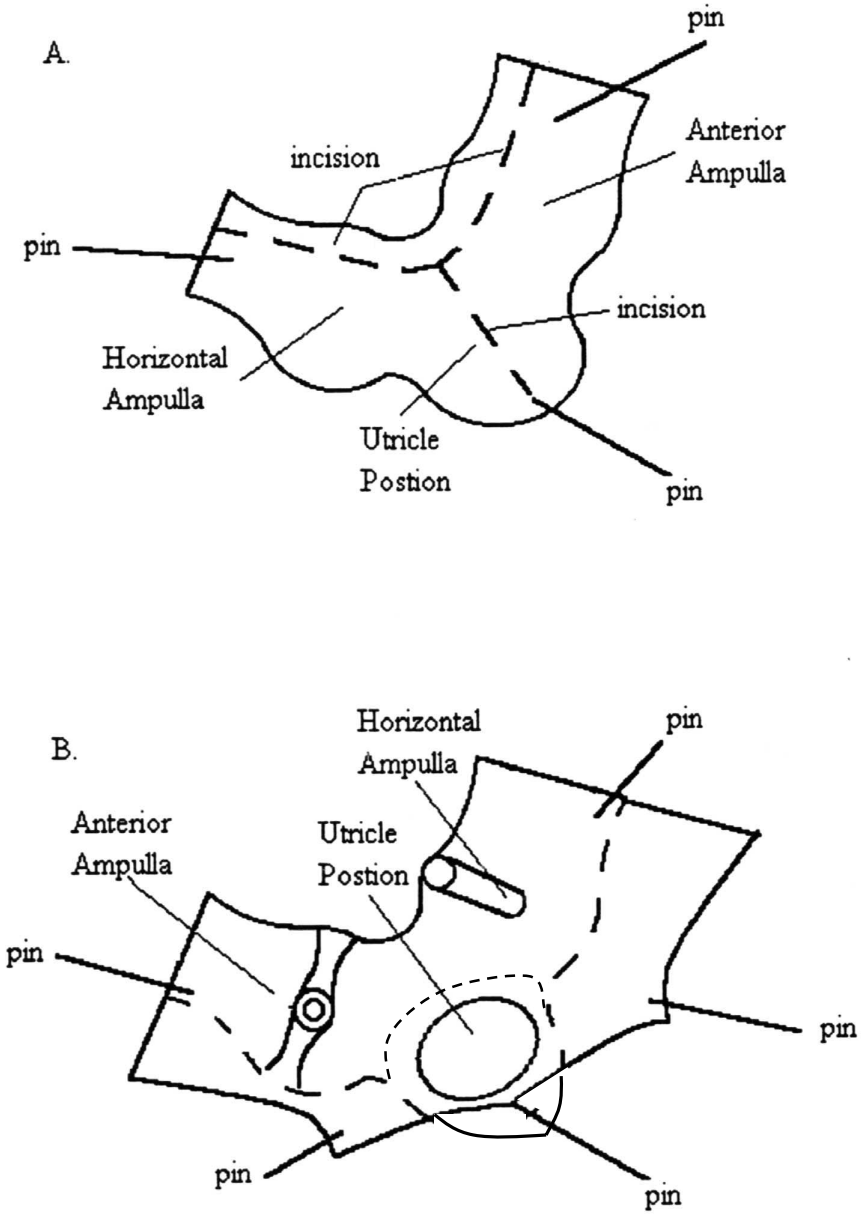

Figure 5.4 Exposed utricle (adapted from Barett, 1995).
The utricle, along with portions of the horizontal and anterior ampullae, is cut from the rest of the labyrinth. Incisions are made and tissue is pinned back to expose the utricle. The shelf of tissue covering the utricle will then be removed. Finally, the utricle will be separated from the surrounding tissue.

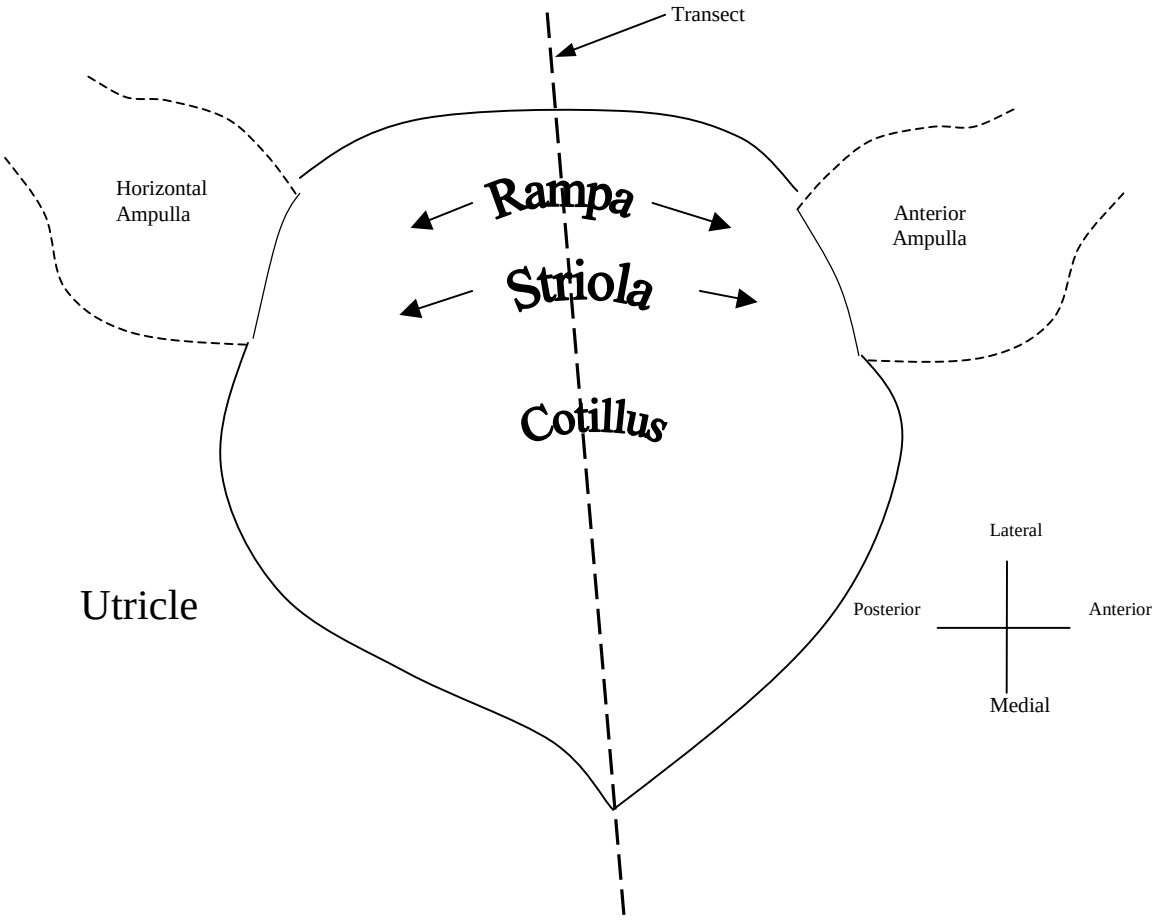

Figure 5.5 Utricle Transect.
The shape of the utricle resembles a scallop shell. Once the utricle is isolated and the outlying tissue removed, then it is placed flat on the cover glass. It is folded back and pinned along a transect that extends from the point of the utricle where the nerve enters and the midpoint between where the horizontal and anterior ampullae previously resided. This is so the profile of the hair cell bundles will project from the tissue surface.

hair cell we are examining, the dimensions of the hair cell, and where it is located in the utricle. The tissue is folded in this manner because it is much easier to conduct a test on and measure the deflection of an isolated hair cell bundle when viewed in profile.

5.3 PRE-TEST PREPARATION

Prior to actually displacing a hair bundle with the whisker and measuring the displacement, a number of steps must be taken to focus the microscope, find a hair bundle, align and calibrate the whisker, and prepare the EFPI and photodiodes.

5.3.1 Focusing the DIC Optics

Once the folded utricle is placed under the microscope, the microscope and the accompanying DIC optics must be correctly focused to achieve maximum contrast and resolution of the image. The first step is to select the 10× objective (N.A. 0.25) and turn the optivar, used for additional magnification, to 1× and focus on the utricle. At this magnification hair cells will not be visible, but the utricle itself can easily be put in focus. Now, open the condenser diaphragm completely and close the field diaphragm as much as possible. This will cause the visible field as seen through the eyepiece to become a small, round area. Adjust the condenser height until the edges of the field diaphragm become sharp. Center the image of the field diaphragm using the setscrews and then open the diaphragm until the edges of the visible field can still barely be seen. Finally, close the condenser until it is only open approximately two-thirds the value of the numerical aperture of the objective currently being used. In order to see hair cells, a higher magnification immersion objective must be used and the above steps must be repeated with each magnification increase.

5.3.2 Choosing a Test Specimen

The hair bundles can be seen well with a 40× objective (N.A. 0.75, immersion lens), the optivar set at 1.6× and with 10× eyepieces. The utricle is viewed along the transect where the fold was made. The hair bundles will vary in height and orientation based on where they lie with respect to the striolar region. We will concentrate on the hair bundles found in the striolar region and the cotillus because they are much more prevalent than bundles located in the rampa. Once a suitable hair cell is chosen, the

dimensions of the bundle are measured using the Imagen XR 2001 and the image fed to the monitor from the video camera.

5.3.3 Calibrating the PMT

Once a suitable hair bundle is located, it is positioned in the center of the field of view using the X-Y microscope stage. Then, a pipette, with whisker attached, is placed in the micromanipulator and positioned so that the whisker is on the same plane as the kinocilium and can make contact with it when moved horizontally. However, the test can not yet be performed. The photoelectronic motion transducer (PMT) must first be calibrated so that the voltage-displacement relationship of the whisker and diodes is known. This must be done prior to each test since slight changes in light intensity, whisker thickness, focus, and numerous other factors cause a significant change in the photodiode's response.

In order to conduct the calibration, the whisker is pulled back slightly from the bundle so that as it is moved across the field of the diodes, it will not contact the hair bundles (Figure 5.6). With the whisker in place, the Fabry-Perot interferometer (EFPI) is turned on and the reflecting fiber is adjusted until a good spectrum plot is achieved with a gap distance around 40 microns. The dual power supply for the diodes and circuit is turned on as well as the multimeter that displays the output voltage from the diodes. Using the micromanipulator, the whisker is moved across the field of the diodes as the gap distance from the EFPI and the corresponding photodiode output voltages are recorded. The whisker is moved until it crosses through the region where the two diodes are separated by the small gap (Figure 4.4). This region produces a linear relationship between output voltage of the PMT and displacement of the whisker (change in gap distance) as the whisker blocks light on one plate and then the other (see Chapter 6). This is the region in which the testing will be done since it is very sensitive to movement and shifts in light intensity and has a large slope on a voltage versus displacement plot (Chapter 6). When the first calibration is completed, the whisker is brought back to its starting position and the calibration is repeated. The Imagen XR 2001 can also be used to measure the whisker movements and be compared with the EFPI output of gap distance.

A plot is made that shows the photodiode output voltage versus the gap distance of the EFPI. A linear region will be visible which is physically indicative of the whisker moving off of one photodiode plate and onto the other. The slope of this region will give the voltage-displacement relationship that is representative of the amount of voltage the PMT will output for a certain physical displacement of the whisker. This value is important because it will be used to calculate how far the kinocilium has moved due to the applied force of the whisker. Examples will be presented in Chapter 7.

Good test results can only be achieved after an accurate calibration of the system has been performed. The calibrations are meticulous and time consuming, with correct whisker setup being key. The whisker must be oriented so that it is perfectly horizontal. This allows the entire whisker to be in focus at the same time. If any part of the whisker is blurred, then this will alter the shadows it casts on the diodes. The whisker must also be aligned perfectly parallel to and move in a direction perpendicular with the borders of the diodes. If the whisker crosses the borders at an angle, then the PMT will not provide a correct output voltage. Other factors, such as light intensity must remain constant for calibrations and tests as they too can effect results. Finally, the background of what is being focused on must remain unchanged. If things surrounding the whisker are being moved around, such as dust on a glass slide, then the results will be skewed.

5.4 TISSUE TESTS

5.4.1 Test Procedure

When the PMT calibrating procedure is completed, the whisker is moved back inline with the hair cell to its previous position next to the bundle (Figure 5.6). The tip of the whisker is positioned up against the end of the kinocilium. The current EFPI gap distance and the photodiode output voltage are recorded at this point. The whisker is then displaced causing a force on the bundle. The whisker, being less stiff than the bundle, will begin to bend from the point where it is bonded to the pipette (Figure 5.7). When the applied force becomes large enough, the bundle itself will begin to displace. After the bundle has moved a small distance, the whisker is stopped, and both the gap distance and the output voltage are again recorded. The change in gap distance corresponds to the amount the pipette is moved by the micromanipulator. The change in output voltage

from the diode is used along with the relationship found from the calibration to measure how far the hair bundle has moved. These two values along with the known whisker stiffness are used to find the bundle stiffness as explained below. The whisker is then backed up until it is no longer in contact with the kinocilium. Then, it is again positioned so that it meets the tip of the kinocilium and the above test steps are repeated numerous times. The resulting stiffness values are averaged to get a stiffness for that particular ciliary bundle.

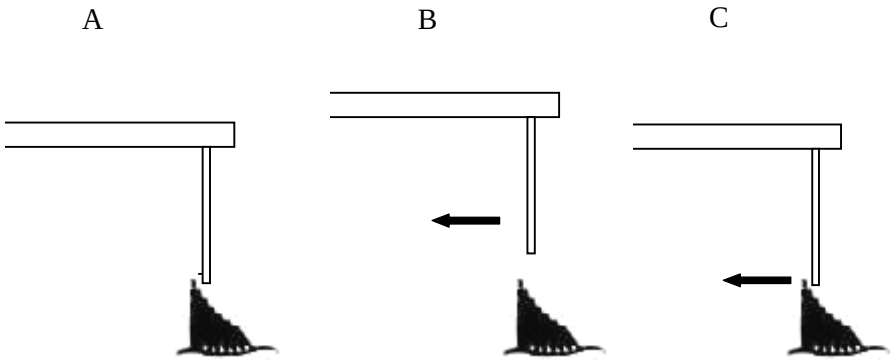

Figure 5.6 Whisker position for calibrating and testing.
A. The whisker is initially placed on a horizontal plane with the hair cell and moved to the tip of the kinocilium. **B.** For calibrating the photodiodes, the whisker is moved slightly back from the tip of the bundle. It is then run across the field of the photodiodes while the position and voltage outputs are recorded. **C.** Once the calibration is complete and the voltage-displacement relationship for the diodes found, the whisker is moved back to its previous position in line with the bundle. In order to conduct the tests, the whisker is positioned at the tip of the bundle, moved so it displaces the bundle a short distance, and then returned back to the original position. This last step is repeated for each test.

This process is also time consuming and tedious. It requires delicate movements with the whisker so the hair cells are not disrupted and displaced too much. Patience is necessary when trying to use a 2 μm diameter whisker to displace a bundle that has a kinocilium just a few hundred nanometers in diameter. Also, it must be recognized when outputs from the PMT are stable enough to be recorded, or when there is too much tissue movement and the measurements must be performed again.

5.4.2 Calculating the Bundle Stiffness

A ciliary bundle's response to mechanical stiffness is determined by its stiffness, k, which is defined as

$$k = F/\delta \qquad [5.2]$$

where F is the force applied to the bundle and δ is the resulting deflection. In this case, the mechanical stimulus is the force applied by the whisker. Figure 5.7 shows the technique used to displace the bundles. The whisker is glued to a pipette which is attached to the micromanipulator. The pipette is positioned up against the ciliary bundle where an initial EFPI gap distance and PMT output voltage are recorded. The pipette is then displaced a certain distance, Δx_P, measured by the EFPI system. As the pipette is moved, it will move the whisker which comes into contact with the bundle. The whisker, being less stiff than the bundle, begins to bend while applying a force to the bundle. As the pipette continues to be moved, the force on the bundle grows until it is large enough to displace it. After a small amount of bundle displacement, the pipette movement is stopped and a second EFPI gap distance and PMT output voltage are recorded. The difference in the gap distance values is the amount the pipette has been displaced, or Δx_P. The change in the PMT output voltage due to the bundle movement, along with the previously found calibration information, can be used to calculate the bundle displacement, or Δx_B.

$$\Delta x_B\,[\mu m] = \frac{\text{change in PMT output voltage}\,[V]}{\text{calibration factor}\,[V/\mu m]} \qquad [5.3]$$

The bundle and pipette displacements can be used to find the amount of the whisker deflection, Δx_W,

$$\Delta x_W = \Delta x_P - \Delta x_B. \qquad [5.4]$$

Using the relationship between force, displacement, and stiffness from [5.2] and the fact that the contact forces, for these steady state experiments, on the whisker due to the

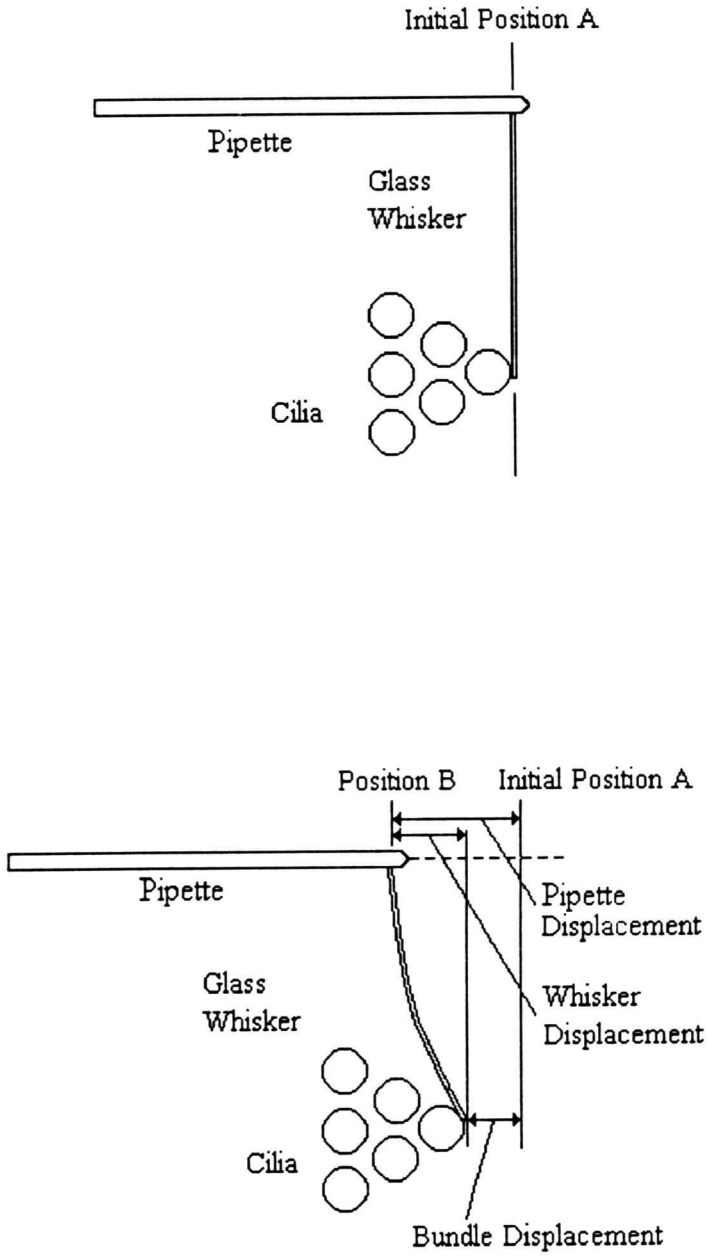

Figure 5.7 Whisker and bundle deflection during testing (Barrett, 1995).
The top drawing shows the initial position of the whisker placed up against the kinocilium of the ciliary bundle. The bottom picture shows the result of the whisker being displaced. The pipette is displaced which causes the whisker to create a force on the bundle. This leads to a bending of the whisker and a deflection of the bundle. These displacements can be used in the calculation of the stiffness of the ciliary bundle. Note that this picture shows the bundles in a top view. This is for illustrative purposes only, since we work with bundles in a profile view.

bundle (F_B) and on the bundle due to the whisker (F_W) are equal and opposite (Barrett, *et al*, 1999), we arrive at

$$F_B = F_W \qquad [5.5]$$

which can be rewritten as

$$k_B \Delta x_B = k_W \Delta x_W \qquad [5.6]$$

where k_B and k_W are the stiffness of the bundle and whisker, respectively. Solving this equation for Δx_W, substituting it into [5.4], and then solving for the bundle stiffness gives

$$k_B = k_W \left(\frac{\Delta x_P}{\Delta x_B} - 1 \right). \qquad [5.7]$$

Since the whisker stiffness is already known (see Chapter 6) and Δx_P and Δx_B are measured during tests, then the bundle stiffness can be found.

6.0 SYSTEM TESTS AND CALIBRATIONS

The testing procedure explained in Chapter 5 requires the use of many different pieces of equipment and materials. Prior to using any of this equipment in an actual test to measure the stiffness of a hair bundle, we must ensure that it is in working order and accurate. Before testing, we need to accurately calculate the stiffness of the whisker, verify the photodiodes linear response to light detection, map the photodiode boundaries onto the monitor, and use all of the aforementioned components to test the entire PMT system. Otherwise, there will be a large margin for error and any potential problems could be due to a number of sources. However, verifying that each piece of equipment is in good working order provides a high confidence level in our final test results.

6.1 WHISKER CALIBRATION

The glass whiskers are manufactured using a micro-pipette puller and a microforge as discussed in section 4.2.5. These whiskers are primarily necessary to apply the force to the hair bundle in order to displace it, but will also be needed to calibrate the system and perform tests on imitation hair bundles (section 6.4). As was mentioned in previous sections, the three values needed in order to be able to calculate the stiffness of a bundle are the displacement of the bundle, the displacement of the base of the whisker/pipette, and the stiffness of the whisker. Therefore, it is necessary to calculate the stiffness of the fabricated whiskers.

In order to calculate the stiffness of the whisker, the pipette to which it is bonded is placed vertically in the microforge. This will put the whisker in a horizontal plane (Figure 6.1). The end of the whisker will be lowered onto a pile of styrene beads. These beads will attach themselves to the whisker electrostatically. As a result, the whisker will bend under the added weight of the beads (Figure 6.1). The stiffness of the whisker can be calculated by modeling it as a beam with applied point loads. We will use the equation for calculating the deflection of a beam due to a force applied at the end. However, since not all beads will attach to the tip of the whisker, we include a correction

factor for forces not applied at the end of the beam [Beer and Johnston, 1992] and the equation becomes,

$$\delta = \frac{W_i}{6EI}\left(2l^3 - 3l^2 a_i + a_i^{\,3}\right) \qquad [6.1]$$

where δ is the total beam deflection, W is the weight of the bead, l is the length of the whisker, a is the distance of the bead from the tip of the whisker, E is the elastic modulus and I is the moment of inertia. A free-body diagram of the whisker with an applied load from a bead is shown in Figure 6.2. The principal of superposition allows the equation to be used for one or more beads attached at one time. Knowing the fact that

$$\mathrm{k} = F/\delta = 6EI/2l^3 = 3EI/l^3, \qquad [6.2]$$

where F and δ are the force and deflection that occur at the end of the beam, solving [6.1] for $3EI/l_i^3$, and then substituting [6.2] into [6.3] provides

$$k = \frac{W_i\left(1 - \frac{3}{2}\frac{a_i}{l_i} + \frac{1}{2}\frac{a_i^3}{l_i^3}\right)}{\delta}. \qquad [6.3]$$

This is the equation used to calculate the stiffness of a whisker when i beads are attached. The weight of each bead is determined from

$$W = mg \qquad [6.4]$$

$$W = \rho V g \qquad [6.5]$$

$$W = \frac{4}{3}\pi r^3 \rho g \qquad [6.6]$$

where m is the mass, V is the volume, ρ is the density and r is the radius of a sphere. The beads have a known density of 1.030 g/cm^3. The quantity g is the acceleration due to gravity. When [6.6] is substituted into [6.3], the final result for the equation used to determine the stiffness of the whisker is

$$k = \frac{\frac{4}{3}\pi r_i^3 \rho g\left(1 - \frac{3}{2}\frac{a_i}{l_i} + \frac{1}{2}\frac{a_i^3}{l_i^3}\right)}{\delta}. \qquad [6.7]$$

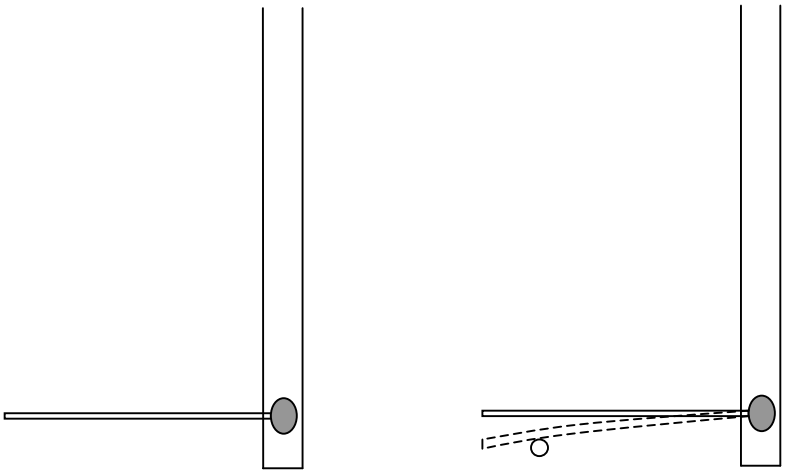

Figure 6.1 Whisker deflection.
The drawings show that when a bead attaches to the whisker electrostatically, the whisker will deflect a certain distance due to the added weight.

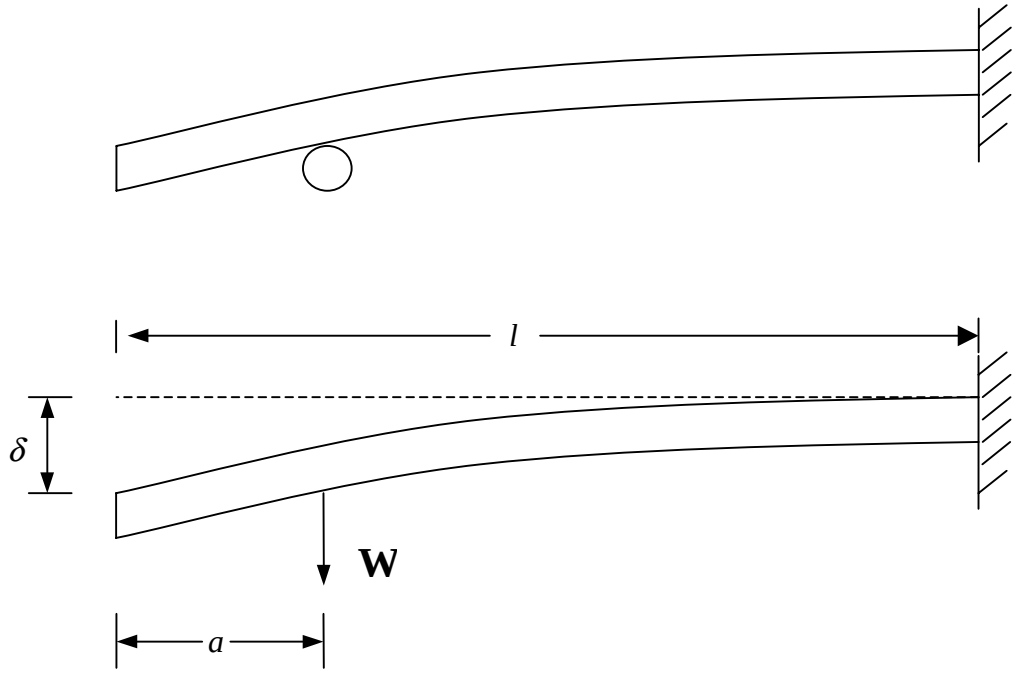

Figure 6.2 Defined quantities for measurement of whisker stiffness.
The top drawing shows a bead attached to the whisker. The bottom drawing is a free-body diagram that defines the variables δ, a, l which are necessary for calculating the whisker stiffness.

The values needed to solve for the stiffness in equation (6.7) are the total deflection of the beam due to the weight (δ), the distance the applied weights are from the end of the whisker (a_i), the radius of the beads (r_i), and the length of the whisker. The density of the beads and the acceleration due to gravity are known quantities. The previously listed unknown quantities are measured by using a reticule located in the eyepiece of the microforge. A sample test demonstrating this calculation of the average stiffness for a whisker is provided in Chapter 7.

6.2 PHOTODIODE EVALUATION

The photoelectronic motion transducer (PMT) is comprised of a dual power supply, low-pass filter, differential instrumentation amplifier, and the photodiode array. This system essentially enables the measurement of small displacements by detecting changes in light intensity due to an object's movement and then conducting a signal comparison between two diodes (explained in section 4.2.2) to determine the distance the object moved. In order to verify that the system is working correctly, the output voltages from the PMT should be plotted versus the displacement of a whisker as it is moved through the photodiode field of view from the outer edge of one diode to the outer edge of the other. The differential amplifier will take the currents from both diodes, convert them to voltages, amplify them, and make one negative. It then sums the negative and positive voltages and produces a single output voltage. Therefore, if both photodiodes see the same light intensity, then the amplifier will make one voltage negative and one positive with equal magnitude and they will add to zero.

If we apply the knowledge of how the PMT works and assume that the first photodiode plate encountered is the plate with the negative voltage, known as the "negative plate", then we will find that when the whisker image crosses the diodes, it will ideally create the plot shown in Figure 6.3. The initial positive incline occurs as the whisker image crosses the border onto the negative plate. This decreases the intensity of the light detected by the negative plate so the differential amplifier will produce a positive voltage. A flat region follows (constant voltage) where the whisker is completely inside the borders of the first plate and the light intensity to which the plate is exposed does not change. As the whisker begins to leave the first plate and enters the gap

in the middle (position 4.5), a decline will occur in the output voltage since the negative plate will begin to see an increase in light intensity. When the whisker reaches the border to enter onto the second plate as it is simultaneously leaving the first plate (position 4.75), the slope of the voltage versus displacement line will increase. This is due to the simultaneous increase in light intensity (i.e., negative voltage) on the first plate as the whisker leaves and the decrease in light intensity (i.e., positive voltage) on the second plate as the whisker enters. The increased rate of voltage change versus distance moved will be constant as long as the whisker is leaving the first plate and entering on the second plate. Once the whisker is completely off of the first plate, yet still entering onto the second, the slope will decrease and return to its previous rate. There will be another region of constant negative voltage when the shadow of the whisker moves within the boundaries of the positive diode. Finally, as the whisker exits the diode, the slope will incline back to zero. These steps are illustrated in Figure 6.3.

Note that the plot shown in Figure 6.3 is only valid when the whisker is larger than the gap between the diodes. If the whisker is smaller than the gap, this will create a flat line in the middle portion of the plot because the whisker will not be crossing any boundaries. However, we do not need to worry about this since our whiskers were slightly larger than the gap. Actually, we neglected the occurrence of the temporary increase in the slope of the plot during our calibrations because we found it occurred for only a small portion of the entire slope.

The pattern described above will be for ideal conditions. This means that the whisker image crossing the borders must be exactly parallel and move perfectly in the direction perpendicular to the borders of the diodes. This is nearly impossible considering the small size of the whisker and diodes and also the slight imperfections that will occur to the whisker during fabrication. Perfect results will also require a light source that produces precisely even illumination; this is extremely difficult as it necessitates exact alignment of the halogen bulb and DIC optics. Among other factors, we would also need the specimen to remain perfectly still and not vibrate as it is being moved. Although we can eliminate the majority, it is nearly impossible to eliminate all external vibrations. Numerous other factors will also contribute to preventing a perfect

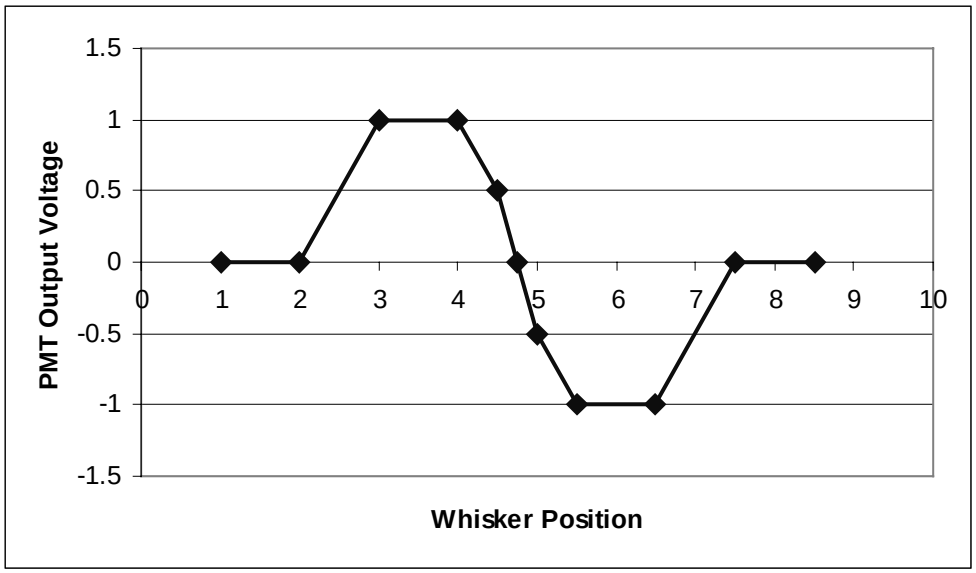

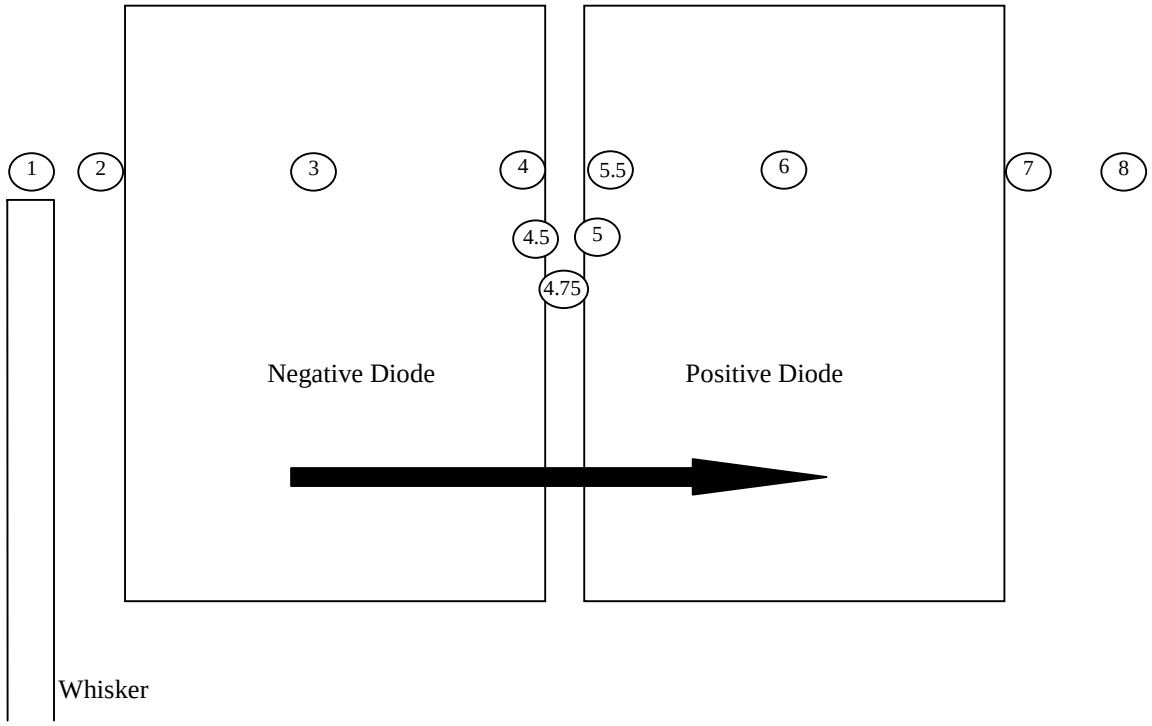

Figure 6.3 Photodiode response for an ideal case.
The photodiodes are tested by moving a whisker across their field of view. The image of the whisker will fall on the diodes as shown above. The circled numbers correspond to the nodes on the above plot and are just relative points, not actual distances. The plot shows the diode array response for an ideal case. Note that if the whisker image covers part of the negative diode, the resulting negative voltage in the differential amplifier will be less, which will lead to a positive output voltage by the PMT. The converse is also true.

signal such as noise in the amplifier circuit. As a result, in the midst of all of the potential problems, reasonably good, yet not ideal, results can be obtained and these will be presented in the next chapter.

6.3 MAPPING THE PHOTODIODE

The video camera is attached to one end of the beam splitter and relays the image of the specimen to the monitor. The opposite end of the splitter guides light to the photodiodes simultaneously. With the monitor, the specimen can be seen as its image is moved across the path of the photodiodes. It is very important that we know where the boundaries of the photodiodes are and exactly where the point in-between them is located. As previously mentioned, the area between the two diodes is a small gap and is the region in which the largest change in volts per micron of movement occurs. For this reason, this is the area of the diodes in which we will conduct testing. We can locate the boundaries by moving an opaque particle across the diodes and noting where the particle is located when the PMT output voltage changes. This is essentially a method for mapping out the boundaries of the photodiodes. The reason for using an opaque particle, such as a sandpaper speck, is because it will block out the light rather well at the single point where it is located and create an easily detected voltage change.

In order to actually figure out the boundaries of the diodes, we scraped a piece of sandpaper over a glass slide and then placed the slide underneath the microscope. We then started far off to one side of the diode array and moved the slide, with particle, using the x-y stage. This will bring the particle across the field of the diodes similar to moving the whisker during the photodiode calibrations. We watched the particle on the monitor and charted where a voltage change was first encountered. This was the beginning of the first boundary and it was marked on a clear plastic sheet placed over the monitor screen. Then, we continued in the same direction until the voltage began to change again. This point was the end of the first diode and the beginning of the gap. This process was continued until we had mapped out the east-west boundaries of the diode. We repeated these steps from north to south as seen on the monitor in order to get the top and bottom boundaries of the diodes. This basic drawing of the diodes' field of view on the monitor was very important because now we could make sure that during tests the whisker was

located in the central region of the two diodes for maximum voltage per micron rates of change.

6.4 SYSTEM TEST WITH IMITATION BUNDLES

In an effort to verify that the PMT was in proper working order and that its results were accurate, we needed to conduct tests on specimens of known stiffness. Since the stiffness of the hair bundles we were seeking to measure are not known, we had to make "imitation hair bundles" of which we could measure the stiffness. These imitation bundles were actually just whiskers whose stiffness we measured using the procedure explained in section 6.1.

We started the system test in the same manner in which we began the tissue tests, with a calibration. A whisker of known stiffness was positioned horizontally in the region where its image was detected by the first diode. The whisker was moved across the first diode and into the field of the second diode with the corresponding voltage versus displacement data being recorded throughout the course of the movement (as explained in 6.2). This data is plotted and serves to calibrate the system by identifying the amount of voltage change per micron of movement. After the calibration, the whisker is returned to its original position and an imitation bundle is now moved to the center of the two photodiodes. The imitation bundle is positioned with its longitudinal axis being vertical so that a cross-sectional view of the bundle will be seen through the microscope (Figure 6.3). The whisker is moved so that it is next to the bundle and barely touching it. At this point, the output voltage of the PMT and the position of the pipette to which the whisker is attached are recorded. The micromanipulator is then used to move the pipette and create a force on the bundle due to the whisker. Eventually, the whisker will push the bundle a small distance, the displacement will be stopped and the recordings of the PMT output voltage and the EFPI displacement will be taken. As explained earlier, the EFPI displacement measures how far the base of the whisker is moved by change in the EFPI sensor's gap distance. The voltage change is used along with the slope found from the calibration to calculate how far the imitation bundle actually moved. These two displacements along with the known stiffness of the whisker are used to find the stiffness of the imitation bundle; this is the same procedure used in a tissue test with a real bundle,

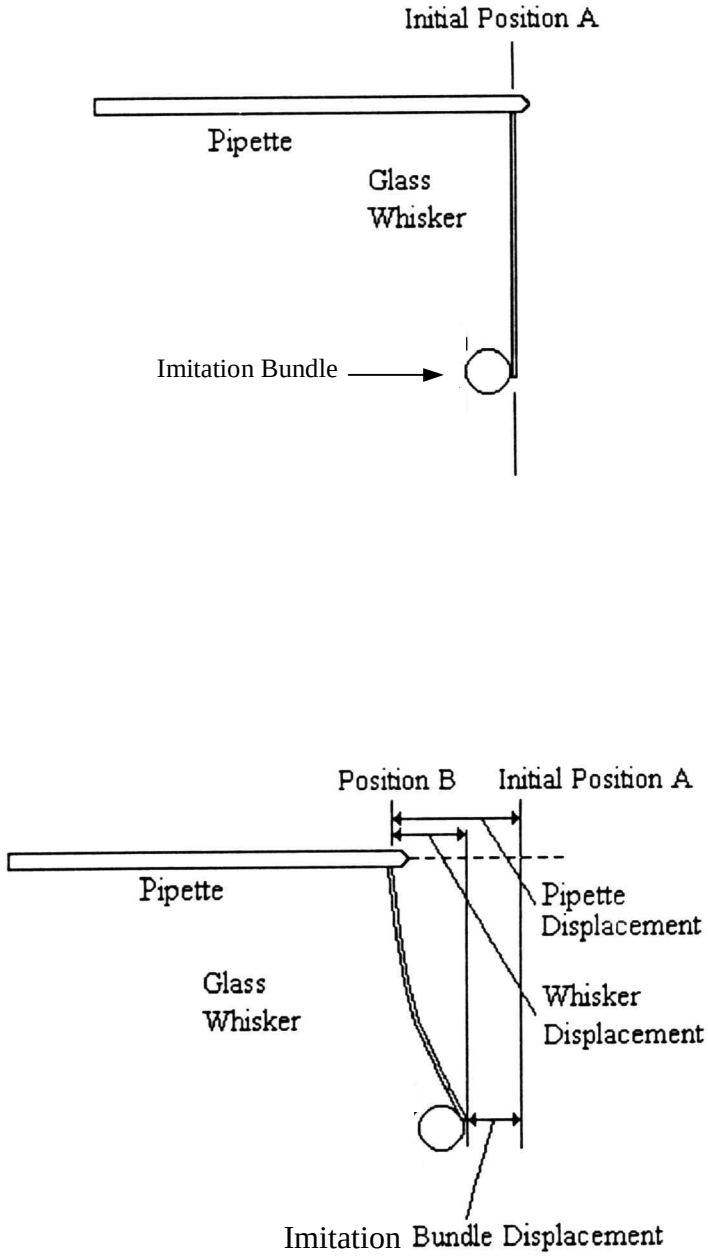

Figure 6.4 Whisker and imitation bundle deflection during system test (adapted from Barrett, 1995).
This schematic shows the whisker being positioned up against the imitation bundle. Then, as the pipette is displaced, the whisker causes a force on the bundle. The whisker bends until the force is large enough to displace the bundle. The resulting displacements are used to calculate the stiffness of the imitation bundle.

as described in section 5.4. The resulting stiffness calculation is then compared with the already known stiffness for the imitation bundle. If the stiffness of the imitation bundle found using the PMT and EFPI is close to the value found using the microforge, then this is good indication that the equipment is performing well. The actual tests done to check the system and their results are shown in Chapter 7.

7.0 RESULTS AND DISCUSSION

This chapter will present the results found from conducting calibrations and tests concerning whisker stiffness, photodiode and system performance, and tissue tests. The results will be interpreted and the findings regarding ciliary bundle stiffness will be compared to results from a computational model.

7.1 WHISKER STIFFNESS RESULTS

The glass whiskers provide the mechanical stimulus for displacing the ciliary bundles. In order to calculate the bundle stiffness, the whiskers needed to have a stiffness small enough so that when they applied a force to the bundle, they would bend prior to moving it (Figure 5.7). This allows the pipette displacement to be larger than the bundle-whisker tip displacement and is necessary in order to correctly solve for the bundle stiffness in equation 5.7.

As previously mentioned, the whisker stiffness was measured by attaching styrene beads and recording the size of the beads, their location on the whisker, and the resulting deflection. This procedure was outlined in section 6.1 and these steps were repeated numerous times for each whisker. Table 7.1 shows the data recorded for a whisker 990 μm in length. The beads that are attached to the whisker each have a density of 1030 kg/m^3. The first four tests were conducted with only one bead attached to the whisker. The fifth, and final, test on the whisker was done with two beads attached.

The last column in the table shows the stiffness calculated for the whisker. This stiffness is the sum of the stiffness due to the weight of the first bead (k_1) and that due to the weight of the second bead (k_2) made possible by the principle of superposition. These values were found from equation 6.7. The five stiffness values were used to calculate an average stiffness of 3.94 E-05 N/m. The scatter in the stiffness results produced a standard deviation of 3.53 E-06 N/m. This whisker will be a bit stiff for conducting tests on flimsy medial II ciliary bundles, but should be suitable for tests on most striolar bundles. Additional whiskers were fabricated and we measured their stiffness using the

Table 7.1 Whisker stiffness values.

Trial	# of beads	Bead Diameter (mm)	Bead Weight (N)	Bead Location (mm)	Total Deflection (mm)	**k1** (N/m)	Bead Diameter (mm)	Bead Weight (N)	Bead Location (mm)	Total Deflection (mm)	**k2** (N/m)	**Whisker Stiffness (K)** [N/m]
1	1	0.068	1.66E-09	0.01	0.047	3.49E-05	-	-	-	-	0	**3.49E-05**
2	1	0.088	3.61E-09	0.047	0.08	4.19E-05	-	-	-	-	0	**4.19E-05**
3	1	0.082	2.92E-09	0.087	0.06	4.23E-05	-	-	-	-	0	**4.23E-05**
4	1	0.057	9.81E-10	0	0.027	3.63E-05	-	-	-	-	0	**3.63E-05**
5	2	0.065	1.45E-09	0.013	0.081	1.76E-05	0.077	2.42E-09	0.13	0.081	2.4E-05	**4.16E-05**

Average Stiffness = 3.94 E-05 N/m **Standard Deviation = 3.53 E-06 N/m**

exact same method. We made whiskers that ranged in stiffness from 5.0 E-06 N/m to 3.0 E-04 N/m and used them according to which type of cells were being tested.

7.2 PHOTODIODE EVALUATION RESULTS

The photodiodes are detectors that sense light and emit a current proprtional to the intensity of light to which they are exposed. They are extremely sensitive light sensors and can detect very tiny changes in light shift and intensity. When they are used as part of a PMT, they are capable of accurately measuring small displacements. That is the reason why we chose to use them to measure the distance a ciliary bundle is deflected by a whisker. After the PMT has been assembled, we must make sure that the diodes are working correctly. This is accomplished by evaluating the diodes performance with the steps outlined in section 6.2.

In our initial amplifier circuit, we were using low power operational amplifiers (Motorola LM324A). As we moved the whisker across the field of the diodes and recorded the displacement and PMT voltage output, we plotted the pattern seen in Figure 7.1. This plot did not show any of the trends for the ideal case with the exception of a somewhat linear region at the center of the field of the diodes. Although we did not expect results exactly like the ideal case, we felt that this plot was the result of experimental error or malfunctioning circuitry. While checking the circuit components, we found that the operational amplifiers we were using were causing some malfunction in the circuit. As a result, we decided to use the low-noise precision amplifiers (AD OP-27) that had been recommended. Upon reconfiguring the circuit and conducting a second test run at 40×1.6 magnification, we arrived at the result shown in Figure 7.2. This plot more closely resembled the trends from the ideal case, but there are a few extra peaks for which we could not account. Also, the negative spike due to the whisker covering part of the positive plate had a much larger magnitude than the spike for the negative plate.

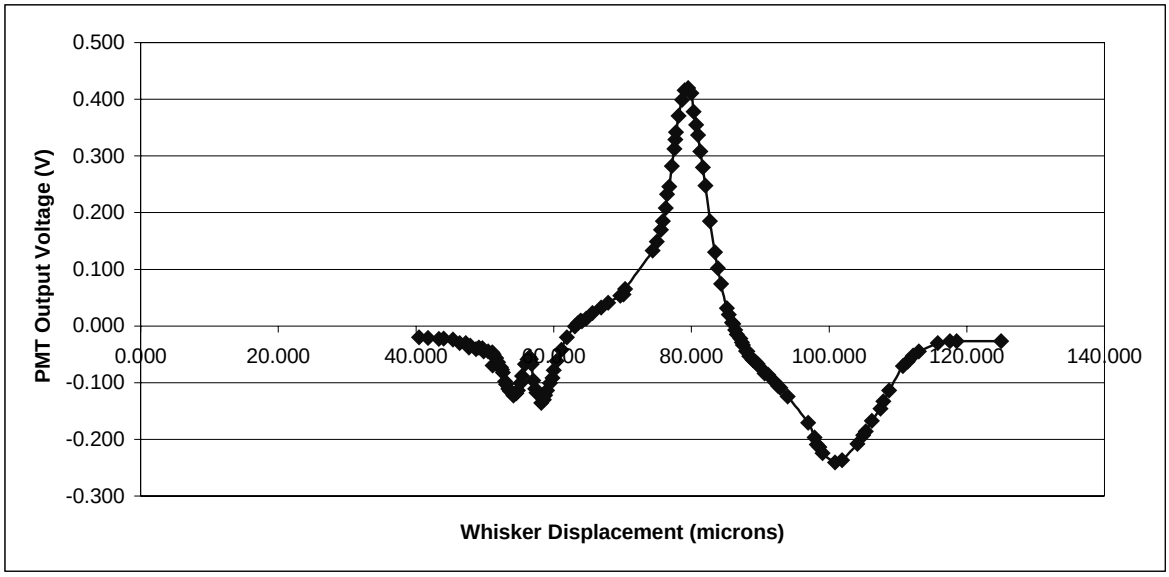

Figure 7.1 Initial PMT response to whisker movement.
This test was done with a 2.4μm whisker at a magnification of 40×1.6 and a PMT supply voltage of 6.02 V. The plot shows signs of photodiode response, but does not resemble the ideal case and shows no flat regions of constant voltage where the whisker is completely within one of the diode borders.

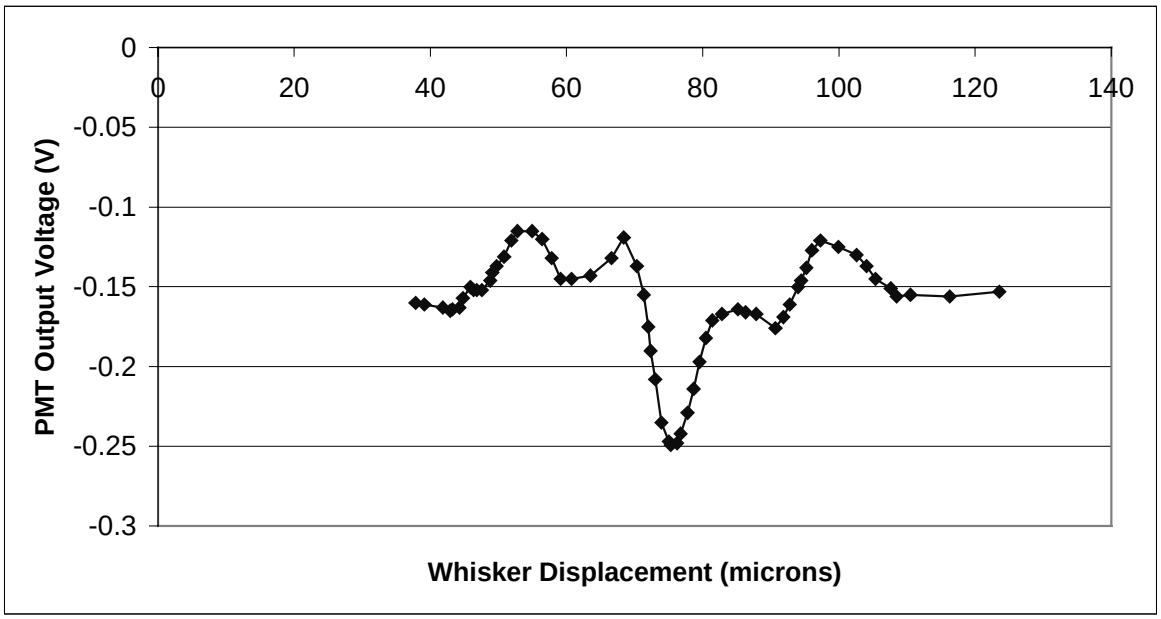

Figure 7.2 PMT response after replacing operational amplifiers.
This test was done with a 2.4μm whisker at a magnification of 40×1.6 and a PMT supply voltage of 6.02 V. The operational amplifiers in the circuit were replaced with low-noise precision op-amps. They seem to show a better response to whisker movement. There is an obvious linear region in the center with two peaks representing the image crossing the borders of the diodes. However, there are still no regions of constant voltage.

We consulted with others familiar with light microscopes equipped with DIC optics as we were concerned that maybe shadows from the whisker were causing the discrepancies. It was suggested that we examine the settings of the optics, more specifically the Wollaston prism. As previously mentioned, the Wollaston prism controls the contrast, field brightness, and sensitivity of the DIC optics. It can be changed by turning a small knob. So, unsure of the effects of turning the knob, we conducted trial and error tests. The knob was turned slightly and the photodiode response to whisker movement was evaluated. We finally reached a setting where the test results were significantly closer to the ideal cased and seemed to no longer improve with any prism adjustments. This test was done with a 2.4 μm whisker at a 40×1.6 magnification and the results are depicted in Figure 7.3. Although there are some unexpected small peaks, two regions of somewhat constant voltage do occur where the whisker is entirely within the positive and negative diode borders. Also, there is a very nice linear region at the center of the plot. We were rather satisfied since this was the region in which we would be conducting tests. An additional positive result was the symmetry evident in the plot which implies the correct functioning of the diodes and good optical alignment.

However, we were not yet done. We wanted to verify that the PMT could produce results even closer to the ideal case. We decided to use a larger whisker and a lower magnification in a test. We theorized that because the voltage response would be of a larger magnitude, this would overwhelm any small errors that the diode may be picking up due to a whisker that traveled across the field at an angle or had rough edges. The result is plotted in Figure 7.4. This plot shows excellent results as it closely mirrors the ideal case. This confirms that the PMT is working correctly. However, we cannot conduct tests at this magnification, because it is not strong enough to see the ciliary bundles. The tests are conducted with a 40x lens and the optivar set at 1.6x.

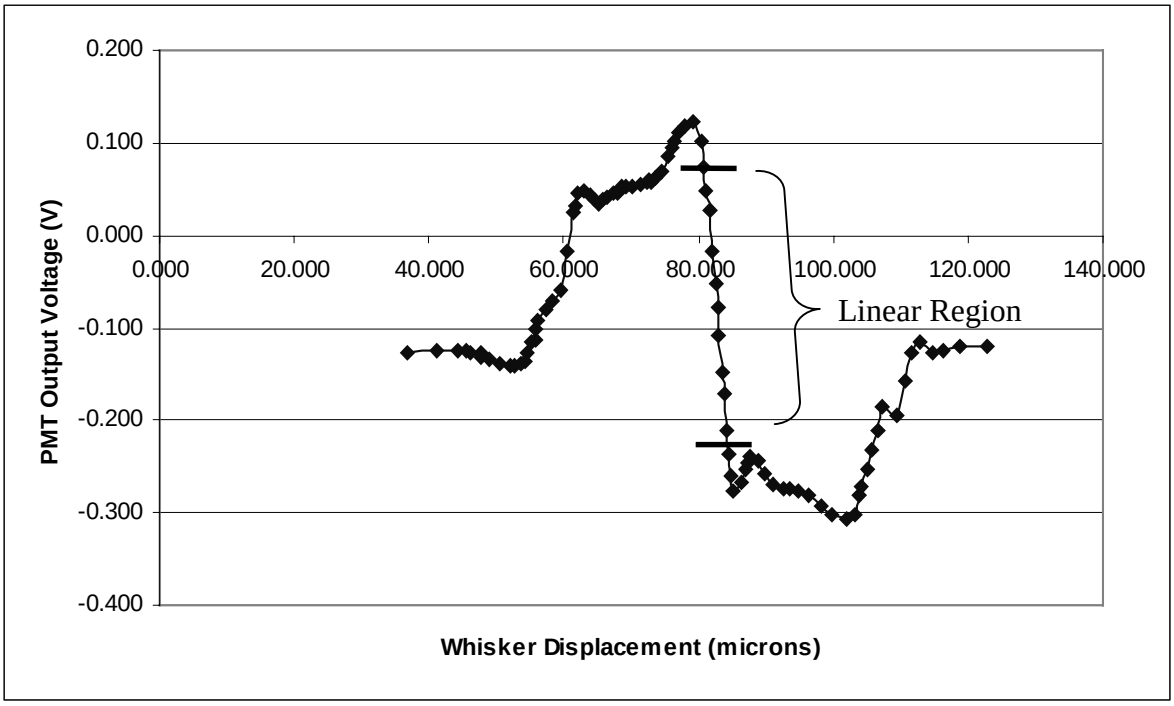

Figure 7.3 PMT response after adjusting Wollaston prism.
This test was done with a 2.4μm whisker at a magnification of 40×1.6 and a PMT supply voltage of 6.02 V. The Wollaston prism was adjusted until the PMT response no longer improved. Symmetry is evident in this result as well as two regions of semi-constant voltage. More importantly, the central region shows a nice linear displacement-voltage relationship. This is the region in which testing will occur and is marked by the two horizontal lines. The differences between this plot and the ideal case may lie in whisker alignment, whisker imperfections, slight misalignments with the optics, or noise in the PMT circuitry.

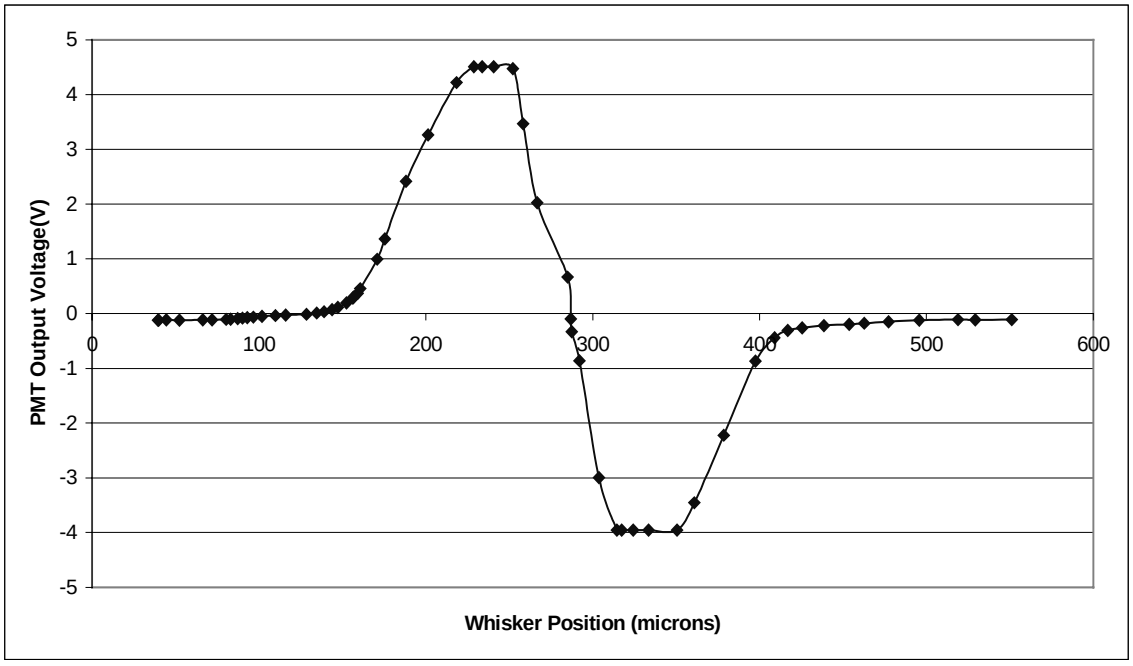

Figure 7.4 PMT response using large whisker.
This test was done with a 70 μm whisker at a magnification of 10×2 and a PMT supply voltage of 6.02 V. The larger whisker will elicit a greater voltage response from the diodes because it is capable of covering more of the diode at one time. As a result, it overwhelms the small voltage jumps due to the whisker and optical alignment or noise in the circuitry that are seen in Figure 7.3. Although this magnification is not strong enough to use for testing on ciliary bundles, it does prove the PMT is performing correctly.

7.3 SYSTEM TEST RESULTS

Prior to conducting the actual tissue tests, the system needs to be evaluated in order to verify its capabilities in measuring the stiffness of ciliary bundles. To check the system, we conducted tests on a whisker and referred to it as an imitation bundle. We measured the stiffness of the imitation bundle using styrene beads, and then measured its stiffness again by deflecting the imitation bundle with a whisker and measuring the resulting displacements with the PMT and EFPI equipment. The steps used to conduct the system check are the same used for an actual test and include a calibration along with actually deflecting the imitation bundle as if it were a ciliary bundle.

7.3.1 PMT Calibration Results

The calibration of the system prior to each set of tests with the imitation bundle will provide the relationship between whisker displacement and PMT output voltage. We are only interested in the central linear region seen in Figure 7.3. After all of the problems mentioned above were fixed, we were ready to conduct calibrations by performing the procedure outlined in section 6.4.

For each set of tests on a particular imitation bundle, the calibrations were performed more than once. The calibration results for tests A, B, and C are shown in Figures 7.5, 7.6, and 7.7, respectively. These tests only display the linear portion of the PMT response as the whisker crosses between the diodes. A line is fit to the data points and the slope of that line is taken to be the calibration factor. Since more than one calibration was done for a particular test, the values were averaged to get the calibration factor to be used in calculations. The R^2 values were included to show how well the trendline fits the data. An R^2 value equal to 1 would be a perfect fit to a straight line.

Tests A, B, and C were conducted at a magnification of 40x1.6 with whiskers ranging between 1-4 μm. The two calibrations for Test A resulted in an average calibration factor of 0.0756 volts/micron. The results for Test B and Test C were 0.0771 and 0.0582 volts/micron, respectively. These results show how the voltage-displacement ratio can differ for the PMT when things such as the light intensity, whisker size, and image background are changed just slightly. This is why the calibrations must be done

prior to each set of tests and also why lighting, background, etc. must not be altered at any point during a test.

7.3.2 Imitation Bundle Stiffness Test Results

Upon completion of the calibration, the whisker was placed up against the tip of the imitation bundle (Figure 6.4) in the center of the two diodes. The values for the EFPI gap distance and the PMT output voltage were recorded. The pipette was then displaced, causing the whisker to apply a force to the imitation bundle (IB). The bundle bent until the force was large enough to displace the whisker. After a small displacement, the pipette was stopped and the EFPI and PMT readings were again recorded. The pipette and IB were returned to their original positions and the test was repeated numerous times.

The tables in figures 7.5, 7.6, and 7.7 display the data recorded during tests A, B, and C. The first column in the tables indicates the number of trials conducted for a particular test on the imitation bundle. The second column represents the gap distance registered by the EFPI sensor. The first value is the starting position of the pipette and the second value is the ending position. Therefore, the difference in these two values is the change in the EFPI gap distance, or the distance the pipette has moved (Δx_P). The absolute value of the difference is calculated in Column 3. The fourth column shows the PMT output voltage when the whisker is up against the bundle and then again when the whisker has displaced the bundle. The absolute difference in this value is provided in the fifth column. Column five is divided by the calibration factor calculated from the slope of the trendline in order to get column six. This value is the actual distance that the bundle has been displaced (Δx_B). Column seven is the experimentally measured stiffness of the imitation bundle. This is found using equation 5.7. The whisker stiffness, k_W, is known and the values for Δx_B and Δx_P were just calculated so the equation can be solved for the imitation bundle stiffness, k_B.

Table 7.2 summarizes the results and includes the stiffness of the whisker used for deflection, both the IB stiffness found by using styrene beads and by using the PMT/EFPI, and the difference between these two values. Test A showed a 4.43% error between the microforge and the experimental values for the IB. Tests B and C had errors of 4.14% and 1.38%, respectively. The two methods for measurement of the IB stiffness are rather close and this proves that the PMT/EFPI technique is in good working order.

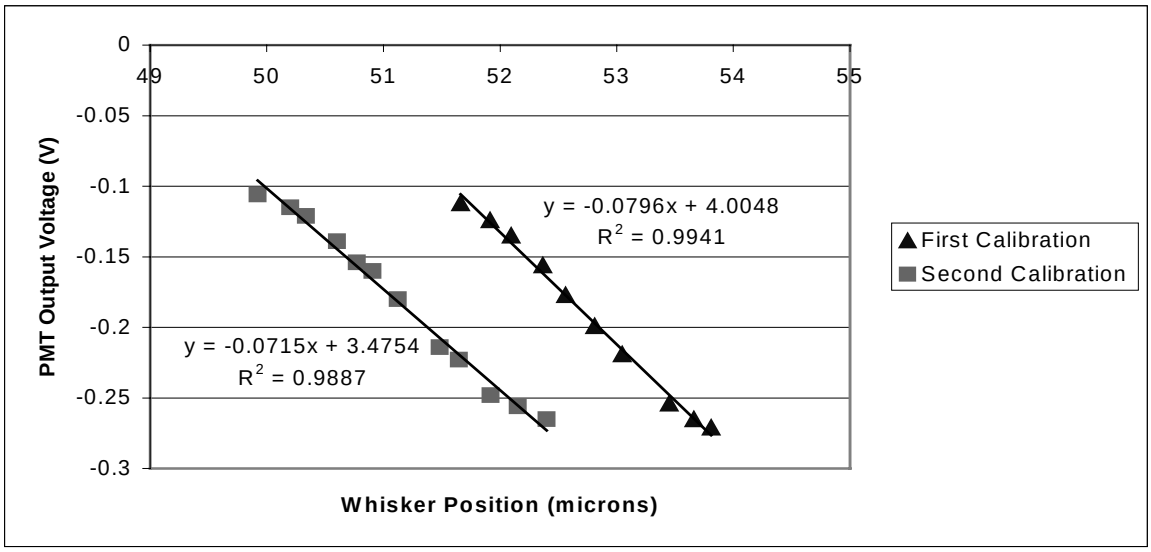

Trial	Pipette Position (microns)	Pipette Displacement (microns)	PMT Output Voltage (V)	Absolute Voltage Change (V)	Imitation Bundle Displacement (microns)	**Imitation Bundle Stiffness (N/m)**
1	53.695 54.269	0.574	-0.283 -0.3	0.017	0.2250	**2.92E-05**
2	51.305 52.91	1.605	-0.248 -0.27	0.022	0.2912	**8.49E-05**
3	52.804 53.794	0.99	-0.259 -0.275	0.016	0.2118	**6.91E-05**
4	57.594 58.904	1.31	-0.227 -0.256	0.029	0.3839	**4.54E-05**
5	99.942 100.843	0.901	-0.231 -0.248	0.017	0.2250	**5.65E-05**
6	101.551 102.419	0.868	-0.249 -0.266	0.017	0.2250	**5.37E-05**
7	100.387 100.908	0.521	-0.221 -0.231	0.01	0.1324	**5.52E-05**
8	100.371 101.228	0.857	-0.22 -0.23	0.01	0.1324	**1.03E-04**
9	97.748 98.703	0.955	-0.174 -0.181	0.007	0.0927	**1.75E-04**
10	98.703 99.632	0.929	-0.173 -0.184	0.011	0.1456	**1.01E-04**

Figure 7.5 System test results for Test A.
The whisker for this test had a stiffness of 1.77 E-05 N/m. The two calibration factors taken from the plot were averaged to be 0.0756 volts/micron. Ten trials were conducted on the imitation bundle with the stiffness values seen in the right column. The average stiffness value for this test was 7.73 E-05 N/m.

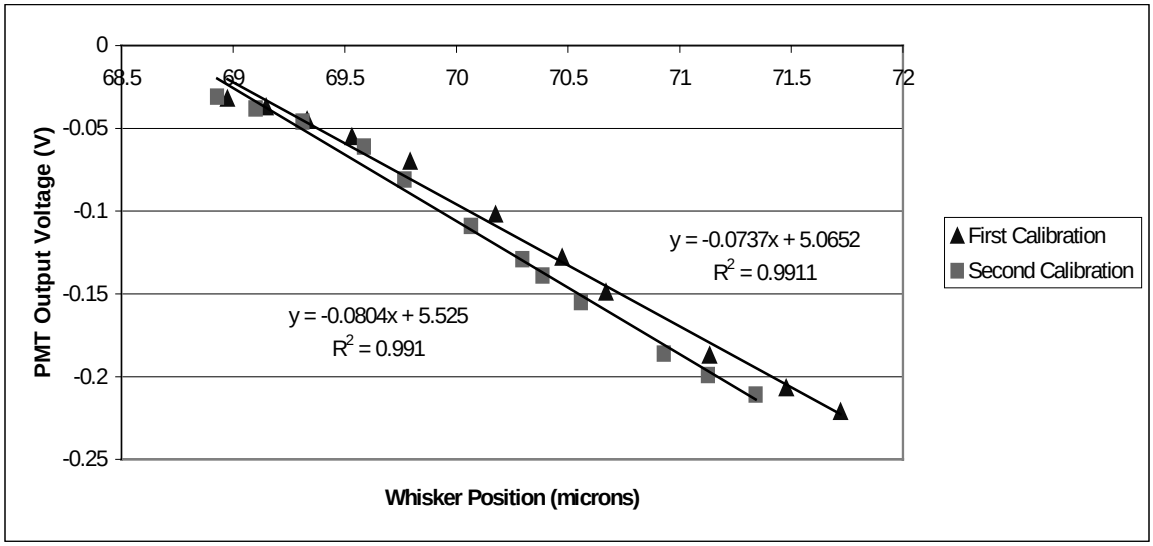

Trial	Pipette Position (microns)	Pipette Displacement (microns)	PMT Output Voltage (V)	Absolute Voltage Change (V)	Bundle Displacement (microns)	**Imitation Bundle Stiffness (N/m)**
1	46.026 46.727	0.701	-0.149 -0.159	0.01	0.1298	**2.85E-04**
2	44.99 45.752	0.762	-0.125 -0.138	0.013	0.1687	**2.28E-04**
3	45.867 47.083	1.216	-0.144 -0.164	0.02	0.2596	**2.38E-04**
4	46.958 47.863	0.905	-0.153 -0.168	0.015	0.1947	**2.36E-04**
5	45.259 46.269	1.01	-0.132 -0.144	0.012	0.1557	**3.55E-04**
6	46.075 47.039	0.964	-0.142 -0.151	0.009	0.1168	**4.69E-04**

Figure 7.6 System test results for Test B.
The whisker for this test had a stiffness of 6.47 E-05 N/m. The two calibration factors taken from the plot were averaged to be 0.0771 volts/micron. Six trials were conducted on the imitation bundle with the stiffness values seen in the right column. The average stiffness value for this test was 3.02 E-04 N/m.

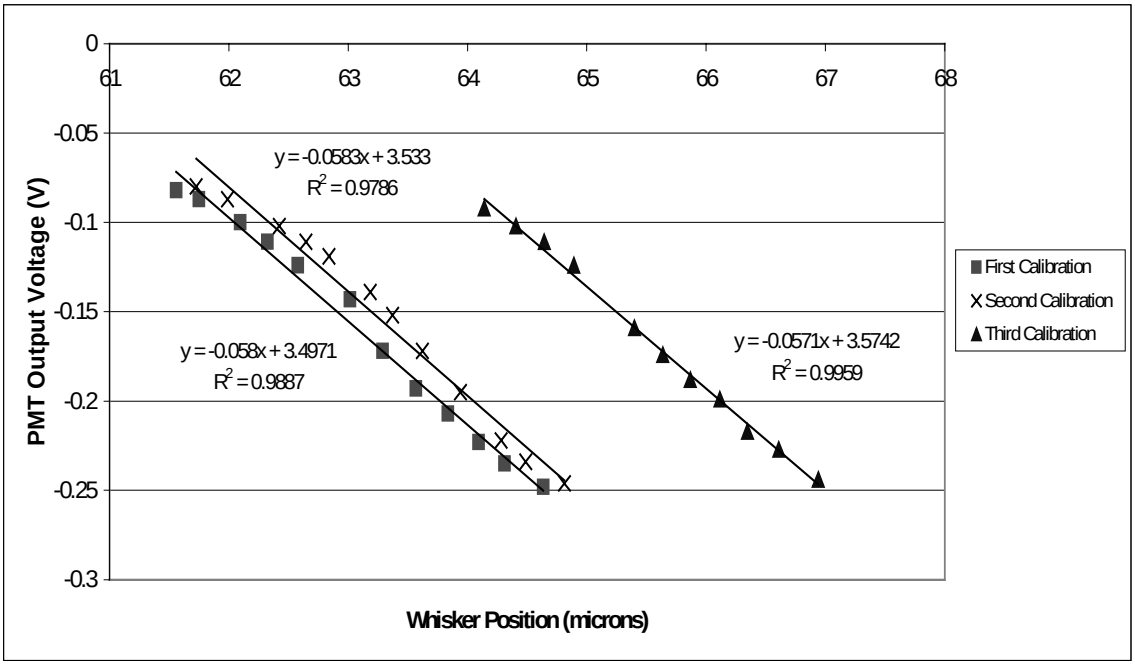

Trial	Pipette Position (microns)	Pipette Displacement (microns)	PMT Output Voltage (V)	Absolute Voltage Change (V)	Bundle Displacement (microns)	**Imitation Bundle Stiffness (N/m)**
1	64.54 65.615	1.075	-0.163 -0.17	0.007	0.1211	**5.10E-04**
2	67.287 68.481	1.194	-0.2005 -0.214	0.0135	0.2336	**2.66E-04**
3	66.965 67.777	0.812	-0.198 -0.207	0.009	0.1557	**2.73E-04**
4	66.444 67.907	1.463	-0.195 -0.213	0.018	0.3114	**2.39E-04**
5	68.108 68.836	0.728	-0.214 -0.228	0.014	0.2422	**1.30E-04**
6	65.606 66.672	1.066	-0.18 -0.191	0.011	0.1903	**2.98E-04**
7	66.367 67.041	0.674	-0.191 -0.201	0.01	0.1730	**1.87E-04**
8	68.218 69.248	1.03	-0.214 -0.229	0.015	0.2595	**1.92E-04**
9	66.719 67.611	0.892	-0.198 -0.211	0.013	0.2249	**1.92E-04**
10	64.772 66.261	1.489	-0.174 -0.189	0.015	0.2595	**3.07E-04**
11	67.247 67.941	0.694	-0.204 -0.221	0.017	0.2941	**8.80E-05**

Figure 7.7 System test results for Test C.

The whisker for this test had a stiffness of 6.47 E-05 N/m. The two calibration factors taken from the plot were averaged to be 0.0582 volts/micron. Eleven trials were conducted on the imitation

bundle with the stiffness values seen in the right column. The average stiffness value for this test was 2.86 E-04 N/m.

Table 7.2 Imitation Bundle (IB) Test Results

Test	Whisker Stiffness (N/m)	Average IB Stiffness-Microforge (N/m)	Average IB Stiffness-PMT/EFPI (N/m)	Percent Error (%)
A	1.77E-05	7.40E-05	7.73E-05	4.43
B	6.47E-05	2.90E-04	3.02E-04	4.14
C	6.47E-05	2.90E-04	2.86E-04	1.38

7.4 TISSUE TEST RESULTS

The tissue tests were conducted in the same manner as with the imitation bundle: calibration first and then numerous static measurements of the bundle displacement. Twenty-five tests were conducted on two types of hair cells: 12 medial II and 13 striolar hair cells.

7.4.1 Medial II Stiffness Results

The medial II type hair cells were much easier to find along the transect of the utricle because, due to their location, they were less likely to be disturbed during dissection. However, these cells were much harder to conduct tests on due to their stiffness. The glass whisker had to apply the force to a kinocilium that was much taller than the surrounding stereocilia. The hair bundle being rather limp, small forces by the glass whisker will displace it. Therefore, testing on these hair cells required only small pipette displacements. Good data would be the result of careful testing and accurate measurements.

A representative test for medial II cells is presented in Figure 7.8. The name of this test was T20. This test used a whisker with a 1.6 E-05 N/m stiffness to deflect a medial II bundle with a kinocilium height of 13.1 μm. One calibration was done and ten

tissue tests were conducted. The plot in the figure shows the calibration and the calibration factor, which was approximately 0.070 volts/micron. The calibration factor

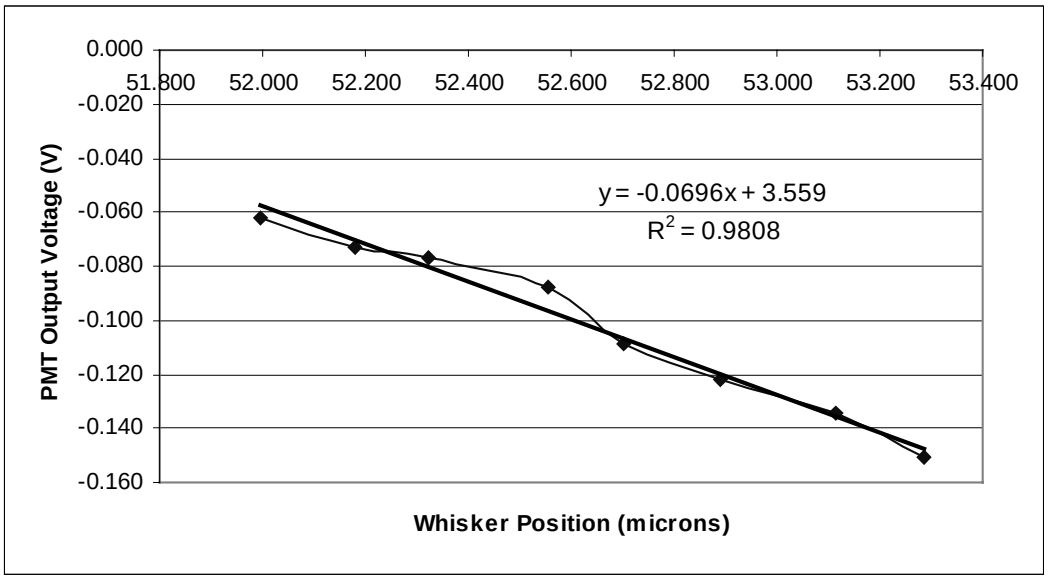

Trial	Pipette Displacement (microns)	Absolute PMT Voltage Change (V)	Bundle Displacement (microns)	Applied Force (pN)	**Bundle Stiffness (N/m)**
1	1.43	0.051	0.73	11.17	**1.52E-05**
2	0.80	0.026	0.37	6.89	**1.84E-05**
3	0.87	0.024	0.34	8.37	**2.43E-05**
4	1.53	0.051	0.73	12.82	**1.75E-05**
5	0.93	0.032	0.46	7.49	**1.63E-05**
6	0.37	0.011	0.16	3.39	**2.15E-05**
7	0.38	0.012	0.17	3.34	**1.94E-05**
8	0.63	0.02	0.29	5.40	**1.88E-05**
9	0.70	0.021	0.30	6.37	**2.11E-05**

Figure 7.8 Tissue test results for medial II bundle test T20.
The whisker for this test had a stiffness of 6.47 E-05 N/m. The calibration factor taken from the plot was 0.0696 volts/micron. Nine trials were conducted on the medial II bundle. The average stiffness value for this test was 1.92 E-05 N/m.

and the displacements of both the pipette and bundle were used to find the stiffness of the bundle. The average stiffness for this hair cell was 1.92 E-05 N/m and there does not seem to be any cell fatigue occurring in the later tests.

An additional column has been included in this table that shows the amount of force that was applied to the bundle for a corresponding displacement. This was calculated by using the known whisker stiffness (k_W) and multiplying it by the calculated whisker displacement (Δx_W) (equations 5.4, 5.5, 5.6). It required only a few piconewtons to displace the bundle hundreds of nanometers. Figure 7.9 shows the force-displacement data from the experiment with a linear regression fit. The data fit reasonably well.

However, some researchers suggest that these data will never fit perfectly and that some scatter is expected [Russell, 1992]. They present empirical results which show that stiffness can vary with the magnitude of deflection. This could be due to the mechanics of the hair cell itself and the relationship of the kinocilium to the stereocilia. Their results imply that since the stiffness may not be constant, then the force-displacement relationship may not be linear. Further tests would need to be done to defend or counter this research.

A total of twelve medial II bundles were tested. The results from these tests are presented in Table 7.3. The measured height of the kinocilium, max height of the stereocilia, and bundle width are also included in the table. The stereocilia height is measured as the maximum height of any stereocilia on the cell. The bundle width is measured as the distance from kinocilium base to the base of the stereocilia furthest away while the cell is seen in profile. The stiffness of the medial II bundles range from 0.26 to 2.62 E-05 N/m.

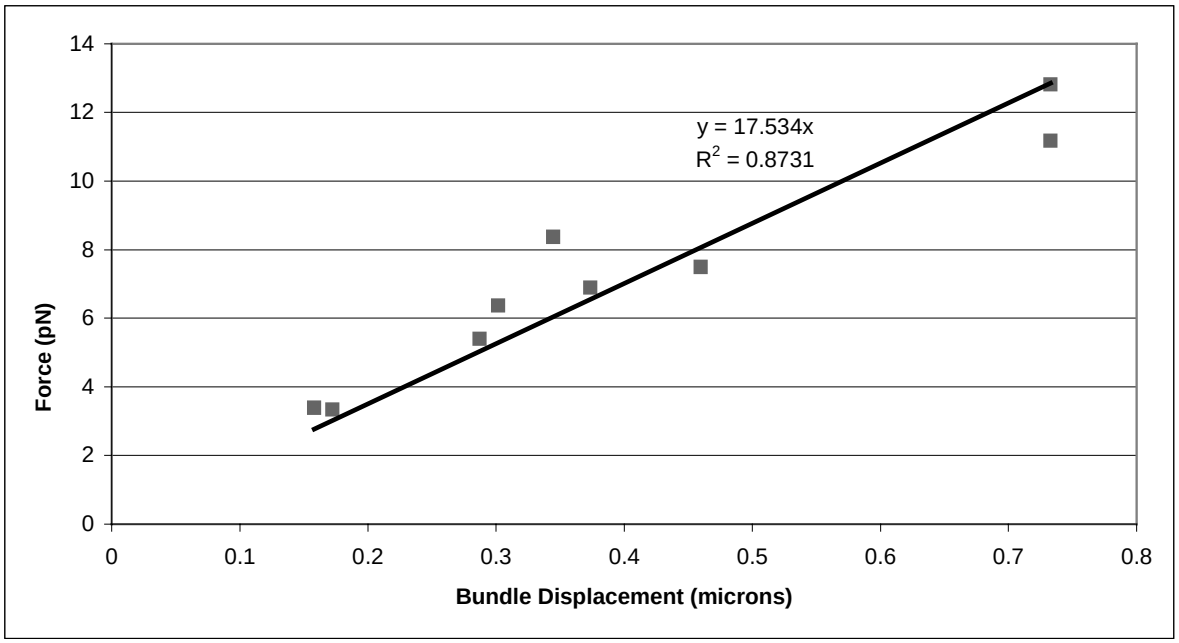

Figure 7.9 Force vs. displacement data for medial II test T20.
The general trend of the data displays how an increased applied force increases bundle displacement. A linear regression is added and the slope of the line is fit through (0,0). This is an additional estimate of bundle stiffness which is 1.75 E-05 N/m.

Table 7.3 Medial II bundle stiffness results and dimensions.

Test	Kinocilium Height (microns)	Stereocilia Height (microns)	Bundle Width (microns)	Bundle Stiffness (x E-05 N/m)
T2	16.3	4.6	4.4	2.62
T3	7.2	3.5	3.6	1.28
T4	11.5	3.9	5.0	0.94
T5	11.2	3.9	4.8	1.16
T6	14.8	4.2	4.1	1.00
T7	7.7	2.7	2.2	0.60
T8	14.7	3.8	5.2	2.38
T16	16.0	5.1	3.0	0.26
T17	12.2	3.3	3.6	1.37
T20	13.1	3.9	4.7	1.92
T21	11.7	3.6	4.2	0.74
T23	10.8	3.4	1.8	1.69

7.4.2 Striolar Stiffness Results

Hair cells in the striolar region had ciliary bundles that appeared much thicker due to the size of the stereocilia. The stereocilia were very large in comparison to those found in medial II cells. These bundles were much stiffer and therefore easier on which to conduct tests.

A representative test for striolar cells is presented in Figure 7.10. The name of this test was T18. This test used a whisker with a 1.6 E-05 N/m stiffness to deflect a striolar bundle with a 6.2 μm kinocilium. One calibration was done and ten tissue tests were conducted. The plot in the figure shows the calibration and the calibration factor, which was approximately 0.038 volts/micron. The calibration factor and the displacements of both the pipette and bundle were used to find the stiffness of the bundle. The average stiffness for this hair cell was 2.71 E-04 N/m. This stiffness value is more than an order of magnitude greater than the measured stiffness of the medial II bundle in T20.

The forces required to deflect the bundle the given distances are provided in column five. The force required to deflect the striolar bundle in T18 are significantly larger than those forces needed to move the medial II bundle in T20 a comparable distance. Figure 7.11 shows the force-displacement data for this particular striolar cell. The linear regression fit approximates the data reasonably well with some noticeable scatter.

A total of thirteen striolar bundles were tested. The results from these tests are presented in Table 7.4. The dimensions of the hair bundles are also included in the table. The stiffness of the striolar bundles range from 2.83 to 27.10 E-05 N/m. The majority of these values are much larger than the stiffness values for the medial II bundles. The dimensions of these bundles show that they are shorter and have a smaller width. This makes them more compact and therefore more stiff.

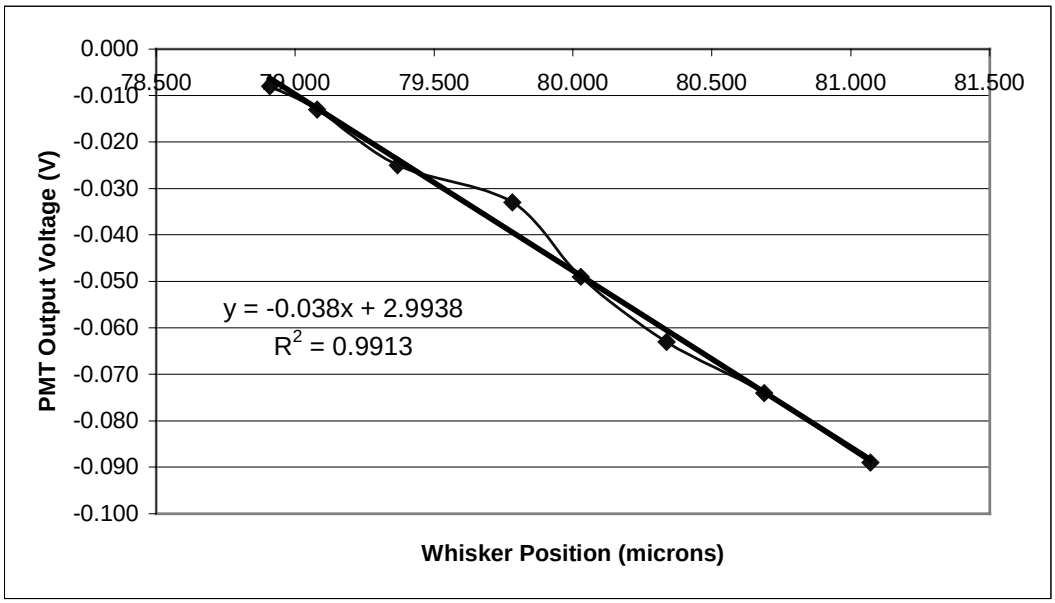

Trial	Pipette Displacement (microns)	Absolute PMT Voltage Change (V)	Bundle Displacement (microns)	Applied Force (pN)	**Bundle Stiffness (N/m)**
1	1.73	0.003	0.08	26.48	**3.35E-04**
2	1.91	0.004	0.11	28.86	**2.74E-04**
3	1.50	0.005	0.13	21.94	**1.67E-04**
4	10.16	0.025	0.66	152.07	**2.31E-04**
5	2.88	0.007	0.18	43.18	**2.34E-04**
6	6.56	0.013	0.34	99.52	**2.91E-04**
7	4.27	0.016	0.42	61.63	**1.46E-04**
8	4.65	0.006	0.16	71.86	**4.55E-04**
9	3.82	0.006	0.16	58.53	**3.71E-04**
10	2.88	0.008	0.21	42.74	**2.03E-04**

Figure 7.10 Tissue test results for striolar bundle test T18.
The whisker for this test had a stiffness of 6.47 E-05 N/m. The calibration factor taken from the plot was 0.038 volts/micron. Ten trials were conducted on the medial II bundle. The average stiffness value for this test was 27.10 E-05 N/m.

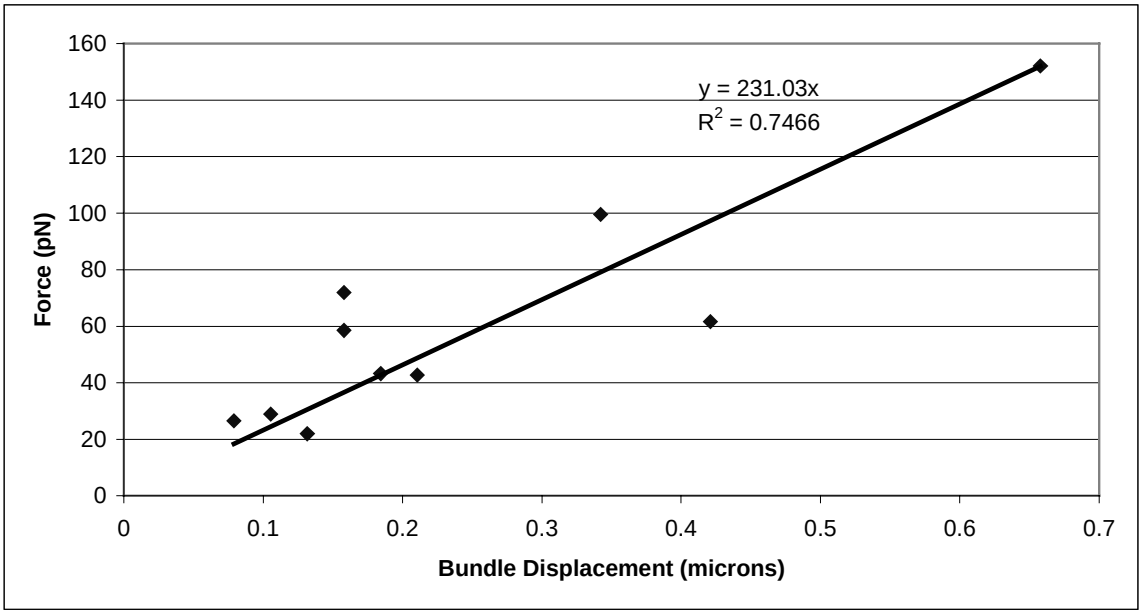

Figure 7.11 Force vs. displacement data for striolar test T18.
The general trend of the data displays how an increased applied force increases bundle displacement. A linear regression is added and the slope of the line is fit through (0,0). This is an additional estimate of bundle stiffness which is 23.1 E-05 N/m.

Table 7.4 Striolar bundle stiffness results and dimensions.

Test	Kinocilium Height (microns)	Stereocilia Height (microns)	Bundle Width (microns)	Bundle Stiffness (x E-05 N/m)
T1	5.5	4.0	2.5	20.70
T9	4.9	3.9	2.8	9.40
T10	9.1	8.4	5.3	16.20
T11	3.5	1.9	2.4	16.20
T12	5.9	4.9	4.9	2.83
T13	4.8	3.4	3.6	3.57
T14	6.4	4.1	4.6	6.18
T15	4.4	4.3	3.6	6.68
T18	6.2	5.4	3.5	27.10
T19	6.6	5.2	4.6	12.60
T22	6.3	2.8	3.1	9.97
T24	6.2	5.7	4.8	4.54
T25	4.4	3.1	2.5	4.15

7.4.3 Linear Stiffness Comparison

The mean stiffness value for the medial II bundles is 1.33 E-05 N/m, whereas the mean value for the striolar bundles is 1.08 E-04 N/m. There is approximately an order of magnitude of difference between these values. However, the stiffness results for both the medial II and striolar ciliary bundles cover a wide spectrum of values. In fact, Figure 7.12 plots the stiffness values for both the striolar and medial II bundles in descending order. This stiffness we have been discussing is labeled "linear stiffness" in the plot for purposes of comparison to a "torsional stiffness" in the next section. The resulting trend of the data is almost ideally fit by an exponential regression analysis curve. It is very interesting to see that the stiffness of the striolar and medial II bundles do not overlap. In fact, the upper limits for medial II stiffness values seem to begin where the lower levels of stiffness values for striolar bundles end. Although this data is preliminary, it is evidence that bundle stiffness is not specific and varies over a wide spectrum for particular types of cells. We have included error bars on the plot which represent one standard deviation for the test results on that particular cell. These bars show the scatter of results and, as expected, bundles with lower stiffness have less scatter and vice-versa. Figure 7.13 shows the same data, but the error bars now are calculated to show 95% confidence levels.

In Figure 7.14, we grouped the tests by the specimen from which they were taken. We wanted to examine any possible specimen specific trends in hair cell stiffness. This plot shows that the test results were relatively consistent on a specimen-to-specimen basis. For example, the striolar results from specimen #5 are all somewhat lower than other striolar cell results. However, all of the results from this turtle are consistently lower, which may imply that bundle stiffness is dependent upon animal age and size. Regardless, the stiffness results obtained obviously vary from specimen to specimen.

We also conducted a student's t-distribution using critical values of t [Sokal and Rolf, 1981] on the entire population of tests. We grouped the trials into tests done on medial II and striolar bundles. The analysis provided a mean striolar stiffness of $11.62 \pm 10.6 \times 10^{-5}$ N/m and a mean medial II stiffness of $1.29 \pm 1.04 \times 10^{-5}$ N/m. The p-value comparing the two populations was 2.19×10^{-18}. This is statistically significant because it provides evidence that the two populations are distinct and the results are repeatable.

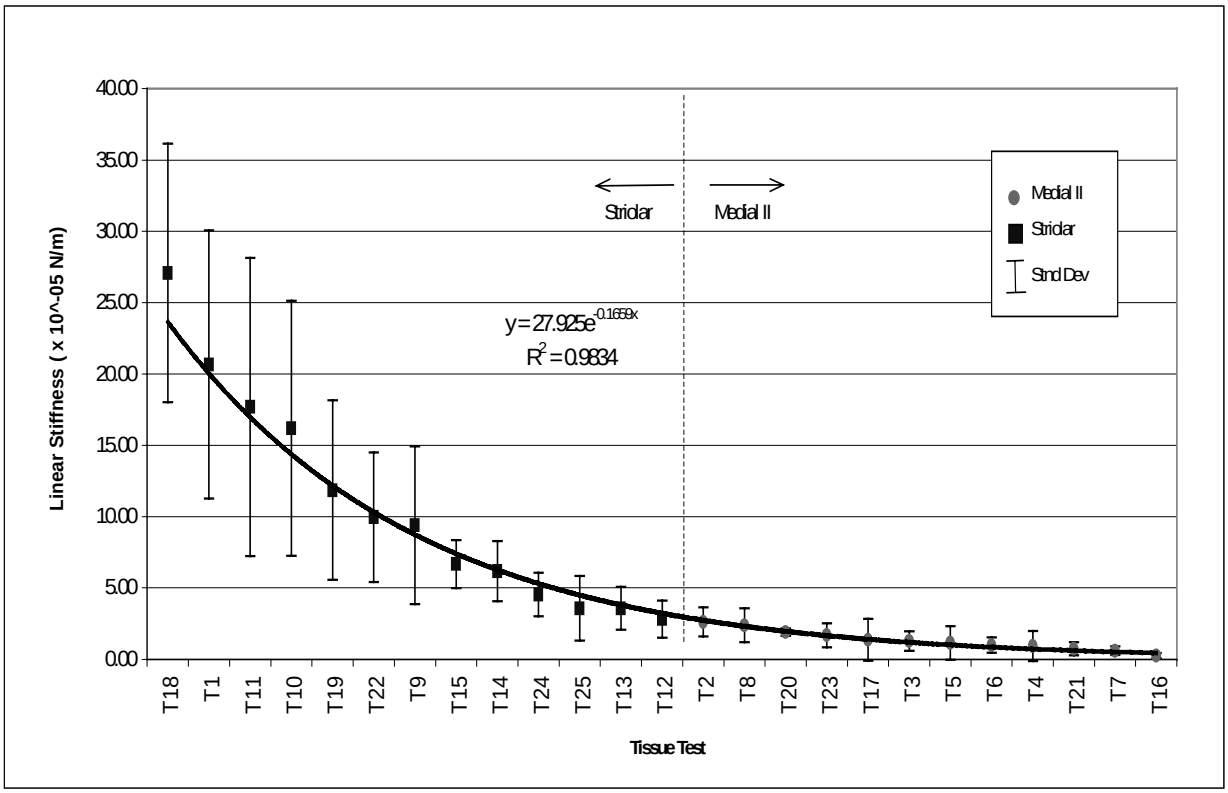

Figure 7.12 Linear stiffness results with standard deviations.
This plot shows the linear stiffness results for all bundles in descending order. Notice that the stiffness values for the striolar and medial II bundles do not overlap. This data trend provides evidence that the stiffness values for bundles occur over a wide range for each type of cell.

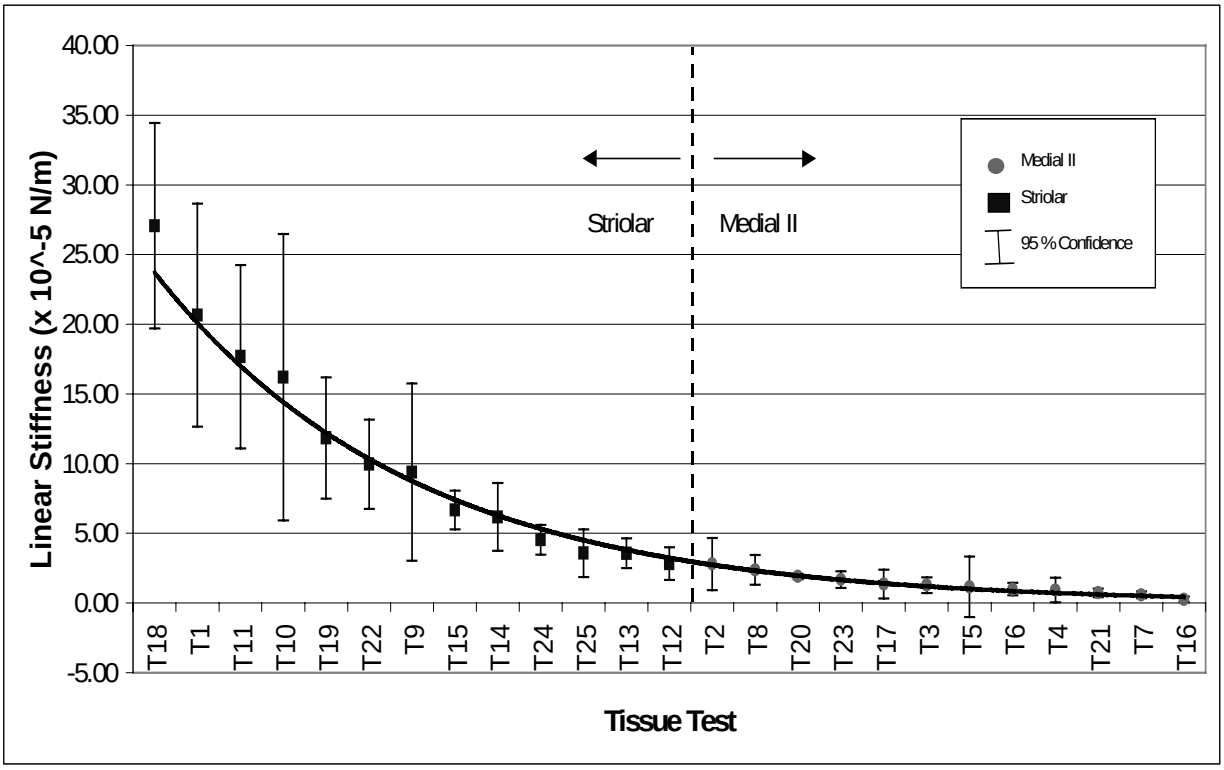

Figure 7.13 Linear stiffness results with 95% confidence limits.
This plot shows the linear stiffness results for all bundles in descending order. The 95% confidence limits are included as opposed to one standard deviation as seen in Figure 7.12.

Specimen	Test	Cell Type	Turtle Weight	Linear Stiffness (x10^-5 N/m)	Standard Deviation (x10^-5 N/m)
1	T1	s	-	20.67	13.995
	T2	m	-	2.62	1.025
2	T3	m	-	1.28	0.688
	T4	m	-	0.94	1.062
	T5	m	-	1.16	1.181
3	T6	m	-	1.00	0.535
	T7	m	-	0.60	0.309
	T8	m	-	2.38	1.185
4	T9	s	220	9.40	5.530
	T10	s	220	16.20	8.943
	T11	s	220	16.20	10.452
5	T12	s	185	2.83	1.305
	T13	s	185	3.57	1.505
	T14	s	185	6.18	2.110
	T15	s	185	6.68	1.689
6	T16	m	160	0.26	0.183
	T17	m	160	1.37	1.470
	T18	s	160	27.10	9.073
	T19	s	160	12.60	6.420
7	T20	m	220	1.92	0.263
	T21	m	220	0.74	0.453
8	T22	s	210	9.97	4.537
	T23	m	210	1.69	0.847
	T24	s	210	4.54	1.520
	T25	s	210	4.15	2.262

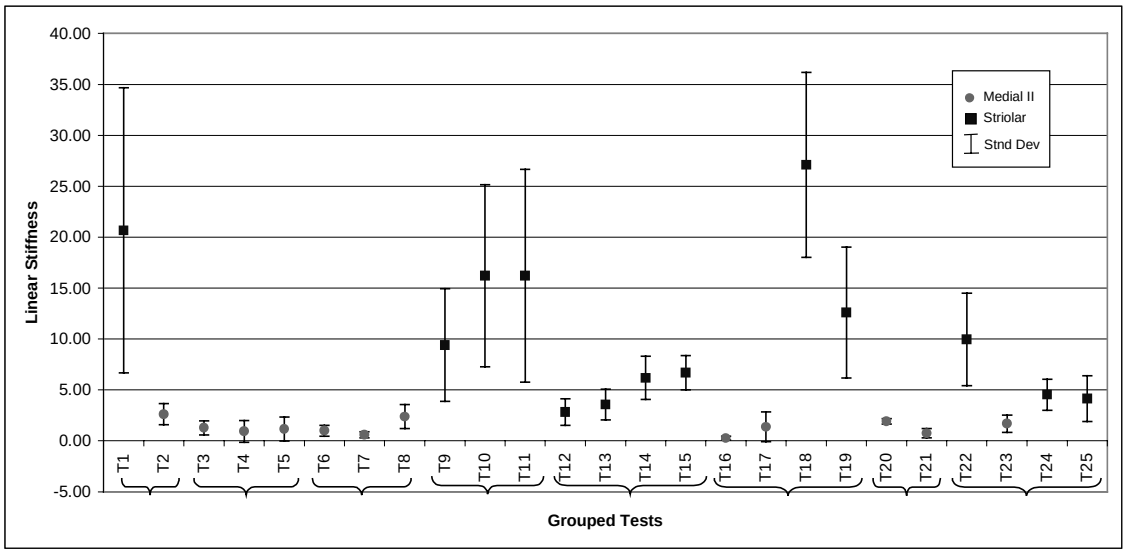

Figure 7.14 Test results grouped by specimen.
This plot shows how the linear stiffness of the hair bundles differed from specimen to specimen.

7.4.4 Torsional Stiffness Results

After examining the linear stiffness results, we wanted to see if the stiffness values we had obtained were based on the height at which the force was applied to the kinocilium. If we could eliminate this factor and the variation in the stiffness values were siginificantly reduced, then we would know that the point of force application greatly influenced the resulting stiffness. If the variation in data was not reduced, this would point to the conclusion that the location of the applied force did not have a great impact.

If the bundle behaves as if it were a rigid rod attached to a spring near its base, then the torque around the base may be expressed in terms of torsional stiffness (k_T) [Crawford and Fettiplace, 1985]; often referred to as a rotational stiffness. This stiffness value can be determined from

$$k_T = \frac{F_B \times h}{\theta} \qquad \text{[N-m/rad]} \qquad [7.1]$$

where F_B is the force applied to the bundle, h is the height at which the force is applied (kinocilium height), and θ is the angular deflection of the bundle. The force applied to the bundle is found using the stiffness and displacement of the whisker

$$F_B = k_W \times \Delta x_W \quad \text{[N]} \qquad [7.2]$$

which are quantities that were previously measured. The height of the kinocilium was measured using the Imagen XR 2001. The angular deflection of the bundle was calculated by using the height at which the force was applied and the corresponding bundle displacement.

$$\theta = \text{ArcTan}\left(\frac{h}{\Delta x_B}\right) \quad \text{[radians]} \qquad [7.3]$$

Using these equations, the torsional stiffness for each of the bundles was calculated. They were then arranged in descending order of stiffness and plotted in Figure 7.15. There is slightly less variation within this data set, which is obvious by comparing the range of these values with those for linear stiffness. However, it does not limit the variability significantly enough to conclude that the height of force application is a determining factor for stiffness values. In fact, there is still a very nice exponential curve to the data. This trend actually supports the theory that there is a wide spectrum of

stiffness values within the utricle. Another interesting observation is that the medial II and striolar values are inter-dispersed. They are desegregated as opposed to the trend seen for the linear stiffness data points. A final note is that we used the tip of the kinocilium as the point at which the force was applied. this was not always the case, but since we had not recorded this point initially, it was a reasonable approximation.

In Figure 7.16, the linear and torsional stiffness values were plotted together in descending order of linear stiffness. This plot shows that the stiffness and torsional results do not show the same relative cell to cell stiffness relationships. However, there is noticeable variability for both sets of data.

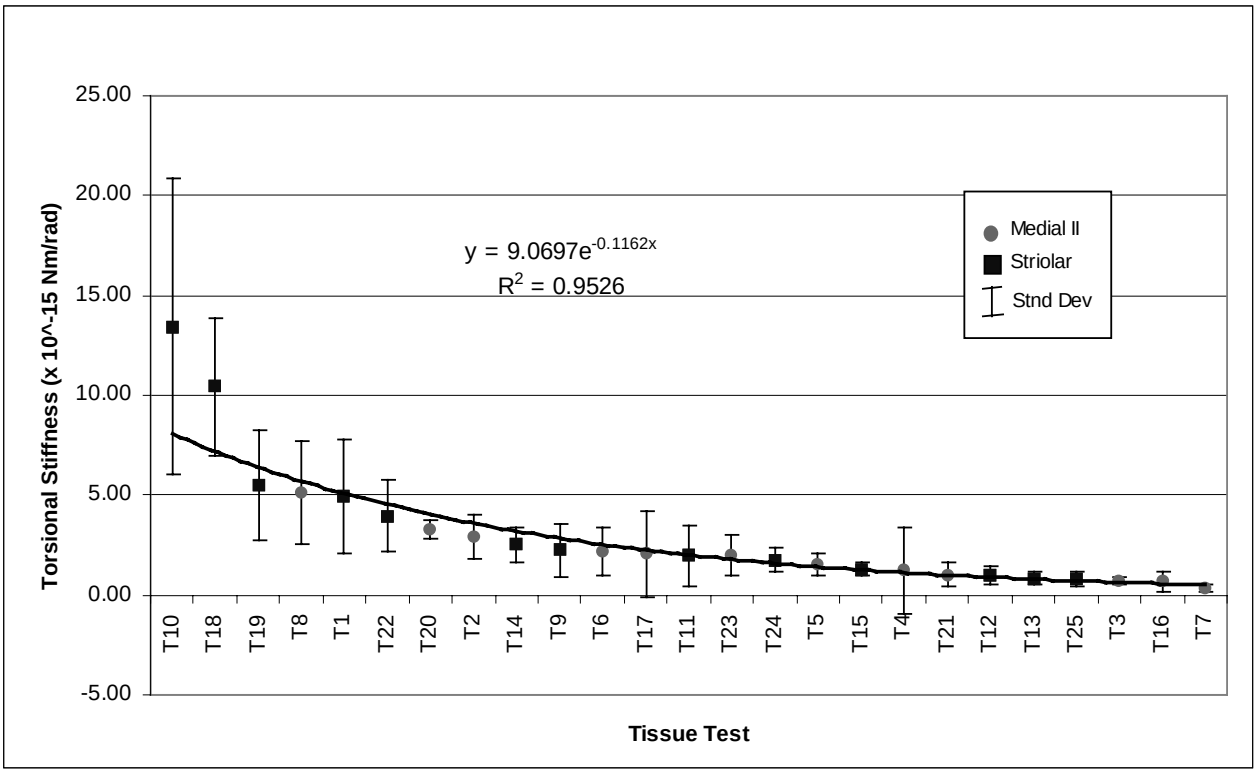

Figure 7.15 Torsional stiffness for medial II and striolar bundles.
The results for torsional stiffness data exhibit the same general trend as the results for linear stiffness. However, the order of cell descension is not the same. Medial II cells and striolar cells have inter-dispersed torsional stiffness values. Although this data set has decreased variability, it is not significant enough to draw any conclusions.

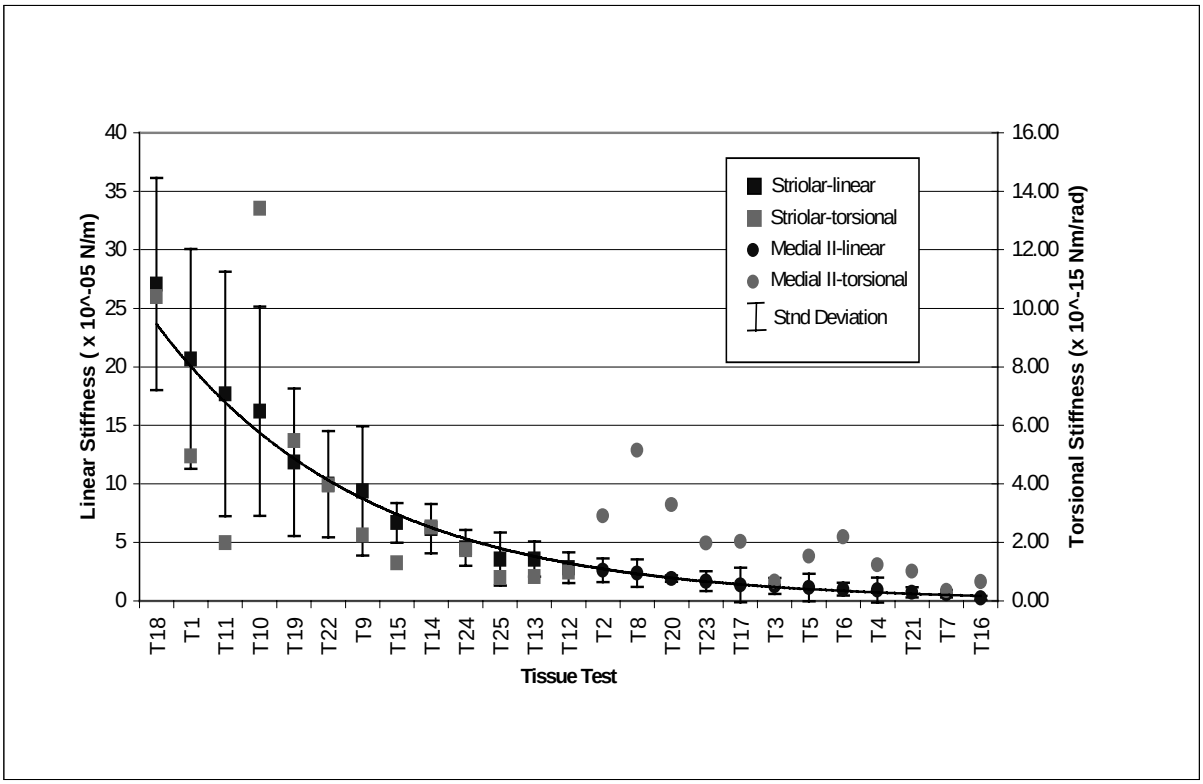

Figure 7.16 Linear and torsional stiffness values.
This plot displays both sets of stiffness data in descending order of linear stiffness. Although the data sets individually show the same decreasing exponential pattern in the previous two figures, the cell order in which this trend occurs is not the same, as shown here.

7.5 EXPERIMENTAL RESULTS VERSUS FEM RESULTS

The development of the FEM vestibular bundle model required assumptions concerning bundle tip links, lateral links, and the kinocilium [Cotton, 1998]. Our current measurement values for medial II bundle stiffness is approximately 1×10^{-5} N/m and the FEM effort predicts this stiffness to be 1×10^{-4} N/m. We measured a mean stiffness for the striolar bundles to be 10×10^{-5} N/m, whereas the model again predicts a stiffer value of 10×10^{-4} N/m. This is approximately an order of magnitude difference between our values and those of the model for both sets of cells. The discrepancy is most like due to the stiffness value that was adopted in the modeling effort for the kinocilium of the bundle. The value was used was taken from a measurement of a flagellum tail. This tale has the same 9+2 microtubal structure as a kinocilium. Our assumption was that the two structures have similar stiffness values. This is apparently not true. The thinking here is that the overall medial II cell stiffness reflects mostly the stiffness of the kinocilium because of the short stereocilia and tall kinocilium. What we need to do is strip away the remainder of the stereocilia in one of these bundles and measure the stiffness of only the kinocilium. This will be a future research effort. The second source of modeling error may be the modulus of the lateral links that bind the bundle together. Once a good experimental value of the kinocilium is computed, we may find that the estimated value of modulus for these links may be to large as well.

Although the results of the model differ from the experimental results, it is very interesting to see that the relative relationship of stiffness between the two bundle types remains the same in both cases. An order of magnitude separates mean medial II and striolar stiffness values in the results from both the modeling and experimental efforts.

8.0 SUMMARY AND CONCLUSIONS

This thesis presents the research involved in developing a method for measuring the stiffness of ciliary bundles and using this method to conduct actual tissue tests. The techniques used to measure bundle stiffness have been introduced and explained in detail. Performance tests conducted on the system were presented to demonstrate the effectiveness of the technique. The results from the tissue tests were also presented in this work in order to learn of their mechanical properties and compare them with results from a computer model. The overall intent is to aid in the understanding of the role hair cells play in the mechanoelectrical transduction process that occurs in the vestibular system.

The subject used in this work was the red-eared sliding turtle. A reliable method was developed for dissecting out the vestibular system and for further cutting the tissue to isolate the utricle. The utricle was positioned under a microscope with DIC optics and an immersion lens so that its hair cells would be visible. A need for a mechanical method for stimulating the bundles was solved with the use of glass whiskers. The whisker of known stiffness was bonded to a pipette which was attached to a micromanipulator. The micromanipulator positioned the whisker against the bundle and then continued to move in order to create a force on the bundle. The amount the bundle was displaced along with the amount the pipette was moved and the whisker stiffness allowed for the calculation of the bundle stiffness. Therefore, measurement techniques were needed to calculate these displacements.

An Extrinsic Fabry-Perot Interferometer (EFPI) was used to measure the amount the pipette was moved by the micromanipulator. A Photoelectronic Motion Transducer (PMT) detected the amount the bundle was displaced by the whisker's force. The PMT used photodiodes and a differential amplifier to detect shifts in light intensity caused by the movement of the bundle-whisker tip. The system produced a voltage change corresponding to the movement. Calibrations of the PMT were used to convert the

change in output voltage into a displacement. All of the unknowns which were required to calculate the bundle stiffness, were now able to be found.

Performance tests were conducted on the displacement detection system. A whisker, with stiffness already found by using styrene beads, was used in place of the ciliary bundle. This imitation bundle was displaced by another whisker of known stiffness. Three tests were performed on the system and the imitation bundle stiffness results were compared with the stiffness values attained from using styrene beads. The results differed by 4.43, 4.14, and 1.38%. The magnitudes of these errors were within experimental limitations and therefore the testing method was deemed valid and useful.

A total of 25 tissue tests were conducted on two types of hair cells. Twelve tests were performed on medial II cells while 13 tests were done on striolar hair cells. The medial II cells varied in stiffness, ranging from 0.26 to 2.62 E-05 N/m. The striolar results had hair bundles with stiffness values ranging from 2.83 to 27.10 E-05 N/m. When the tests done on both cell types were statistically analyzed with a student's t-distribution, a p-value of 2.19×10^{-18} was found. This signifies that we are examining two distinct populations and that the results we obtained are repeatable.

When the values from both cell types were plotted in descending order, the result was a trend well approximated by an exponential fit. This plot provided evidence that the stiffness for these cells occur over a wide spectrum, not just a narrow range. This supports the theory that bundle stiffness depends on morphology. It also leads to the theory that the utricle would require bundles with varying stiffness values in order for it to be capable of sensing a wide range of accelerations. If the head undergoes a small linear acceleration, then the less stiff medial II bundles will deflect and transduce this movement into a neural signal. At larger accelerations, these cells will reach a point of saturation. However, the more stiff striolar bundles, which require a larger force to be deflected, will not be saturated and can snese these larger accelerations. therefore, a wide range of accelerations can be interpreted by bundle deflection in the utricle.

The data were further analyzed by computing the torsional, or rotational, stiffness. This value would essentially eliminate any variability that occurred due to the point at which the force was applied. The results did slightly reduce the variability in stiffness

data, but not enough to conclude that the point of force application was the cause for the wide range of data.

Overall, the stiffness values for the striolar hair bundles were approximately an order of magnitude larger than the medial II bundles. This relationship is consistent with the results from an FEM computer model developed for the hair cells. However, the experimental results for both types of cells were an order of magnitude less than the values found from the model. As a result, the computer model will be reviewed and the assumptions revised in an effort to achieve results comparable to experimental values.

In conclusion, although the test system was proven to operate well, the data presented here must be viewed as preliminary results. However, it does present evidence that stiffness values occur over a wide range, they may vary over the life cycle of the animal, and there is a definite difference in stiffness magnitude between striolar and medial II ciliary bundles. Further tests will need to be conducted in an effort to expand on these results.

9.0 FUTURE WORK AND RECOMMENDATIONS

There still remains much work that can be done with measuring the stiffness of ciliary bundles. Although this work presented a system for which to measure the stiffness and the results of 25 tests, there are still many aspects to explore. The equipment used to conduct tests can also be further improved for additional accuracy in results. Also, as researchers become confident in the stiffness values, then the scope of knowledge regarding vestibular mechanics will expand and lead to other investigations.

The test results presented in this work provide the results for the stiffness of 25 striolar and medial II hair cell bundles. Additional tests should be conducted to expand upon these results as well as tests performed on lateral bundles located in the rampa. Further investigation will aid in understanding the mechanics of the hair bundles and may lead to a conclusion concerning the relationship of stiffness and displacement presented by Russell, et al.

The equipment used to conduct the tests worked extremely well. However, there was the existence of a low frequency noise in the PMT. If the source of this noise were located and eliminated, then the displacement detection system would achieve even greater accuracy and may eliminate some of the scatter within the test data. The method for conducting tests can also be improved. A program that would enable the data from the EFPI and the PMT to be recorded with a computer by using a trigger mechanism (mouse click) would be an immense help. Currently, we are limited to conducting tests on three or four hair cells per turtle due to the time it takes to conduct a single test and the short timeframe in which the tissue is viable. An automated system would decrease test time and dramatically increase the quantity of results.

The finite element model of the hair cells conducted by Cotton, et al. should be re-examined and some of the assumptions modified. This should lead to either better agreement with and support of the experimental results presented here, or it will disagree and spurn more testing. Either way, if the experimental work is performed correctly and the assumptions for the FEM are accurate, the results should eventually agree.

REFERENCES

Azzi, A.A. (1981). "Considerations on Labyrinthine Hydrodynamics in Meniere's Disease."

Barrett, M.D. (1995). Fiber Optic Interferometer for Measuring Sub-Micrometer Displacements of Ciliary Bundles. Thesis, Virginia Polytechnic Institute and State University.

Barrett, M.D., Peterson, E.H., & Grant, J.W. (1999). "Extrinsic Fabry-Perot Interferometer for Measuring the Stiffness of Ciliary Bundles on Hair Cells." *IEEE Transactions on Biomedical Engineering* 46:331-339.

Beer, F.P. & Johnston, Jr., E.R. (1992). Mechanics of Materials, Second Edition. New York: McGraw Hill.

Burleigh Manuals. (1997). Fishers, New York.

Cha, J.H. (1994). Application of the Photodiode in Design of a 2-D Position Detector. Thesis, Virginia Polytechnic Institute and State University.

Cotton, J.R. (1998). Mechanical Modeling of Vestibular Hair Cell Bundles. Dissertation, Virginia Polytechnic Institute and State University.

Crawford, A.C. & Fettiplace, R. (1985). "The mechanical properties of ciliary bundles of turtle cochlear hair cells." *Journal of Physiology* 364: 359-379.

Denk, W., Webb, W.W., & Hudspeth, A.J. (1989). "Mechanical properties of sensory hair bundles are reflected in their Brownian motion measured with a laser differential interferometer." *Proc. Natl. Acad. Sci.* 86: 5371-5375.

EG&G Product Bulletin 1090. Montgomeryville: PA.

Encarta Learning Zone (Brownian Motion)
Available: http://encarta.msn.com

Engström, H. & Engström, B. (1981). "The Structure of the Vestibular Sensory Epithelia." The Vestibular System: Function and Morphology. Edited by T. Gualitierotti. New York: Springer-Verlag.

F&S, Inc. AFSS-PC v3 User's Manual,Revision B. (1999). Blacksburg, VA.

Flock, Å. (1983). "Micromechanical properties of sensory hairs on receptor cells of the inner ear." *Hearing Research* 11: 249-260.

Geisler, D.C. (1998). From Sound to Synapse: Physiology of The Mammalian Ear. New York: Oxford University Press.

Gelfand, S.A. (1998). Hearing. New York: Marcel Dekker, Inc.

Gelles, J., Schnapp, B.J., & Sheetz, M.P. (1998). "Tracking kinesin-driven movements with nanometre-scale precision." *Nature* 331: 450-453.

Howard, J. & Ashmore, J.F. (1986). "Stiffness of sensory hair bundles in the sacculus of the frog." *Hearing Research* 23: 93-104.

Howard, J. & Hudspeth, J. (1988). "Compliance of the hair bundle associated with gating of the mechanoelectricla transduction channels in the bullfrog's saccular hair cell." *Neuron* 1: 189-199.

Huang, A.Y. (1991). A Photoelectronic Motion Transducer for Measuring Sensory Hair Bundle Movements on Isolated Inner Ear Hair Cells. Student Research Project, University of Pennsylvania.

Hudspeth, A.J. (1983). "The hair cells of the inner ear." *Scientific American* 248: 54-64.

Inoué, S. & Spring, K.R. (1997). Video Microscopy: The Fundamentals, Second Edition. New York: Plenum Press.

Kazahaya, K. (1989). Photoelectronic Motion Transducer: The Design, Construction and Operation of a Photodiode Detector for Microscopic Studies of Hair Bundle Motion. Student Project, University of Pennsylvania.

Kelly, J.P. (1991). "The Sense of Balance." Principles of Neural Science, Third Edition. Edited by E.R. Kandel and J.H. Schwartz. Norwalk, CT: Appleton and Lange.

Kelly, J.P. (1981). "Vestibular System." Principles of Neural Science. Edited by E.R. Kandel and J.H. Schwartz. New York: Elsevier North Holland, Inc.

Klinke, R. (1986). "Physiology of Hearing." Fundamentals of Sensory Physiology. Edited by R.F. Schmidt. New York: Springer-Verlag.

Lewis, E.R., Leverenz, E.L., & Bialek, W.S. (1985). The Vertebrate Inner Ear. Boca Raton, FL: CRC Press, Inc.

Perkins, W.H., Kent, R.D. (1986). Fuctional Anatomy of Speech, Language, and Hearing. San Diego, CA: College-Hill Press

Russell, I.J., Kössl, M., Richardson, G.P. (1992). "Nonlinear mechanical responses of mouse cochlear hair bundles." *Proc. R. Soc. Lond.*250: 217-227.

Saunders, J.C. & Szymko, Y.M. (1989). “The design, calibration, and use of a water microjet for stimulating hair cell sensory bundles.” *Journal of Acoustical Society of America* 86: 1797-1804.

Shepherd, G.M. (1988). Neurobiology, Second Edition. New York: Oxford University Press.

Schnapp, B.J., Gelles, J., & Sheetz, M.P. (1988). “Nanometer-scale measurements using video light microscopy.” *Cell Motility and the Cytoskeleton* 10:47-53.

Singh, R.P. (1980). Anatomy of Hearing and Speech. New York: Oxford University Press.

Sokal, R.R. & Rohlf, F.J. (1981). Biometry. New York: W. H. Freeman and Company.

Streiloff, D. & Flock, Å. (1984) “Stiffness of sensory-cell hair bundles in the isolated guinea pig cochlea.” *Hearing research* 15: 19-28.

Szymko, Y.M., Dimitri, P.S., & Saunders, J.C. (1991). “Stiffness of hair bundles in chick cochlea.” *Hearing Research* 59: 241-249.

VITA

Andrew Charles Merkle was born in Washington, D.C. on May 11, 1976. He spent his childhood in Clinton, Maryland until moving to Upper Marlboro, Maryland when he was 17. He attended Bishop McNamara high school and graduated as valedictorian in 1994. He went on to Virginia Polytechnic Institute and State University to play soccer and study engineering. In the Spring of 1998, he graduated with his Bachelors of Science; majoring in Engineering Science and Mechanics and concentrating in Biomechanics. In addition to his academic studies, Mr. Merkle played on the Virginia Tech Varsity Soccer Team and was a member and President of the university chapter of The Biomedical Engineering Society. Upon graduation with his Masters of Science in Engineering Mechanics, he will continue his career in biomedical engineering with a position at The Johns Hopkins University Applied Physics Labs in Columbia, Maryland.